Spring 5-19-2017

Motion Dynamics of Dropped Cylindrical Objects

Gong Xiang
University of New Orleans, xghust89@gmail.com

Motion Dynamics of Dropped Cylindrical Objects

A Dissertation

Submitted to the Graduate Faculty of the
University of New Orleans
in partial fulfillment of the
requirements for the degree of

Doctor of Philosophy
in Engineering and Applied Science
Naval Architecture and Marine Engineering

by

Gong Xiang

B.S. Huazhong University of Science and Technology 2011
M.E. Stevens Institute of Technology 2013
May 2017

Dedicated to the people who love mathematics, science, and engineering.

Acknowledgement

I would like to express the deepest appreciation to my committee chair Professor Lothar Birk and co-chair Professor Xiaochuan Yu. They continually and convincingly conveyed a spirit of adventure in regard to research and an excitement in regard to teaching. Without their guidance and persistent help this dissertation would not have been possible.

I would like to thank my committee member, Professor Brandon Taravella who recruited me into UNO's PhD program and gave me clear guidance on finishing all the official requirements for the degree.

In addition, thank Professor Linxiong Li and Professor Uttam K Chakravarty for serving on my committee.

At last, I would like to thank my dear parents for their continuous understanding and support.

Contents

List of Figures

List of Tables

Symbols

β :	the instantaneous rotational angle between x-axis and X-axis.	rad
m:	the mass of the cylinder	kg
ρ_c:	the mass density of the cylinder	kg/m
m_t:	2D added mass coefficient in heave direction at the trailing edge	kg/m
x_t:	longitudinal position of effective trailing edge	m
g:	acceleration of gravity	m/s^2
ρ:	the density of water	kg/m^3
δ:	the volume of the cylinder	m^3
D:	diameter of the cylinder	m
ν :	kinematic viscosity of water	m^2/s
L:	length of the cylinder	m
C_{dx}:	drag coefficient in x-direction	
C_{dz}:	drag coefficient in z-direction	
ϕ:	the instantaneous Euler angle around X-axis	rad
θ:	the instantaneous Euler angle around Y-axis	rad
ψ:	the instantaneous Euler angle around Z-axis	rad
I_{44}:	mass moment of inertia of the cylinder in roll direction	kg m^2
I_{55}:	mass moment of inertia of the cylinder in pitch direction	kg m^2
I_{66}:	mass moment of inertia of the cylinder in yaw direction	kg m^2
m_{22}:	added mass in sway direction from strip theory	kg
m_{33}:	added mass in heave direction from strip theory	kg
m_{55}:	added mass in pitch direction from strip theory	kg m^2
m_{66}:	added mass in yaw direction from strip theory	kg m^2
m_{35}:	cross-coupling added mass between heave and pitch direction	kg m
m_{26}:	cross-coupling added mass between sway and yaw direction	kg m
m_{t2}:	2D added mass coefficient in sway direction at the trailing edge	kg/m
m_{t3}:	2D added mass coefficient in heave direction at the trailing edge	kg/m
M_{22}:	2D added mass coefficient in sway direction	kg/m
M_{33}:	2D added mass coefficient in heave direction	kg/m

U_1:	translational velocity in x direction	m/s
U_2:	translational velocity in y direction	m/s
U_3:	translational velocity in z direction	m/s
Ω_1:	rotational velocity in x direction (rolling frequency)	rad/s
Ω_2:	rotational velocity in y direction (pitching frequency)	rad/s
Ω_3:	rotational velocity in z direction (yawing frequency)	rad/s
A:	constant value determined by the position of transition	
c:	rolling frequency decaying rate	rad/s^2
W:	the lateral velocity of the body section	m/s
$\vec{i}$:	unit vector in x direction	
$\vec{j}$:	unit vector in y direction	
$\vec{k}$:	unit vector in z direction	
$\vec{i}_O$:	unit vector in X direction	
$\vec{j}_O$:	unit vector in Y direction	
$\vec{k}_O$:	unit vector in Z direction	

Abbreviations

DORIS	**D**ropped **O**bjects **R**egister of **I**ncidents & **S**tatistics
HSE	**H**ealth **S**afety and the **E**nvironment
DOS	**D**ropped **O**bjects **S**imulator
ABS	**A**merican **B**ureau of **S**hipping
DNV	**D**et **N**orske **V**eritas
DOF	**D**egree **O**f **F**reedom
NPS	**N**aval **P**ostgraduate **S**chool
LCG	**L**ongitudinal **C**enter **G**ravity
SD	**S**tandard **D**eviation
PDF	**P**robability **D**ensity **F**unction
CDF	**C**umulative **D**istribution **F**unction

Abstract

Dropped objects are among the top ten causes of fatalities and serious injuries in the oil and gas industry. Objects may be dropped during lifting or any other offshore operation. Concerns of health, safety, and the environment (HSE) as well as possible damages to structures require the prediction of where and how a dropped object moves underwater. This study of dropped objects is subdivided into three parts.

In the first part, the experimental and simulated results published by Aanesland (1987) have been successfully reproduced and validated based on a two-dimensional (2D) theory for a dropped drilling pipe model. A new three-dimensional (3D) theory is proposed to consider the effect of axial rotation on dropped cylindrical objects. The 3D method is based on a modified slender body theory for maneuvering. A numerical tool called Dropped Objects Simulator (DROBS) has been developed based on this 3D theory. Firstly, simulated results of a dropped drilling pipe model using a 2D theory by Aanesland (1987) are compared with results from 3D theory when rolling frequency is zero. Good agreement is found. Further, factors that affect the trajectory, such as drop angle, normal drag coefficient, binormal drag coefficient, and rolling frequency are systematically investigated. It is found that drop angle, normal drag coefficient, and rolling frequency are the three most critical factors determining the trajectories.

In the second part, a more general three-dimensional (3D) theory is proposed to physically simulate the dynamic motion of a dropped cylindrical object underwater with different longitudinal center of gravity (LCG). DROBS has been further developed based on this 3D theory. It is initially applied to a dropped cylinder with LCG = 0 (cylinder #1) falling from the surface of calm water. The calculated trajectories match very well with both the experimental and numerical results published in Aanesland (1987). Then DROBS is further utilized to simulate two dropped cylinders with positive LCG (cylinder #2) and negative LCG (cylinder #3) in Chu et al. (2005), respectively. The simulated results from DROBS show a better agreement with the measured data than the numerical results given in Chu et al. (2005). This comparison again validates and indicates the effectiveness of the DROBS program. Finally, it's applied to investigate

the effects of varying LCG on the trajectory and landing points. Therefore, the newly developed DROBS program could be used to simulate the distribution of landing points of dropped cylindrical objects, as is very valuable in the risk-free zone prediction in offshore engineering.

The third part investigates the dynamic motion of a dropped cylindrical object under current. A numerical procedure is developed and integrated into Dropped Objects Simulator (DROBS). DROBS is utilized to simulate the trajectories of a cylinder when dropped into currents from different directions (incoming angle at $0^o, 90^o, 180^o,$ and 270^o) and with different amplitudes (0m/s to 1.0m/s). It is found that trajectories and landing points of dropped cylinders are greatly influenced by currents. Cylinders falling into water are modeled as a stochastic process. Therefore, the related parameters, including the orientation angle, translational velocity and rotational velocity of the cylindrical object after fully entering the water, is assumed to follow normal distributions. DROBS is further used to derive the landing point distribution of a cylinder. The results are compared to Awotahegn (2015) based on Monte Carlo simulations. Then the Monte Carlo simulations are used for predicting the landing point distribution of dropped cylinders with drop angles from 0^o to 90^o under the influence of currents. The plots of overall landing point distribution and impact energy distribution on the sea bed provide a simple way to indicate the risk-free zones for offshore operation.

Key words: Dropped cylindrical object; 3D motion; Excursion distribution; Monte Carlo simulation; risk free zone.

Chapter 1

Introduction

Study on the movement of a dropped rigid body in water has wide scientific significance and technical application in the offshore industry. It involves knowledge about nonlinear dynamics, maneuvering theory, fluid dynamics, probability, and statistical methods.

Dropped objects are one of the principal causes of accidents in the oil and gas industry and increase the total risk level for offshore and onshore facilities (*DORIS* 2016). Objects may accidentally fall down from platforms or vessels during lifting or any other offshore operation. Small dropped objects such as scaffolding bars may cause little damage to sub-sea structures and equipment like pipelines. However, when crane activities happen during offshore platform installations, dropping larger objects such as drill pipes, containers, or B.O.P. stacks into the water cause potentially greater hazards, due to the likelihood of significant damage resulting from their larger impact energy (Brown and Perry, 1989).

The frequency for dropped tools and equipment into the sea is significant. As recorded by the UK Department of Energy, during the period 1980—1986 (DNV, 1996), 81 incidents with dropped objects within 825 crane years are reported. There are 3.7 million lifts estimated to happen in the period, which corresponds to 4.500 lifts to/from vessel per crane per year. This also gives a dropped object frequency of 2.2×10^{-5} per lift. The drop frequency for lifts above 20tons is even higher and has been estimated to even reach 3.0×10^{-5} per lift. The frequency of drops is further divided into a 70 $\%$ chance to fall onto deck and a 30 $\%$ chance to fall into the sea.

The proposed dropped object frequency relates to individual crane types and specific operation types as shown in Table 1.1. The frequency of losing a BOP during lowering to or lifting from a well is higher than for other typical crane lifts (DNV, 2010).

Table 1.1: Frequencies for dropped objects into the sea (DNV, 2010)

Type of lift	Frequency of dropped object into the sea (per lift)
Ordinary lift to/from supply vessel with platform crane < 20 tonnes	1.2×10^{-5}
Heavy lift to/from supply vessel with the platform crane > 20 tonnes	1.6×10^{-5}
Handling of load < 100 tonnes with the lifting system in the drilling derrick	2.2×10^{-5}
Handling of BOP/load > 100 tonnes with the lifting system in the drilling derrick	1.5×10^{-5}

ABS guidance (ABS, 2010) proposes a general evaluation process for the assessment of damages due to dropped objects which may result from failed lifting operations from a supply boat or unsecured debris falling overboard during storms. However, this guidance does not address deep water structures (either fixed jackets or floating hull systems) and subsea equipment. DNV (2010) proposes specific rules about the risk assessment for pipeline protection. In its recorded simplified method, object excursions on the seabed are assumed to be normally distributed. However, there are still no specialized techniques to predict the trajectory of dropped objects and the subsequent likelihood of striking additional structure and equipment as well as predicting the consequences of such impacts (ABS, 2010). Therefore, motion dynamics of objects falling into the water and their landing points are of interest for the protection of oil and gas production equipment resting on the seabed.

This dissertation elucidates the theory involved in specifying the 2D and 3D motion of dropped cylindrical objects, the development and extension of 3D theory to consider mass center and environmental conditions such as a current, the statistical study of risk free zones, and the conclusions found from the comparison of theoretical and experimental results. This chapter explains the motivation for this research. The chapter concludes with how this project contributes to solving the practical problem about dropped objects in the offshore industry. Chapter 2 provides a brief overview of previous research on similar work involving experimental and numerical studies of dropped cylindrical objects. Chapter 3 illustrates the 2D theory of dropped cylindrical objects by introducing equations of motion and explaining force and moments acting on the body. The numerical simulations based on 2D theory are verified by comparing

simulated results with experimental results. Chapter 4 details the new three-dimensional (3D) theory which considers 6 DOF motions by modifying the maneuvering equations for a slender rigid body. Chapter 5 introduces a statistical study on landing points of dropped cylindrical objects falling through air-water columns by using Monte Carlo simulations. Chapter 6 states the conclusions determined from all the facts gathered throughout the entire research process. These conclusions tie in all aspects of the theory and numerical simulation, provide a comparison to the overall field of associated research.

Chapter 2

Literature Review

In the offshore industry, the problem with dropped objects accidentally falling from platforms or vessels into water is well known and was already reported in 20th century. Correspondingly, lots of early research studies on solving this problem were started and accomplished. Aanesland (1987) experimentally and numerically investigated falling drilling pipes. Two model tests were presented. The first test was performed in order to investigate the entire history of events from a drop at the platform deck till the object lands on the seabed. The second drop test was intended to verify a computer program which was developed to calculate the motion, velocity, and acceleration of falling drilling pipes and to predict the impact load. A number of different trajectories were observed in the tests and are as illustrated in Fig. 2.1.

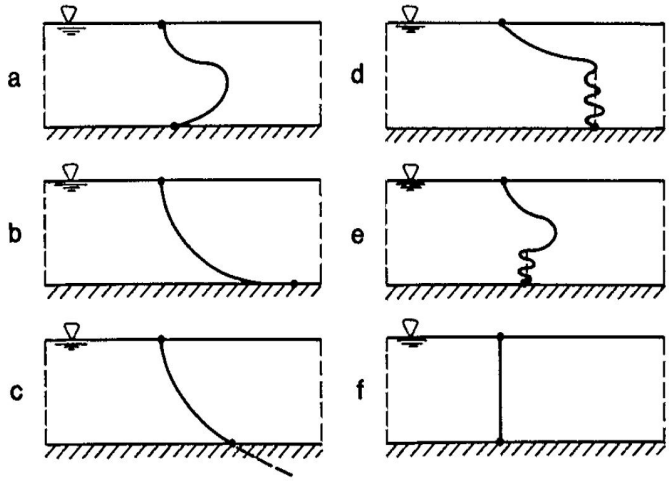

Fig. 2.1. Sketches of observed trajectories (Aanesland, 1987)

Aanesland's program solves a set of two-dimensional (2D) maneuvering equations which describe the motions of drilling pipes, in which the trailing edge effect for a long slender body has been considered and further corrected for viscous effects (Newman, 1977). The drag coefficient is assumed to be constant at each time step.

Luo and Davis (1992) also simulated the 2D motion of falling objects by solving the differential equations of motion. Illustrative parametric studies are carried out in a computer program called DELTA. It was found that the horizontal motion and velocity of the dropped object are greatly affected by drop angle and drop height. Also, horizontal excursion at the seabed level is found to be significantly influenced by drop angle and current. However, waves have limited overall effect on both horizontal excursion and the maximum velocity. Meanwhile, Colwill and Ahilan (1992) performed multiple numerical studies of trajectories of two dropped drill casings by using the same computer program, DELTA. These studies confirmed that drop height above waterline and the initial drop angle were key parameters influencing the final horizontal velocity. Reliability-based impact analysis successfully established the relation between impact velocity and the probability of its exceedance.

Kim et al. (2002) focused on the study of characteristic motions of 3D bodies freely falling through water. The time-domain six degree-of-freedom motions of general 3D bodies as shown

in Fig. 2.2 dropping in water has been solved by a direct numerical scheme, the 4-th order Runge-Kutta scheme. In addition, viscous effects on the cylindrical bodies have been considered by estimating the drag coefficients of the bodies for various body aspect ratios, end shapes, and orientations to incoming flow based on laboratory experiments. A comparison between numerical results and experimental tests showed that the simulated motion pattern depend significantly on initial drop angle, body aspect ratio, and mass center.

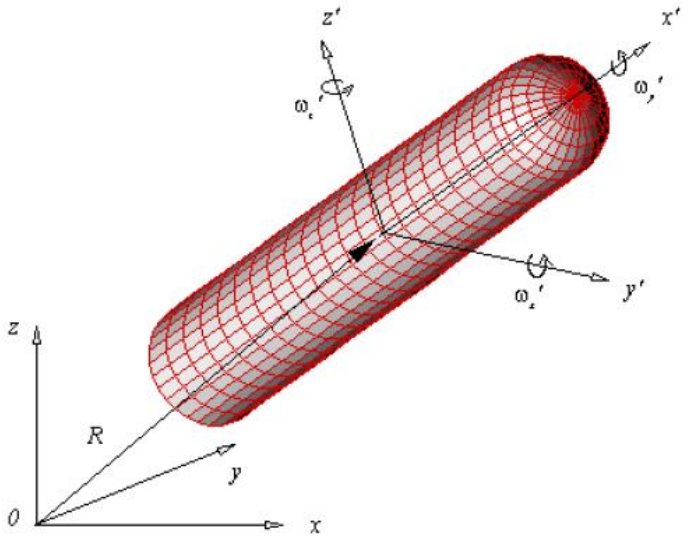

Fig. 2.2. Coordinate system for equation of motions in three dimensions (Kim et al. 2002)

Mann et al. (2007) developed a physics-based computational model to predict the motion of a 3-D mine-shaped object impacting the water surface from the air, and subsequently, dropping through the water toward the sea bottom. This deterministic model [mine's six-degree-of-freedom dynamics (MINE6D)] accounts for six-degree-of-freedom motions of the body including unsteady hydrodynamic interaction effects, water impact and air cavity effects. To demonstrate the efficacy of the model, the authors compared deterministic MINE6D predictions with tank drops tests and field measurements. In practical applications, the environments are often quite irregular, and the releasing conditions are also uncertain. To provide some guidance in understanding and interpreting statistical characterizations of mine motions in practical environments, the authors performed Monte Carlo simulations using MINE6D.

Chu et al. (2002) conducted the Mine Impact Burial Prediction Experiment (MIBEX) using a simulated mine. During the experiment, mine track and mine burial depth were observed. The Navy's Impact Burial Prediction Model (IBPM) was used to create a two-dimensional time

history for a bottom mine as it falls through air, water, and sediment. The output of the model is the predicted burial depth of the mine in the sediment, as well as height, area, and volume protruding. Model input consists of environmental parameters and mine characteristics, as well as parameters describing the mine's release. The MIBEX data show that the current IBPM model needs to be improved by considering more DOFs. Chu et al. (2005; 2006; 2009) developed a 3D motion program, IMPACT35, to simulate objects falling through a single fluid (e.g, air, water and sediment) and through the interface of different fluids (air-water and water-sediment interface). In the equations of motion, apparent torque was ignored due to the use of a rotating coordinate system. Drag, lift force, and moments were linearized with temporally varying coefficients in the time domain. Chu et al. (2005; 2006; 2009) report the trajectories of falling cylinders from experiments with variations of mass center, initial velocity, and drop angle. IMPACT35 has been validated by comparing its results with experimental data. LCG, initial velocity, and drop angle are found to be critical factors influencing the trajectories of dropped objects. Chu et al. (2005) conducted the experiment as shown in Fig. 2.3 consisting of dropping three cylinders of various lengths into NPS swim pool where the trajectories were recorded from two cameras at different angles as shown in Fig. 2.4. The controlled parameters are the cylinder's physical parameters (length to diameter ratio, center of mass location), and initial drop conditions (initial velocity,and drop angle).

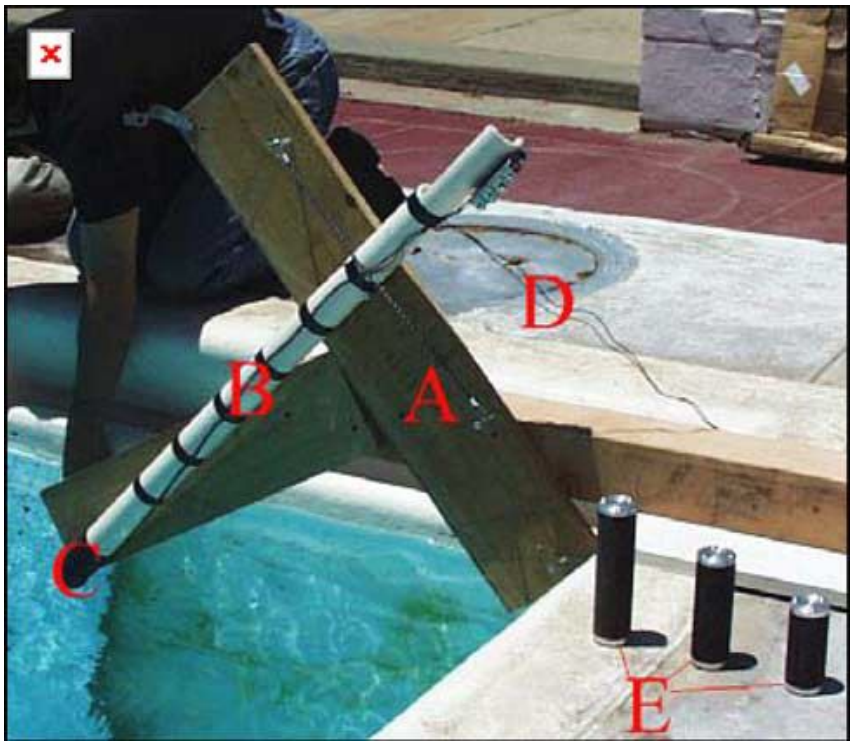

Fig. 2.3. Experimental equipments: (A) drop angle device, (B) cylinder injector, (C) infrared light sensor, (D) output to universal counter, and (E) cylinders.(Chu et al.2005; 2006)

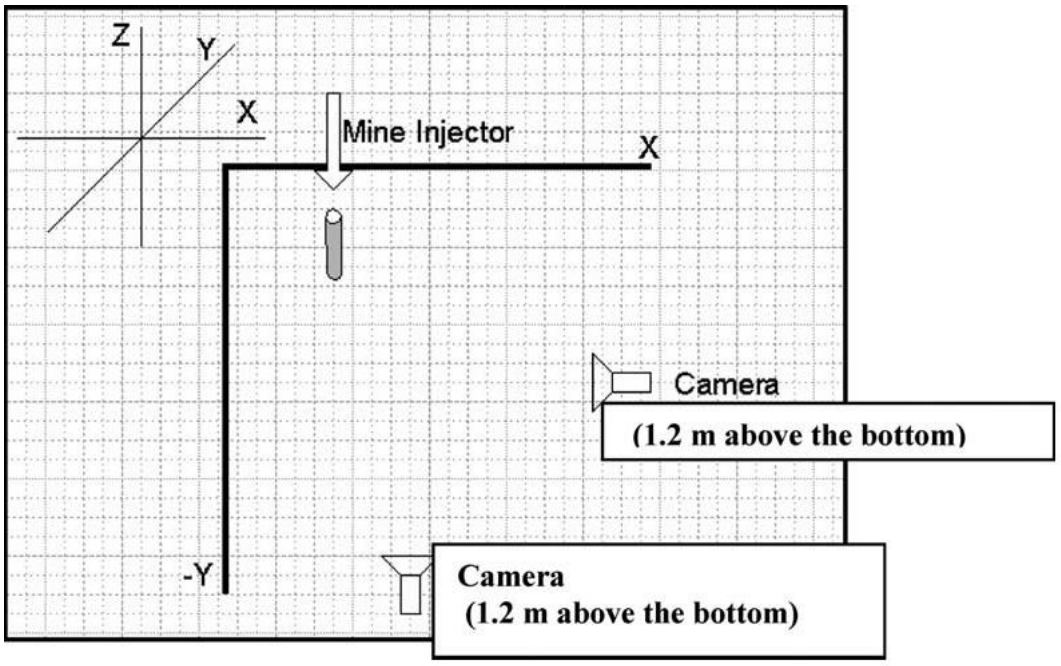

Fig. 2.4. Top view of the cylinder drop experiment.(Chu et al. .2005; 2006)

Mazzola (2000) built up a probabilistic model for the estimation of the pipeline impact and rupture frequencies. This information is obtained both for the overall pipeline section exposed to the hazard and for a number of critical locations along the pipeline route. The presented algorithm has been implemented in a computer program that allows the analysis of a large number of possible landing points and pipeline target point locations based on normal distribution. In particular, two sample cases have been analyzed. The first one is the problem of selecting the best approaching route to a platform. The second application deals with the selection of the location for a safety valve at the riser base.

Majed and Cooper (2013) presented nonlinear dynamic simulations of dropped objects for a detailed and accurate assessment of dropped object trajectories by incorporating detailed 3D hydrodynamic models of complex object geometries. In addition, the entire impact zone is determined using Monte-Carlo simulations which consider the object's initial drop angle to be the random variable.

Yasseri (2014) experimentally investigated the falling of model-scale cylinders through water with low initial entry velocity and concluded that the landing location of free-falling cylinders is within 10% of the water depth with 50% of probability, within 20% of the water depth with 80% of probability, within 30% of the water depth with 90% of probability, within 40%

of the water depth with 95% of probability, and within 50% of the water depth with 98% of probability.

Awotahegn (2015) performed a series of model tests (1:16.67,1:33.3) to investigate the trajectory and seabed distribution of two drill pipes with two diameters in full scale, 8″ and 12″ falling from defined heights above the water surface. He plotted and analyzed the maximum excursion points and the seabed landing points. After comparing them with the results from a simplified method by DNV (2010), Awotahegn (2015) concluded that the methodology recommended by DNV (2010) is generally conservative.

In my work, based on the traditional 2D theory, a new 3D theory is extended and established to consider the complete 6DOF motions of dropped cylinders into water. Drag coefficients are updated at each time step as per Reynolds number. Lift force because of rolling rotation are also considered. More factors like rolling frequencies, drag coefficient in Y direction, etc are found to influence the trajectories of dropped cylinders. By comparing the new 3D theory to traditional 3D theory, the trailing edge effect of long cylinders is considered by potential flow theory for a slender body instead of expensive laboratory tests or direct neglect. Also, environmental conditions including current and physical properties of the dropped cylinder like mass distribution are quantitatively studied and found to have a great influence on the trajectories and landing points of the dropped cylinder. Other than study on the deterministic 3D theory of the dropped cylinder, a stochastic model is combined with the new 3D theory to study the landing point distribution and impact energy distribution on the sea bed. At the same time, the definition of risk free zone is firstly proposed in Ocean Engineering industry.

Chapter 3

2D theory of dropped cylinderical object

3.1 2D Equations of motion for rigid body

Aanesland (1987) used a computer program to investigate falling drilling pipes. This program solves a set of two-dimensional (2D) maneuvering equations which describe the motions of drilling pipes, in which the trailing edge effect for a long slender body has been considered and further corrected for viscous effects . Two coordinate systems are used in the two-dimensional (2D) theory as shown in Fig. 3.1. Firstly, OXZ is the global coordinate system, where X-axis represents the still-water surface and Z-axis points vertical upwards. The other coordinate system is a local coordinate system - oxz which is fixed on the cylinder, where the x-axis is aligned with the cylinder's axis. Its origin o is assumed to be located at the center of gravity of the cylinder. Both coordinate systems OXZ and oxz coincide when the cylinder is horizontally situated on the water surface in the beginning.

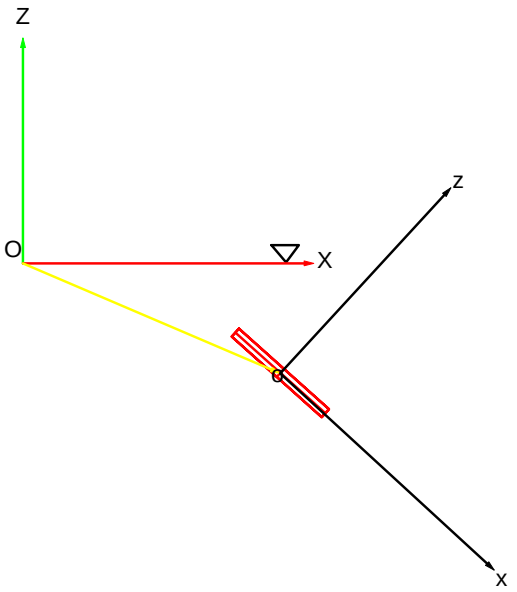

Fig. 3.1. Coordinate system for equation of motions in two dimensions

In Aanesland's (1987) paper, the cylinder is assumed to be rigid and slender. Its mass distribution is uniform. Therefore, its mass center and geometric center coincide. Since Aanesland (1987) simplified the problem into a 2D problem, only motions in the x-z plane are considered. The velocity components are U_1 (surge), U_3 (heave), and Ω_2 (pitch). The equation of motions are given as:

$$(m - \rho\nabla)g\sin(\beta) + F_{dx} = m\dot{U}_1 \tag{3.1}$$

$$-(m - \rho\nabla)g\cos(\beta) + F_{dz} = \{U_1 m_t U_3 - U_1(x_t m_t)\Omega_2\} + m_{33}\dot{U}_3 + m(\dot{U}_3 - U_1\Omega_2) \tag{3.2}$$

$$M_{dy} = \{-U_1(m_{33} + x_t m_t)U_3 + U_1 {x_t}^2 m_t \Omega_2\} + m_{55}\dot{\Omega}_2 + I_{55}\dot{\Omega}_2 \tag{3.3}$$

It should be noted that the motions in the above equations are stated in the body-fixed coordinate system oxz. The first two equations represent the force equilibrium in x and z direction while the last equation shows the moment equilibrium with respect to y-axis.

3.1.1 Hydrodynamic force and moment in potential theory

Terms in curly brackets on the right side of the Eqs. (3.2) and (3.3) are hydrodynamic force and moment derived from potential theory (Newman, 1977). Hydrodynamic force refers to added mass force and an additional force component to consider the trailing edge effect of the cylinder in Eqs. (3.1) and (3.3). This trailing edge effect is determined by longitudinal position of effective trailing edge, x_t and 2D added mass coefficients at the trailing edge m_t. At last, the total hydrodynamics force is derived by integrating Eq. (3.4) which is initially used to calculate differential lateral force acting along the swimming motion of slender fish by Lighthill (1960) over the length of the cylinder.

$$F_z' = -\left(\frac{\partial}{\partial t} - U\frac{\partial}{\partial x}\right)[W(x,t)m_{33}(x)] \tag{3.4}$$

The lateral added-mass coefficient, due to acceleration of a rigid body in the z-direction, is given by the integral

$$m_{33} = \int_l M_{33}(x)\mathrm{d}x \tag{3.5}$$

Similarly,

$$m_{35} = -\int_l M_{33}(x)x\mathrm{d}x \tag{3.6}$$

and

$$m_{55} = \int_l M_{33}(x)x^2\mathrm{d}x \tag{3.7}$$

The total force acting on a slender body can be derived by integrating the differential force,

$$\begin{aligned} F_z &= \int_l -\dot{W}(x,t)M_{33}(x)\mathrm{d}x + U\int_l \frac{\partial}{\partial x}[W(x,t)M_{33}(x)]\mathrm{d}x \\ &= \int_l -\dot{W}(x,t)M_{33}(x)\mathrm{d}x + U\Big[W(x,t)M_{33}(x)\Big]_{x_t}^{x_n} \end{aligned} \tag{3.8}$$

In Eqs. (3.2)-(3.3), longitudinal position of effective trailing edge x_t is introduced from Newman (1977). And x_n is the longitudinal location of nose.

The yaw moment about the vertical axis of the body can be obtained by multiplying Eq. (3.4) by the arm -x and integrating over the length.

$$\begin{aligned} M_y &= \int_l \dot{W}(x,t)M_{33}(x)x\mathrm{d}x - U\int_l \frac{\partial}{\partial x}[W(x,t)M_{33}(x)]x\mathrm{d}x \\ &= \int_l \dot{W}(x,t)M_{33}(x)x\mathrm{d}x - U\left\{x\Big[W(x,t)M_{33}(x)\Big]\right\}_{x_t}^{x_n} + U\int_l [W(x,t)M_{33}(x)\mathrm{d}x \end{aligned} \tag{3.9}$$

The first term stands for the unsteady term. The second term is associated with the moment due to the lift force on the tail fin and vanishes for a body with a pointed tail. The last term is the Munk moment, which gives a contribution for a body moving at an angle of attack, regardless of whether the tail is pointed.

$$W(x,t) = U_3(t) - x\Omega_2(t) \tag{3.10}$$

For a slender body, the nose is a point of zero transverse dimensions, and thus $M_{33}(x_n) = 0$. The same will be true without a tail fin, $M_{33}(x_t) = 0$ at the tail for a pointed body; In accordance with D'Alembert's paradox, the lateral force acting on such a body in steady motion is zero. But the ends of the cylinder are not pointed, i.e. $M_{33}(x_t) \neq 0$. An additional force component is included to consider this trailing edge effect for a long slender body as shown in curly brackets on the right side of the Eqs. (3.2) - (3.3) (Newman, 1977) .

Bring the Eq. (3.10) into Eqs. (3.8) - (3.9):

$$F_z = -\dot{U}_3 m_{33} - \dot{\Omega}_2 m_{35} - U_1 U_3 M_{33}(x_t) + U_1 \Omega_2 x_t M_{33}(x_t) \tag{3.11}$$

$$M_y = -\dot{U}_3 m_{35} - \dot{\Omega}_2 m_{55} + U_1 U_3 [m_{33} + x_t M_{33}(x_t)] + U_1 \Omega_2 [m_{35} - (x_t)^2 M_{33}(x_t)] \tag{3.12}$$

3.1.2 Viscosity

In addition, the viscous forces and moment, F_{dx}, F_{dz} and M_{dy}, are evaluated with a Morison equation type approach:

$$F_{dx} = 0.664\pi\sqrt{\nu\rho^2 L}U_1\sqrt{|U_1|} + \frac{1}{8}\rho\pi C_{dx} D^2 U_1 |U_1| \tag{3.13}$$

$$F_{dz} = 0.5\int_{-0.5L}^{0.5L} \rho C_{dz} D U_z(x)|U_z(x)|\mathrm{d}x \tag{3.14}$$

$$M_{dy} = -0.5\int_{-0.5L}^{0.5L} \rho C_{dz} D x U_z(x)|U_z(x)|\mathrm{d}x \tag{3.15}$$

The first term in Eq. (3.13) represents the frictional drag which can be obtained from boundary layer theory (Schlichting, 1979) and the second term represents a form drag component (Hoerner, 1958). Morison equation (Gudmestad and Moe, 1996) is used in Eqs. (3.14) and (3.15),

and the unknown parameter $U_z(x)$ is the local relative water to cylinder velocity in z-axis direction . It may be represented as

$$U_z(x) = -(U_3 - \Omega_2 x), -0.5L < x < 0.5L \tag{3.16}$$

When we substitute Eq. (3.16) into Eqs. (3.14) and (3.15), we obtain

$$\begin{aligned} F_{dz} &= 0.5 \int_{-0.5L}^{0.5L} \rho C_{dz} D U_z(x)|U_z(x)|\mathrm{d}x \\ &= 0.5\rho C_{dz} D \int_{-0.5L}^{0.5L} -(U_3 - \Omega_2 x)|U_3 - \Omega_2 x|\mathrm{d}x \end{aligned} \tag{3.17}$$

$$\begin{aligned} M_{dy} &= -0.5 \int_{-0.5L}^{0.5L} \rho C_{dz} D x U_z(x)|U_z(x)|\mathrm{d}x \\ &= 0.5\rho C_{dz} D \int_{-0.5L}^{0.5L} x(U_3 - \Omega_2 x)|U_3 - \Omega_2 x|\mathrm{d}x \end{aligned} \tag{3.18}$$

3.1.3 Transformation of coordinate system

In the numerical simulation, U_1, U_3 and Ω_2 are solved at each time step. The motions in body fixed coordinate system can be transformed to the motions in the inertial system. However , let's do the transformation from inertial system to body fixed coordinate system first, which is expressed by a rotation matrix α , that transforms the vector coordinates of inertial system to the body fixed coordinate system. Then, consider the following xz plane rotations: rotation around axis y; the corresponding angle is β for pitch motion, being a precession Euler angle; The new direction of the associated unit vector for axis x and axis z after precession can be expressed in terms of its components along the axes of the inertial system:

$$\begin{bmatrix} \vec{i} \\ \vec{k} \end{bmatrix} = \alpha \begin{bmatrix} \vec{i}_O \\ \vec{k}_O \end{bmatrix} = \begin{bmatrix} \cos\beta & -\sin\beta \\ \sin\beta & \cos\beta \end{bmatrix} \begin{bmatrix} \vec{i}_O \\ \vec{k}_O \end{bmatrix} \tag{3.19}$$

multiply both sides of Eq. (3.19) by $\begin{bmatrix} U_1 & U_3 \end{bmatrix}$

$$\begin{aligned}\begin{bmatrix} U_1 & U_3 \end{bmatrix} \begin{bmatrix} \vec{i} \\ \vec{k} \end{bmatrix} &= \begin{bmatrix} U_1 & U_3 \end{bmatrix} (\alpha \begin{bmatrix} \vec{i}_O \\ \vec{k}_O \end{bmatrix}) \\ &= (\begin{bmatrix} U_1 & U_3 \end{bmatrix} \begin{bmatrix} \cos\beta & -\sin\beta \\ \sin\beta & \cos\beta \end{bmatrix}) \begin{bmatrix} \vec{i}_O \\ \vec{k}_O \end{bmatrix} \\ &= \begin{bmatrix} \dot{X} & \dot{Z} \end{bmatrix} \begin{bmatrix} \vec{i}_O \\ \vec{k}_O \end{bmatrix}\end{aligned} \tag{3.20}$$

Then

$$\dot{X} = U_1 \cos(\beta) + U_3 \sin(\beta) \tag{3.21}$$

$$\dot{Z} = -U_1 \sin(\beta) + U_3 \cos(\beta) \tag{3.22}$$

$$\dot{\beta} = \Omega_2 \tag{3.23}$$

Because axis Y and axis y are parallel, then the rotation speed of dropped cylinder around axis Y and axis y are the same. (Eq. (3.23))

3.2 Simulated trajectories of dropped cylindrical objects using 2D theory

A drilling pipe model from Aanesland (1987) is selected as the dropped cylindrical object in this study. Its properties are summarized in Table 3.1. Figs. 3.2, 3.4, and 3.6 show results of

Table 3.1: Property of the Cylinder

Parameters	Unit	Full Scale	Model Scale(1:20.32)
Length (L)	m	9.95	0.450
Mass density (ρ_c)	kg/m	225	0.548
Diameter	m	0.203	0.010

trajectories from experiments and simulations by Aanesland (1987). Several trajectories are shown for initial drop angle of 30^o, 45^o, and 60^o which is represented by dashed curves determining an experimental envelope as well as solid lines from numerical simulations. Figs. 3.3, 3.5, and 3.7 show the simulation results based on the 2D theory have been reproduced by Xiang et al. (2017). It is obvious that there is a good agreement between current numerical results and the experimental/numerical results given by Aanesland (1987).

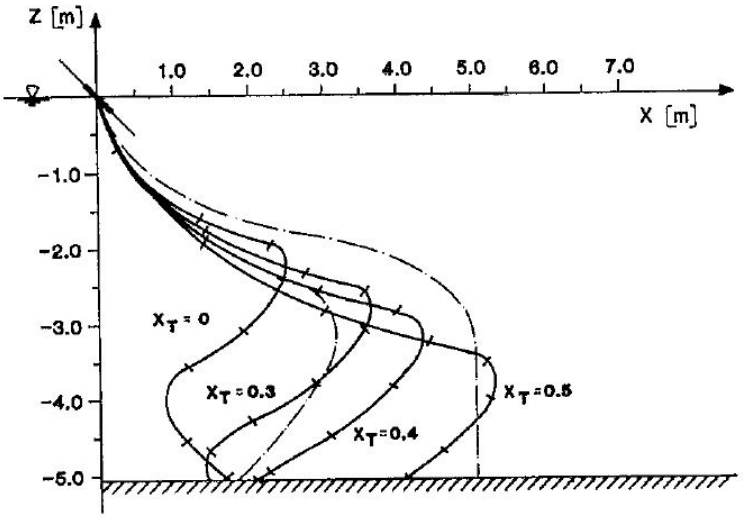

Fig. 3.2. Simulated trajectory and experimental envelope at drop angle 45^o, $C_{dz} = 1.0$, by Aanesland (1987)

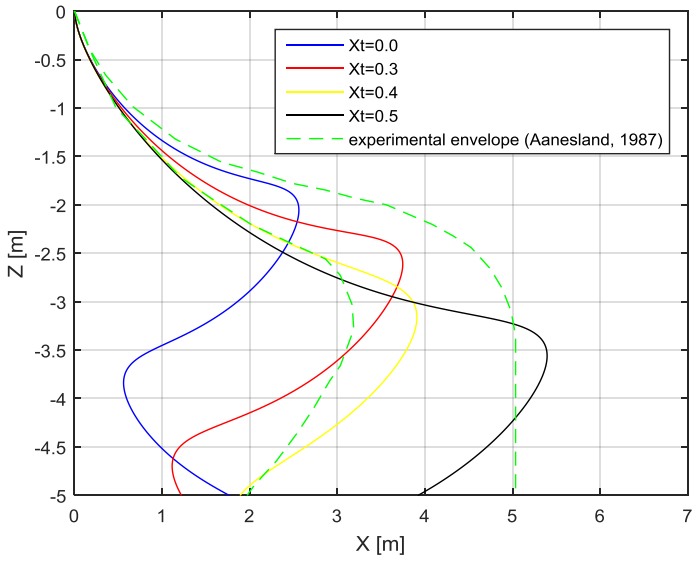

Fig. 3.3. Comparison of repeated simulated trajectory at drop angle 45^o, $C_{dz} = 1.0$, with experimental envelope by Aanesland (1987)

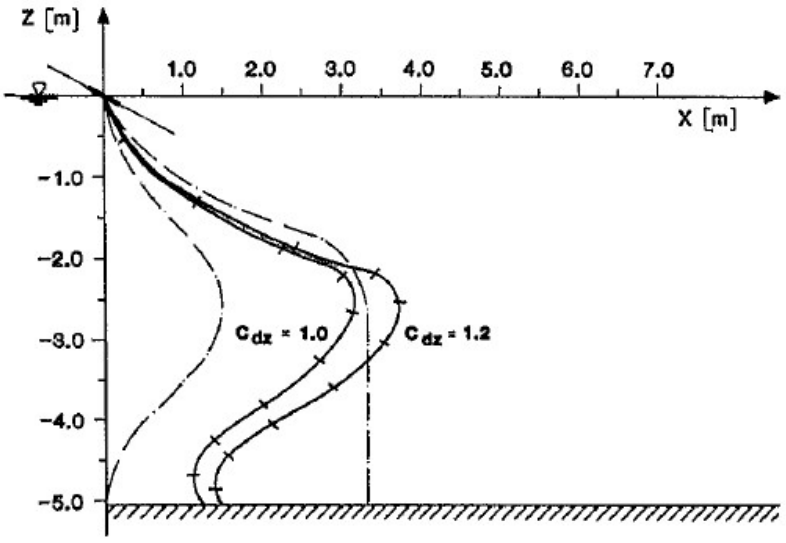

Fig. 3.4. Simulated trajectory and experimental envelope at drop angle 30^o, Xt=0.4, by Aanesland (1987)

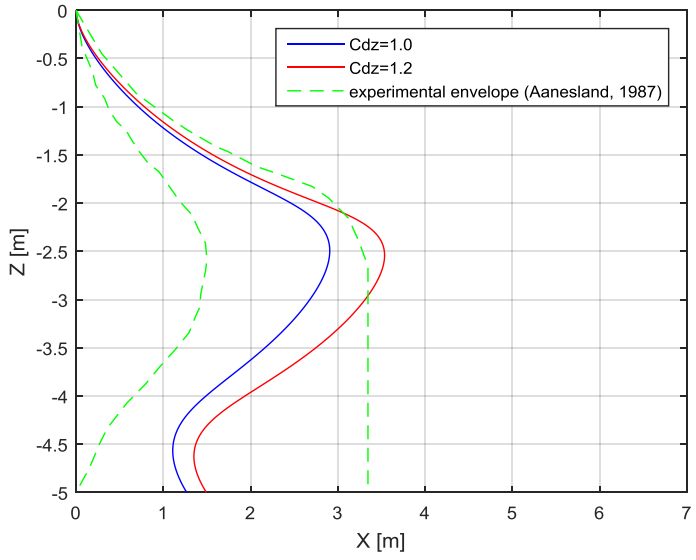

Fig. 3.5. Comparison of repeated simulated trajectory at drop angle 30^o, Xt=0.4, with experimental envelope by Aanesland (1987)

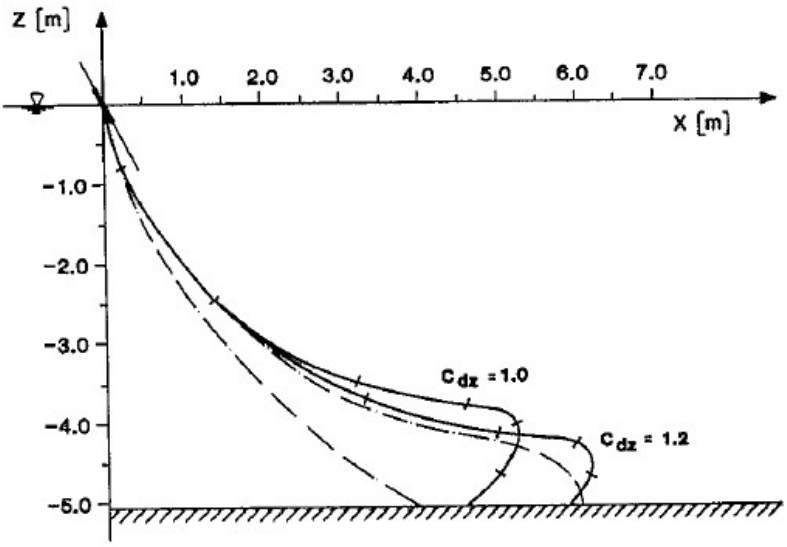

Fig. 3.6. Simulated trajectory and experimental envelope at drop angle 60^o, Xt=0.4, by Aanesland (1987)

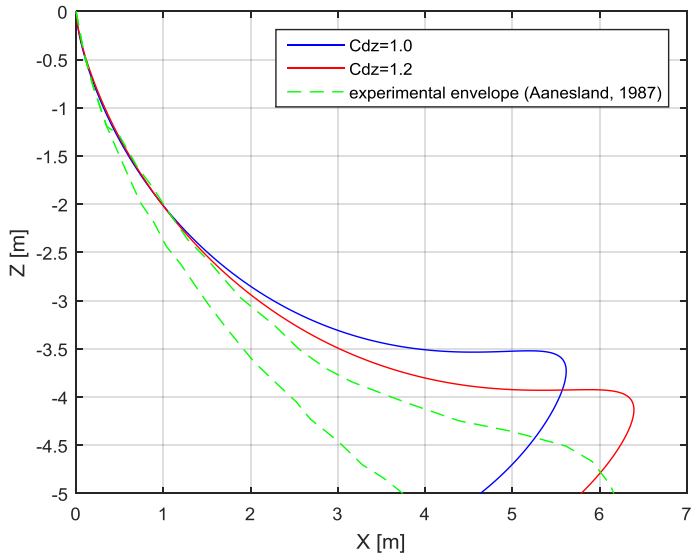

Fig. 3.7. Comparison of repeated simulated trajectory at drop angle 60^o, Xt=0.4, with experimental envelope by Aanesland (1987)

Chapter 4

3D theory of dropped cylinderical object

4.1 3D Equations of motion of rigid body

Xiang et al. (2017) proposed a new three-dimensional (3D) theory to consider the effect of axial rotation on dropped cylindrical objects by modifying the maneuvering equations for a slender rigid body and adding nonlinear kinematics and dynamics of a rigid body. A numerical tool called Dropped Objects Simulator (DROBS) has been successfully developed based on this 3D theory to investigate various factors that may affect the trajectories, including drop angle, normal drag coefficient, binormal drag coefficient and rolling frequency.

4.1.1 Rigid body kinematics

Assume that the origin o of the body fixed system ($oxyz$) moves with translational velocity $\vec{V}_o$ and rotational speed $\vec{\Omega}_o$ with respect to inertial system ($OXYZ$). The vector $\vec{V}_o$ and $\vec{\Omega}_o$ can be expressed in terms of their components along $\vec{i}$, $\vec{j}$,and $\vec{k}$, the unit vectors of the body fixed system.

$$\vec{V}_o = u\vec{i} + v\vec{j} + w\vec{k} \tag{4.1}$$

$$\vec{\Omega}_o = p\vec{i} + q\vec{j} + r\vec{k} \tag{4.2}$$

u, v and w are the amplitudes of the velocity components of $\vec{V}_o$ along $\vec{i}$, $\vec{j}$, $\vec{k}$; p, q and r are the amplitudes of the velocity components of $\vec{\Omega}_o$ around $\vec{i}$, $\vec{j}$ and $\vec{k}$.

The acceleration of the body at the origin o of the body fixed system can be expressed by

$$\vec{a}_o = \dot{u}\vec{i} + u\frac{\mathrm{d}\vec{i}(t)}{\mathrm{d}t} + \dot{v}\vec{j} + v\frac{\mathrm{d}\vec{j}(t)}{\mathrm{d}t} + \dot{w}\vec{k} + w\frac{\mathrm{d}\vec{k}(t)}{\mathrm{d}t} \tag{4.3}$$

and with Eqs. (4.4) - (4.6) following

$$\frac{\mathrm{d}\vec{i}(t)}{\mathrm{d}t} = \vec{\Omega}_o \times \vec{i} \tag{4.4}$$

$$\frac{\mathrm{d}\vec{j}(t)}{\mathrm{d}t} = \vec{\Omega}_o \times \vec{j} \tag{4.5}$$

$$\frac{\mathrm{d}\vec{k}(t)}{\mathrm{d}t} = \vec{\Omega}_o \times \vec{k} \tag{4.6}$$

The following can be derived:

$$\frac{\mathrm{d}\vec{i}(t)}{\mathrm{d}t} = r\vec{j} - q\vec{k} \tag{4.7}$$

$$\frac{\mathrm{d}\vec{j}(t)}{\mathrm{d}t} = -r\vec{i} + p\vec{k} \tag{4.8}$$

$$\frac{\mathrm{d}\vec{k}(t)}{\mathrm{d}t} = q\vec{i} - p\vec{j} \tag{4.9}$$

By substituting Eqs. (4.7) - (4.9) into Eqs. (4.3)

$$\vec{a}_o = (\dot{u} - vr + wq)\vec{i} + (\dot{v} + ur - wp)\vec{j} + (\dot{w} - uq + vp)\vec{k} \tag{4.10}$$

4.1.2 Rigid body dynamics

If the mass of a rigid body is uniformly distributed, the mass center G will be at o, the origin of the body fixed system. Based on Newton's Second Law:

$$F_e = m\vec{a}_G = m\vec{a}_o \tag{4.11}$$

F_e is the total external force acting on the mass center, G which may be split into its components.

$$F_e = F_{ex}\vec{i} + F_{ey}\vec{j} + F_{ez}\vec{k} \tag{4.12}$$

Substituting Eqs. (4.12) and (4.10) into Eq. (4.11) yields:

$$\begin{aligned} F_{ex}\vec{i} + F_{ey}\vec{j} + F_{ez}\vec{k} =& m[(\dot{u} - vr + wq)\vec{i} \\ &+ (\dot{v} + ur - wp)\vec{j} \\ &+ (\dot{w} - uq + vp)\vec{k}] \end{aligned} \tag{4.13}$$

Let $\vec{R}_{Oo}$ be the distance vector from the origin of the inertial system to the origin of the body fixed system. The time rate of the angular momentum for the rigid body can be expressed as:

$$\frac{\mathrm{d}}{\mathrm{d}t}[\Sigma(\vec{R}_{Oo} + \vec{R}_i) \times m_i(\vec{V}_o + \vec{\Omega}_o \times \vec{R}_i)] \tag{4.14}$$

If the moment of the external force is calculated with respect to the body fixed system, then $\vec{R}_{Oo} = 0$ and the time rate of the angular momentum for the rigid body can be expressed as:

$$\begin{aligned} &\frac{\mathrm{d}}{\mathrm{d}t}[\Sigma\vec{R}_i \times m_i(\vec{V}_o + \vec{\Omega}_o \times \vec{R}_i)] \\ &= m\vec{R}_G \times \vec{a}_o + \Sigma[m_i\vec{R}_i \times (\dot{\vec{\Omega}}_o \times \vec{R}_i)] + \Sigma\{m_i\vec{R}_i \times [\vec{\Omega}_o \times (\vec{\Omega}_o \times \vec{R}_i)]\} \\ &= m\vec{R}_G \times \vec{a}_o + \dot{\vec{\Omega}}_o(\Sigma\, m_i\vec{R}_i \cdot \vec{R}_i) - (\Sigma\, m_i\vec{R}_i\vec{R}_i) \cdot \dot{\vec{\Omega}}_o + \dot{\vec{\Omega}}_o \cdot (\Sigma\, m_i\vec{R}_i\vec{R}_i) \times \vec{\Omega}_o \\ &= \dot{\vec{\Omega}}_o(\Sigma\, m_i\vec{R}_i \cdot \vec{R}_i) - (\Sigma\, m_i\vec{R}_i\vec{R}_i) \cdot \dot{\vec{\Omega}}_o + \dot{\vec{\Omega}}_o \cdot (\Sigma\, m_i\vec{R}_i\vec{R}_i) \times \vec{\Omega}_o \end{aligned} \tag{4.15}$$

The term $\Sigma\, m_i\vec{R}_i\vec{R}_i$ is the dyadic product of the vector $\vec{R}_i$ by itself. It can be written as a second order tensor:

$$\begin{aligned}\Sigma\, m_i\vec{R}_i\vec{R}_i =& \Sigma\, m_i \begin{bmatrix}\vec{i} & \vec{j} & \vec{k}\end{bmatrix} \begin{bmatrix}x_i\\ y_i\\ z_i\end{bmatrix} \begin{bmatrix}x_i & y_i & z_i\end{bmatrix} \begin{bmatrix}\vec{i}\\ \vec{j}\\ \vec{k}\end{bmatrix}\\ &= \begin{bmatrix}\vec{i} & \vec{j} & \vec{k}\end{bmatrix} \Sigma\, m_i \begin{bmatrix}x_i^2 & x_iy_i & x_iz_i\\ x_iy_i & y_i^2 & y_iz_i\\ x_iz_i & y_iz_i & z_i^2\end{bmatrix} \begin{bmatrix}\vec{i}\\ \vec{j}\\ \vec{k}\end{bmatrix}\\ &= \begin{bmatrix}\vec{i} & \vec{j} & \vec{k}\end{bmatrix} \begin{bmatrix}I_{xx} & I_{xy} & I_{xz}\\ I_{yx} & I_{yy} & I_{yz}\\ I_{zx} & I_{zy} & I_{zz}\end{bmatrix} \begin{bmatrix}\vec{i}\\ \vec{j}\\ \vec{k}\end{bmatrix}\end{aligned} \tag{4.16}$$

The term$\Sigma\, m_i\vec{R}_i \cdot \vec{R}_i$ is the dot product of vector $\vec{R}_i$ by itself. It also can be written as a second order tensor:

$$\begin{aligned}\Sigma\, m_i\vec{R}_i \cdot \vec{R}_i &= \begin{bmatrix}\vec{i} & \vec{j} & \vec{k}\end{bmatrix} \Sigma\, m_i(x_i^2+y_i^2+z_i^2) \begin{bmatrix}1 & 0 & 0\\ 0 & 1 & 0\\ 0 & 0 & 1\end{bmatrix} \begin{bmatrix}\vec{i}\\ \vec{j}\\ \vec{k}\end{bmatrix}\\ &= \begin{bmatrix}\vec{i} & \vec{j} & \vec{k}\end{bmatrix} \begin{bmatrix}I_x+I_{xx} & 0 & 0\\ 0 & I_y+I_{yy} & 0\\ 0 & 0 & I_z+I_{zz}\end{bmatrix} \begin{bmatrix}\vec{i}\\ \vec{j}\\ \vec{k}\end{bmatrix}\end{aligned} \tag{4.17}$$

where, $I_x = \Sigma\, m_i(y_i^2+z_i^2), I_y = \Sigma\, m_i(x_i^2+z_i^2), I_z = \Sigma\, m_i(x_i^2+y_i^2)$ are the mass moments of inertia of the body around axes x, y and z, respectively; $I_{xy} = I_{yx} = \Sigma\, m_ix_iy_i, I_{xz} = I_{zx} = \Sigma\, m_ix_iz_i, I_{yz} = I_{zy} = \Sigma\, m_iy_iz_i, I_{xx} = \Sigma\, m_ix_i^2, I_{yy} = \Sigma\, m_iy_i^2, I_{zz} = \Sigma\, m_iz_i^2$ are the mass products of inertia of the body.

Based on Newton's Second Law:

$$M_e = \frac{\mathrm{d}}{\mathrm{d}t}[\Sigma\vec{R}_i \times m_i(\vec{V}_o + \vec{\Omega}_o \times \vec{R}_i)] \tag{4.18}$$

M_e is the total moment of external forces with respect to body fixed system, which may be split into its components.

$$M_e = M_{ex}\vec{i} + M_{ey}\vec{j} + M_{ez}\vec{k} \tag{4.19}$$

Substituting Eqs. (4.19) and (4.15) into Eq. (4.18) results in,

$$\begin{aligned} M_{ex}\vec{i} + M_{ey}\vec{j} + M_{ez}\vec{k} =& m\Big\{[I_x\dot{p} - I_{xy}(\dot{q} - pr) - I_{xz}(\dot{r} + pq) + I_{yz}(r^2 - q^2) + (I_z - I_y)qr]\vec{i} \\ &+ [I_y\dot{q} - I_{yx}(\dot{p} + qr) - I_{yz}(\dot{r} - pq) + I_{xz}(p^2 - r^2) + (I_x - I_z)pr]\vec{j} \\ &+ [I_z\dot{r} - I_{zx}(\dot{p} - qr) - I_{zy}(\dot{q} + pr) + I_{xy}(q^2 - p^2) + (I_y - I_x)pq]\vec{k}\Big\} \end{aligned} \tag{4.20}$$

4.1.3 Transformation of coordinate system

The transformation between body fixed system ($oxyz$) and inertial system ($OXYZ$) can be expressed as a sequence of partial rotations where each rotation is done with respect to the preceding one (John and Francis, 1962). Then, consider the following sequential plane rotations:

- rotation around axis z ; the corresponding angle is for the yaw motion, being a precession Euler angle; the new direction assumed by axis y after precession is taken as the nutation axis and named n; the associated unit vector can be expressed either in terms of its components along the axes of the inertial system or along the body fixed axes:

$$\begin{bmatrix} \vec{i}_1 \\ \vec{j}_1 \\ \vec{k}_1 \end{bmatrix} = \alpha_\psi \begin{bmatrix} \vec{i}_O \\ \vec{j}_O \\ \vec{k}_O \end{bmatrix} = \begin{bmatrix} \cos\psi & \sin\psi & 0 \\ -\sin\psi & \cos\psi & 0 \\ 0 & 0 & 1 \end{bmatrix} \begin{bmatrix} \vec{i}_O \\ \vec{j}_O \\ \vec{k}_O \end{bmatrix} \tag{4.21}$$

- rotation around the nutation axis n as defined in the above item; the corresponding angle is for the pitch motion, being a nutation Euler angle

$$\begin{bmatrix} \vec{i}_2 \\ \vec{j}_2 \\ \vec{k}_2 \end{bmatrix} = \alpha_\theta \begin{bmatrix} \vec{i}_1 \\ \vec{j}_1 \\ \vec{k}_1 \end{bmatrix} = \begin{bmatrix} \cos\theta & 0 & -\sin\theta \\ 0 & 1 & 0 \\ \sin\theta & 0 & \cos\theta \end{bmatrix} \begin{bmatrix} \vec{i}_1 \\ \vec{j}_1 \\ \vec{k}_1 \end{bmatrix} \tag{4.22}$$

- rotation around the body fixed axis x; the corresponding angle is for the roll motion, being a self rotation Euler angle

$$\begin{bmatrix} \vec{i} \\ \vec{j} \\ \vec{k} \end{bmatrix} = \alpha_\phi \begin{bmatrix} \vec{i}_2 \\ \vec{j}_2 \\ \vec{k}_2 \end{bmatrix} = \begin{bmatrix} 1 & 0 & 0 \\ 0 & \cos\phi & \sin\phi \\ 0 & -\sin\phi & \cos\phi \end{bmatrix} \begin{bmatrix} \vec{i}_2 \\ \vec{j}_2 \\ \vec{k}_2 \end{bmatrix} \tag{4.23}$$

Substitution of Eq. (4.21) into Eq. (4.22) and Eq. (4.22) into Eq result in (4.23),

$$\begin{bmatrix} \vec{i} \\ \vec{j} \\ \vec{k} \end{bmatrix} = \alpha_\phi \alpha_\theta \alpha_\psi \begin{bmatrix} \vec{i}_O \\ \vec{j}_O \\ \vec{k}_O \end{bmatrix} = \begin{bmatrix} 1 & 0 & 0 \\ 0 & \cos\phi & \sin\phi \\ 0 & -\sin\phi & \cos\phi \end{bmatrix} \begin{bmatrix} \cos\theta & 0 & -\sin\theta \\ 0 & 1 & 0 \\ \sin\theta & 0 & \cos\theta \end{bmatrix} \begin{bmatrix} \cos\psi & \sin\psi & 0 \\ -\sin\psi & \cos\psi & 0 \\ 0 & 0 & 1 \end{bmatrix} \begin{bmatrix} \vec{i}_O \\ \vec{j}_O \\ \vec{k}_O \end{bmatrix} \tag{4.24}$$

The matrix product is combined into the transformation matrix α,

$$\alpha = \begin{bmatrix} 1 & 0 & 0 \\ 0 & \cos\phi & \sin\phi \\ 0 & -\sin\phi & \cos\phi \end{bmatrix} \begin{bmatrix} \cos\theta & 0 & -\sin\theta \\ 0 & 1 & 0 \\ \sin\theta & 0 & \cos\theta \end{bmatrix} \begin{bmatrix} \cos\psi & \sin\psi & 0 \\ -\sin\psi & \cos\psi & 0 \\ 0 & 0 & 1 \end{bmatrix} \tag{4.25}$$

Next, we multiply both sides of Eq. (4.24) by $\begin{bmatrix} u & v & w \end{bmatrix}$ from the left:

$$\begin{aligned} \begin{bmatrix} u & v & w \end{bmatrix} \begin{bmatrix} \vec{i} \\ \vec{j} \\ \vec{k} \end{bmatrix} &= \begin{bmatrix} u & v & w \end{bmatrix} \left(\alpha \begin{bmatrix} \vec{i}_O \\ \vec{j}_O \\ \vec{k}_O \end{bmatrix} \right) \\ &= \left(\begin{bmatrix} u & v & w \end{bmatrix} \alpha \right) \begin{bmatrix} \vec{i}_O \\ \vec{j}_O \\ \vec{k}_O \end{bmatrix} \\ &= \begin{bmatrix} \dot{X} & \dot{Y} & \dot{Z} \end{bmatrix} \begin{bmatrix} \vec{i}_O \\ \vec{j}_O \\ \vec{k}_O \end{bmatrix} \end{aligned} \tag{4.26}$$

The component of the vector in Eq. (4.26) can be expressed as:

$$\begin{aligned}\dot{X} =& u\cos(\theta)\cos(\psi) + v(-\cos(\phi)\sin(\psi) + \sin(\phi)\sin(\theta)\cos(\psi)) \\ &+ w(\sin(\phi)\sin(\psi) + \cos(\phi)\sin(\theta)\cos(\psi))\end{aligned} \tag{4.27}$$

$$\begin{aligned}\dot{Y} =& u\cos(\theta)\sin(\psi) + v(\cos(\phi)\cos(\psi) + \sin(\phi)\sin(\theta)\sin(\psi)) \\ &+ w(-\sin(\phi)\cos(\psi) + \cos(\phi)\sin(\theta)\sin(\psi))\end{aligned} \tag{4.28}$$

$$\dot{Z} = -u\sin(\theta) + v(-\sin(\phi)\cos(\theta)) + w(\cos(\phi)\cos(\theta)) \tag{4.29}$$

During the three rotations, $\vec{\Omega}_o$ can be expressed with respect to inertial system:

$$\vec{\Omega}_o = \dot{\psi}\vec{k}_O + \dot{\theta}\vec{n} + \dot{\phi}\vec{i} \tag{4.30}$$

Expressing $\vec{\Omega}_o$ in terms of body fixed coordinates yields:

$$\begin{aligned}\vec{\Omega}_o &= \dot{\psi}\begin{bmatrix}\vec{i}_O & \vec{j}_O & \vec{k}_O\end{bmatrix}\begin{bmatrix}0\\0\\1\end{bmatrix} + \dot{\theta}\begin{bmatrix}\vec{i} & \vec{n} & \vec{k}\end{bmatrix}\begin{bmatrix}0\\1\\0\end{bmatrix} + \dot{\phi}\begin{bmatrix}\vec{i} & \vec{j} & \vec{k}\end{bmatrix}\begin{bmatrix}1\\0\\0\end{bmatrix} \\ &= \begin{bmatrix}\vec{i} & \vec{j} & \vec{k}\end{bmatrix}\alpha\begin{bmatrix}0\\0\\\dot{\psi}\end{bmatrix} + \begin{bmatrix}\vec{i} & \vec{j} & \vec{k}\end{bmatrix}\alpha_\phi\begin{bmatrix}0\\\dot{\theta}\\0\end{bmatrix} + \begin{bmatrix}\vec{i} & \vec{j} & \vec{k}\end{bmatrix}\begin{bmatrix}\dot{\phi}\\0\\0\end{bmatrix} \\ &= \begin{bmatrix}\vec{i} & \vec{j} & \vec{k}\end{bmatrix}\{\begin{bmatrix}1 & 0 & 0\\0 & \cos\phi & \sin\phi\\0 & -\sin\phi & \cos\phi\end{bmatrix}\begin{bmatrix}\cos\theta & 0 & -\sin\theta\\0 & 1 & 0\\\sin\theta & 0 & \cos\theta\end{bmatrix}\begin{bmatrix}\cos\psi & \sin\psi & 0\\-\sin\psi & \cos\psi & 0\\0 & 0 & 1\end{bmatrix}\begin{bmatrix}0\\0\\\dot{\psi}\end{bmatrix} \\ &+ \begin{bmatrix}1 & 0 & 0\\0 & \cos\phi & \sin\phi\\0 & -\sin\phi & \cos\phi\end{bmatrix}\begin{bmatrix}0\\\dot{\theta}\\0\end{bmatrix} + \begin{bmatrix}\dot{\phi}\\0\\0\end{bmatrix}\} \\ &= \begin{bmatrix}\vec{i} & \vec{j} & \vec{k}\end{bmatrix}\left\{\begin{bmatrix}-\dot{\psi}\sin\theta\\\dot{\psi}\sin\phi\cos\theta\\\dot{\psi}\cos\phi\cos\theta\end{bmatrix} + \begin{bmatrix}0\\\dot{\theta}\cos\phi\\-\dot{\theta}\sin\phi\end{bmatrix} + \begin{bmatrix}\dot{\phi}\\0\\0\end{bmatrix}\right\}\end{aligned} \tag{4.31}$$

So after equaling Eq. (4.2) to Eq. (4.31), the final equations for p, q, and r are found

$$p = \dot{\phi} - \dot{\psi}\sin\theta \tag{4.32}$$

$$q = \dot{\psi} \sin\phi \cos\theta + \dot{\theta} \cos\phi \tag{4.33}$$

$$r = \dot{\psi} \cos\phi \cos\theta - \dot{\theta} \sin\phi \tag{4.34}$$

4.1.4 Equations of motion for dropped cylindrical object

In Fig. 4.1, $OXYZ$ is the global inertial coordinate system with unit vectors: $\vec{i_O}, \vec{j_O}$ and $\vec{k_O}$ in X, Y and Z directions respectively, where $X - Y$ represents the still-water surface and the Z-axis points vertical upwards. The other coordinate system oxyz is a local coordinate system fixed on the cylinder, where unit vectors are $\vec{i}, \vec{j}$, and $\vec{k}$ in X, Y, and Z directions respectively. In $oxyz$, x-axis is the cylinder axis, in tangent direction, y-axis is in binormal direction and z-axis is in normal direction. Its origin is located at the mass center. Both $OXYZ$ and $oxyz$ coordinate systems coincide when the cylinder is situated on the water surface horizontally at the beginning.

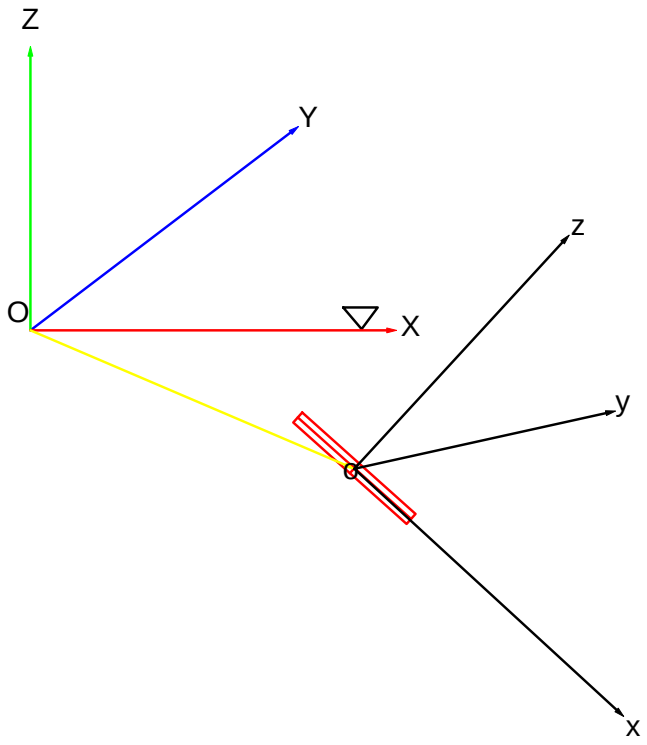

Fig. 4.1. Coordinate system for equation of motions in three dimensions

By extending Eqs. (3.1) - (3.3) based on the maneuvering theory of slender body (Newman, 1977) and rigid body dynamics (Gertler and Hagen, 1967; Feldman, 1979; Thorton and Marion, 2003) a new 3D theory for dropped cylinders has been proposed as follows:

$$(m-\rho\nabla)g\sin(\theta)+F_{dx}=m(\dot{U}_1+U_3\Omega_2-U_2\Omega_3) \tag{4.35}$$

$$\begin{aligned}-(m-\rho\nabla)g\cos(\theta)\sin(\phi)+F_{Ly}+F_{dy}=&\{m_{22}\dot{U}_2+U_1m_{t2}U_2-U_1(x_tm_{t2})\Omega_3\}\\&+m(\dot{U}_2+U_1\Omega_3-U_3\Omega_1)\end{aligned} \tag{4.36}$$

$$\begin{aligned}-(m-\rho\nabla)g\cos(\theta)\cos(\phi)+F_{Lz}+F_{dz}=&\{m_{33}\dot{U}_3+U_1m_{t3}U_3-U_1(x_tm_{t3})\Omega_2\}\\&+m(\dot{U}_3+U_2\Omega_1-U_1\Omega_2)\end{aligned} \tag{4.37}$$

$$\dot{\Omega}_1=c \tag{4.38}$$

$$M_{Ly} + M_{dy} = \{-U_1(m_{33} + x_t m_{t3})U_3 + U_1 {x_t}^2 m_{t3}\Omega_2 + m_{55}\dot{\Omega}_2\} + I_{55}\dot{\Omega}_2 + (I_{44} - I_{66})\Omega_1\Omega_3 \tag{4.39}$$

$$M_{Lz} + M_{dz} = \{-U_1(m_{22} + x_t m_{t2})U_2 + U_1 {x_t}^2 m_{t2}\Omega_3 + m_{66}\dot{\Omega}_3\} + I_{66}\dot{\Omega}_3 + (I_{55} - I_{44})\Omega_1\Omega_2 \tag{4.40}$$

2D added masses, M_{22} and M_{33} are calculated (Newman, 1977):

$$M_{22}(x) = M_{33}(x) = \pi \left(\frac{D}{2}\right)^2 \rho \quad \text{for} \quad -0.5L < x < 0.5L \tag{4.41}$$

Then, 2D added mass in sway and heave direction at the trailing edge are:

$$m_{t2}(x) = M_{22}(x = x_t) \tag{4.42}$$

$$m_{t3}(x) = M_{33}(x = x_t) \tag{4.43}$$

And 3D added masses, m_{22}, m_{33} and m_{55}, m_{66} are derived in a strip-theory way:

$$m_{22} = \int_L M_{22}(x)dx \tag{4.44}$$

$$m_{33} = \int_L M_{33}(x)dx \tag{4.45}$$

$$m_{55} = \int_L M_{33}(x)x^2 dx \tag{4.46}$$

$$m_{66} = \int_L M_{22}(x)x^2 dx \tag{4.47}$$

Translational and rotational motions in x, y, z directions can be obtained at each time step during simulations. Eqs. (4.48)-(4.50) transform the local rotational velocity components: Ω_1 ,Ω_2 and Ω_3 into global Euler angles: ϕ , θ and ψ .

$$\dot{\phi} = \Omega_1 + \frac{\Omega_2 \sin(\phi) + \Omega_3 \cos(\phi)}{\cos(\theta)} \sin(\theta) \tag{4.48}$$

$$\dot{\theta} = \Omega_2 \cos(\phi) - \Omega_2 \sin(\phi) \tag{4.49}$$

$$\dot{\psi} = \frac{\Omega_2 \sin(\phi) + \Omega_3 \cos(\phi)}{\cos(\theta)} \tag{4.50}$$

In 3D theory, the translational motion in y direction and rotation around x and z-axis are also considered. F_{dy} is the y directional drag force and M_{dz} is the z directional drag moment, both of

which are calculated from Morison equation as shown in Eqs. (4.49) and (4.50). Correspondingly, the lift forces and moments are also added: y directional lift force, F_{Ly} and moment, M_{Ly}, z directional lift force, F_{Lz} and moment, M_{Lz} are all caused by the rolling motion. *Kutta-Joukowski lift theorem* (1941) for a cylinder in ideal flow (potential theory) is used for estimating F_{Ly}, F_{Lz} and M_{Ly},M_{Lz}.

4.1.5 Hydrodynamic force and moment in potential theory

Equations for F_y and M_z are derived in the same manner as the equations for F_z and M_y:

$$F_y = -\dot{U}_2 m_{22} - \dot{\Omega}_3 m_{26} - U_1 U_2 M_{22}(x_t) + U_1 \Omega_3 x_t M_{22}(x_t) \tag{4.51}$$

$$M_z = -\dot{U}_2 m_{26} - \dot{\Omega}_3 m_{66} + U_1 U_2 [m_{22} + x_t M_{22}(x_t)] + U_1 \Omega_3 [m_{26} - x_t^2 M_{22}(x_t)] \tag{4.52}$$

For a slender body, the nose is a point of zero transverse dimensions, and thus $M_{22}(x_n) = 0$. The same will be true at the tail for a pointed body, without a tail fin, $M_{22}(x_t) = 0$; In accordance with D'Alembert's paradox, the lateral force acting on such a body in steady motion is zero. But the ends of the cylinder are not pointed, i.e. $M_{22}(x_t) \neq 0$. An additional force component is included to consider this trailing edge effect for a long slender body as shown in curly brackets on the right side of the Eqs. (3.2) - (3.3) (Newman, 1977) .

4.1.6 Viscosity

Viscous effects associated with the unsteady flow separation and vortex shedding (Cox, 1970) are ignored because of their high complexity. A quasi-steady approach is employed by using strip theory to calculate the drag force/moment on the object. The drag forces are F_{dx}, F_{dy}, and F_{dz}, in x, y and z directions respectively. Correspondingly, the drag moments, M_{dy} and M_{dz} act with respect to y and z axis:

$$F_{dx} = \begin{cases} -0.664\pi\sqrt{\nu\rho^2 L}U_1\sqrt{|U_1|} - \frac{1}{8}\rho\pi C_{dx}D^2 U_1|U_1| & \text{laminar flow} \\ -(\frac{0.455}{(\log Re)^{2.58}} - \frac{A}{Re})\frac{1}{2}\rho\pi DLU_1|U_1| - \frac{1}{8}\rho\pi C_{dx}D^2 U_1|U_1| & \text{transition} \\ -\frac{0.455}{(\log Re)^{2.58}}\frac{1}{2}\rho\pi DLU_1|U_1| - \frac{1}{8}\rho\pi C_{dx}D^2 U_1|U_1| & \text{turbulent flow} \end{cases}$$

The first term in F_{dx} represents the frictional drag which can be obtained from boundary layer theory (Schlichting, 1979) and the second term represents a form drag component (Hoerner,

1958).

$$F_{dy} = 0.5 \int_{-0.5L}^{0.5L} \rho C_{dy} D U_y(x) |U_y(x)| \mathrm{d}x \tag{4.53}$$

$$M_{dy} = -0.5 \int_{-0.5L}^{0.5L} \rho C_{dz} D x U_z(x) |U_z(x)| \mathrm{d}x \tag{4.54}$$

$$F_{dz} = 0.5 \int_{-0.5L}^{0.5L} \rho C_{dz} D U_z(x) |U_z(x)| \mathrm{d}x \tag{4.55}$$

$$M_{dz} = 0.5 \int_{-0.5L}^{0.5L} \rho C_{dy} D x U_y(x) |U_y(x)| \mathrm{d}x \tag{4.56}$$

$U_y(x)$ is the local relative velocity in y direction.The unknown parameters $U_y(x)$ and $U_z(x)$ are the local water to cylinder relative velocity in y and z direction which are represented as

$$\begin{aligned} U_y(x) &= -(U_2 + \Omega_3 x). -0.5L < x < 0.5L \\ U_z(x) &= -(U_3 - \Omega_2 x). -0.5L < x < 0.5L \end{aligned} \tag{4.57}$$

4.1.7 Lift theory

Potential flow theory predicts the velocity potential for the flow around a rotating cylinder is:

$$\Phi = U(r + \frac{R^2}{r}) \cos\theta + \frac{\Gamma}{2\pi}\theta. \tag{4.58}$$

The velocity in radial direction can be expressed as:

$$u_r = U(1 - \frac{R^2}{r^2}) \cos\theta \tag{4.59}$$

and tangential velocity:

$$u_\theta = \frac{\Gamma}{2\pi r} - U(1 + \frac{R^2}{r^2}) \sin\theta. \tag{4.60}$$

where $\Gamma = 2\pi\omega R^2$ is the circulation. ω is the rotational speed of cylinder.

To consider the pressure on the cylinder's surface, on $r = R, u_r = 0$ and $u_\theta = (\frac{\Gamma}{2\pi R} - 2U \sin\theta)$; So the pressure p at the cylinder surface can be calculated using Bernoulli's equation,

$$p + \frac{1}{2}\rho(u_\theta^2 + u_r^2) = p_\infty + \frac{1}{2}\rho U^2 \tag{4.61}$$

Then,

$$p = p_\infty + \frac{1}{2}\rho U^2 - (\frac{\rho\Gamma^2}{8\pi^2 R^2} - \frac{\rho\Gamma U}{\pi R}\sin\theta + 2\rho U^2 \sin^2\theta) \tag{4.62}$$

The pressure force per unit length

$$F = \oint -p\vec{n}\mathrm{d}l = \int_0^{2\pi} -p\vec{n}R\mathrm{d}\theta \quad \text{with} \quad \vec{n} = \cos\theta\vec{e}_x + \sin\theta\vec{e}_y \tag{4.63}$$

The force can be decomposed into its components F_x and F_y, i.e. parallel (in the x direction) and perpendicular (in the y direction) to the free stream velocity U :

$$\begin{aligned} F_x &= 0 \\ F_y &= -\rho\Gamma U \end{aligned} \tag{4.64}$$

We can get zero drag force, F_x and a nonzero lift force F_l, also called Magnus force.This is the Kutta-Joukowski theorem

$$F_l = \rho 2\pi\omega R^2 U \tag{4.65}$$

Hence, a lift coefficient is given by:

$$C_l = \frac{F_l}{\rho R U^2} = -\frac{\rho(2\pi\omega R^2)U}{\rho R U^2} = 2\pi\frac{\omega R}{U} \tag{4.66}$$

The Kutta-Joukowski lift theorem predicts a value for C_l which is generally higher than experimental results suggest. The discrepancy is primarily due to viscous effect. However, the measured C_l is in accordance with the theoretically predicted at small speed ratios, $\frac{\omega R}{U}$ (rolling frequency is very small).(Carstensen et al., 2014)

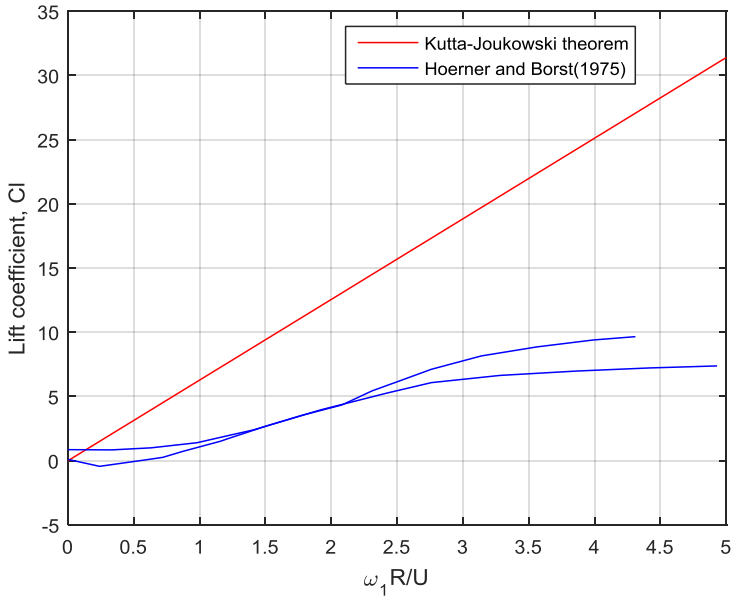

Fig. 4.2. Lift force of a rotating cylinder as a function of speed ratio

here values for C_l predicted by Kutta-Joukowski's lift theorem are only used in cases with small rolling frequencies. The following lift forces and moments are calculated:

$$F_{Ly} = \int_{-0.5L}^{0.5L} \rho U_z(x)\Gamma \mathrm{d}x = \int_{-0.5L}^{0.5L} \rho\Big[-(U_3 - \Omega_2 x)\Big]\pi D\Omega_1 \frac{D}{2}\mathrm{d}x \tag{4.67}$$

$$F_{Lz} = \int_{-0.5L}^{0.5L} \rho U_y(x)\Gamma \mathrm{d}x = \int_{-0.5L}^{0.5L} \rho\Big[-(U_2 + \Omega_3 x)\Big]\pi D\Omega_1 \frac{D}{2}\mathrm{d}x \tag{4.68}$$

$$M_{Ly} = \int_{-0.5L}^{0.5L} \rho U_y(x)\Gamma x \mathrm{d}x = \int_{-0.5L}^{0.5L} \rho\Big[-(U_2 + \Omega_3 x)\Big]\pi D\Omega_1 \frac{D}{2}x\mathrm{d}x \tag{4.69}$$

$$M_{Lz} = \int_{-0.5L}^{0.5L} \rho U_z(x)\Gamma x \mathrm{d}x = \int_{-0.5L}^{0.5L} \rho\Big[-(U_3 - \Omega_2 x)\Big]\pi D\Omega_1 \frac{D}{2}x\mathrm{d}x \tag{4.70}$$

4.1.8 Transformation of coordinate system

The governing equations here are a set of highly nonlinear ODEs. An explicit Runge Kutta 4th order method (Nagle et al., 2008) is used to integrate the system of ODEs in time. A corresponding subroutine in MATLAB is employed. Translational velocity components: U_1, U_2 and

U_3 are computed at each time step. Based on the previous step's rotation sequence of the coordinate system, the translational velocities are transformed from the local coordinate system to the global system (Beeker et al., 1993):

$$\begin{aligned}\dot{X} =& U_1 \cos(\theta)\cos(\psi) + U_2(-\cos(\phi)\sin(\psi) + \sin(\phi)\sin(\theta)\cos(\psi)) \\ &+ U_3(\sin(\phi)\sin(\psi) + \cos(\phi)\sin(\theta)\cos(\psi))\end{aligned} \tag{4.71}$$

$$\begin{aligned}\dot{Y} =& U_1 \cos(\theta)\sin(\psi) + U_2(\cos(\phi)\cos(\psi) + \sin(\phi)\sin(\theta)\sin(\psi)) \\ &+ U_3(-\sin(\phi)\cos(\psi) + \cos(\phi)\sin(\theta)\sin(\psi))\end{aligned} \tag{4.72}$$

$$\dot{Z} = -U_1 \sin(\theta) + U_2(-\sin(\phi)\cos(\theta)) + U_3(\cos(\phi)\cos(\theta)) \tag{4.73}$$

4.2 Comparison of dropped cylindrical objects using 2D theory and 3D theory

In the following we use the 3D simulation on some 2D test cases. A cylinder is dropped at an initial drop angle of 45^o. Several simulated trajectories are shown in Fig. 4.3 to illustrate the comparison between simulated results in Aanesland (1987) from 2D theory and simulated results from the new 3D theory. Good agreement between 2D theory and 3D theory is achieved for vanishing initial rolling frequency. Simulated trajectories of 2D theory and 3D theory both match the experimental results given by Aanesland (1987) best if the effective trailing edge position is set to $x_t = -0.4L$ and non-dimensional trailing edge position, $Xt = |x_t/L| = 0.4$.

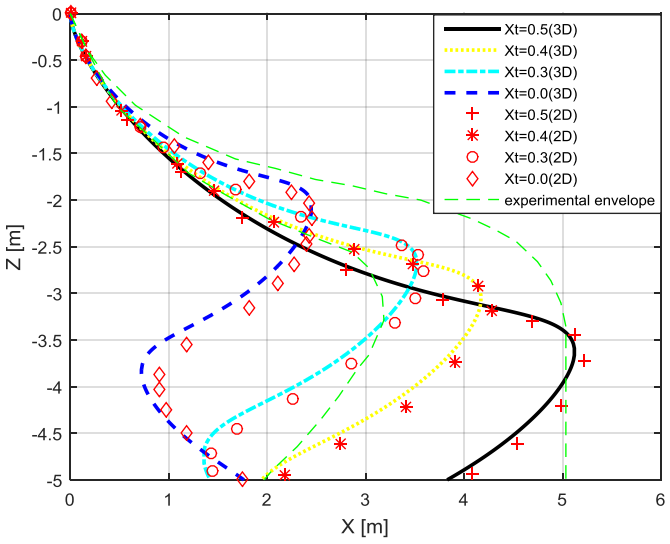

Fig. 4.3. Comparison of simulated trajectories of dropped cylinder at drop angle 45^o with variance of Xt using 2D theory in Aanesland (1987) and new 3D theory with $V_{roll} = 0$

4.3 Study of factors influencing trajectories

A drilling pipe model from Aanesland (1987) is selected as the dropped cylindrical object in this study. A list of possible factors to influence the 3D trajectory of dropped object are shown in Table 4.1.

Table 4.1: List of factors to study

Influencing Factors	Unit	Range
Drop angle (θ_0)	degree	0-90
Normal drag coefficient (C_{dz})		1.0-1.2
Binormal drag coefficient (C_{dy})		1.0-1.2
Rolling frequency (Vroll)	rad/s	0-0.1

It should be noted that initially, the cylinder is starting at in the free surface of water with zero velocity, a certain drop angle, θ_0 which is also the initial Euler angle around the Y-axis and without axial rotation. However, Aanesland (1987) found out that neglect of axial rotation will cause some errors in simulating the trajectory in real experiments. Therefore, the rolling frequency is accordingly considered to be within a small range, such as 0 to 0.1 rad/sec. The

normal and binormal drag coefficients are supposed to be in the subcritical Reynolds number range (about 1000-10000) where their values vary between 1.0 and 1.4 (Hoerner, 1958). But the numerical tests indicated that a smaller drag coefficient produced better trajectories to match experimental results, so only the range between 1.0 and 1.2 is studied. The comparison between $X - Z$ plane trajectory from 3D simulations with drop angles 30^o, 45^o and 60^o and corresponding experimental envelope is shown in Figs. 4.4-4.6.

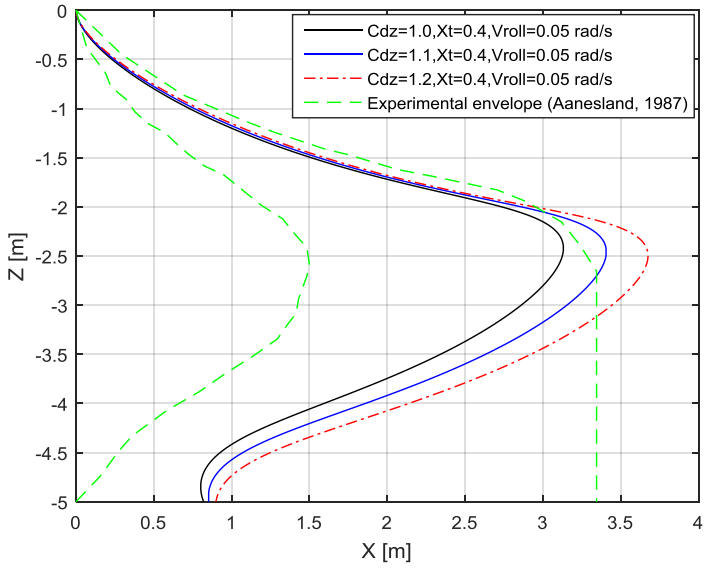

Fig. 4.4. Simulated X-Z plane trajectories with variance of C_{dz} at drop angle 30^o, Xt=0.4, Vroll=0.05rad/s, C_{dy}=1.0

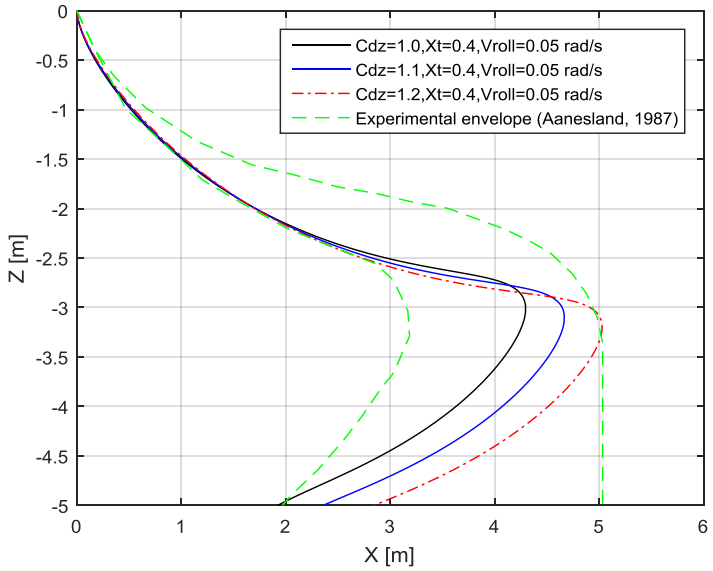

Fig. 4.5. Simulated X-Z plane trajectories with variance of C_{dz} at drop angle 45^o, Xt=0.4, Vroll=0.05rad/s, C_{dy}=1.0

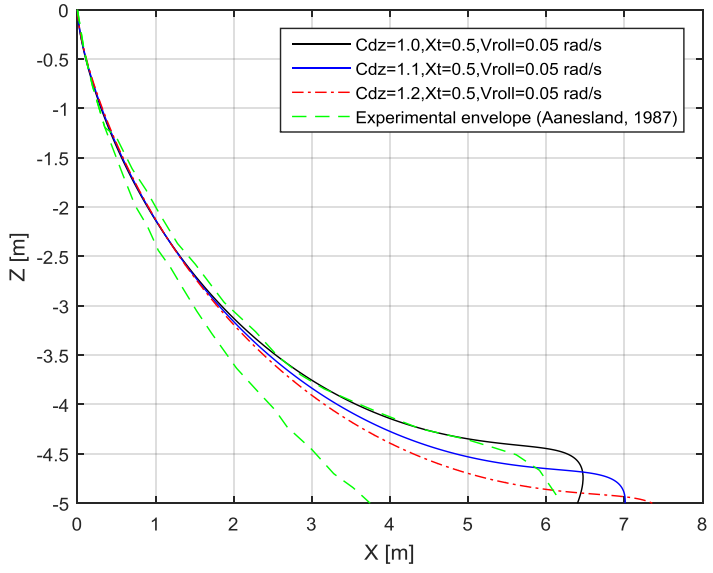

Fig. 4.6. Simulated X-Z plane trajectories with variance of C_{dz} at drop angle 60^o, Xt=0.5, Vroll=0.05rad/s, C_{dy}=1.0

Non-dimensional trailing edge position, Xt=$|x_t/L|$ =0.4 is used for cases with drop angles 30^o and 45^o. As mentioned in Aanesland (1987), for greater drop angles, a larger Xt should be used. Therefore, Xt=0.5 is used for cases with drop angles larger than 60^o. Also, an initial rolling frequency is assumed to be 0.05 rad/s. For each drop angle, the trajectories with different z directional drag coefficients, C_{dz}=1.0, 1.1 and 1.2 are simulated and presented in Figs. 4.4-4.6, respectively. All the trajectories show a similar trend. However, a larger drag coefficient, C_{dz} spreads the trajectory in positive X-direction potentially because the increased resistance force slows the movement of dropped objects in Z-axis. Figs. 4.4-4.6 also indicate that C_{dz}=1.0 can produce a more reasonable trajectory if compared with the experimental envelope (Aanesland, 1987).

The selection of different drag coefficient C_{dy} could affect the simulated trajectory in the X-Z plane. Herein, various values are used, that is 1.0, 1.1 and 1.2. The corresponding trajectories are presented in Figs. 4.7-4.9. The trajectories almost overlapped. Therefore the influence of C_{dy} on the motion in $X-Z$ plane may be ignored.

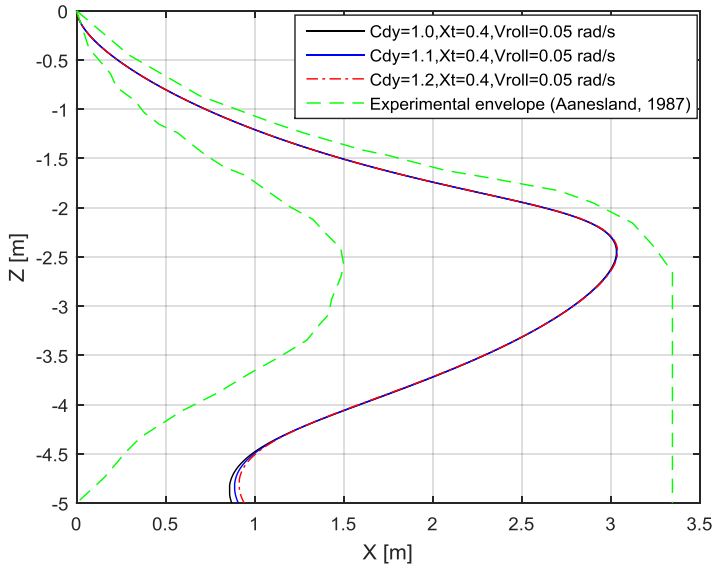

Fig. 4.7. Simulated X-Z plane trajectories with variance of C_{dy} at drop angle 30^o, Xt=0.4, Vroll=0.05rad/s, C_{dz}=1.0

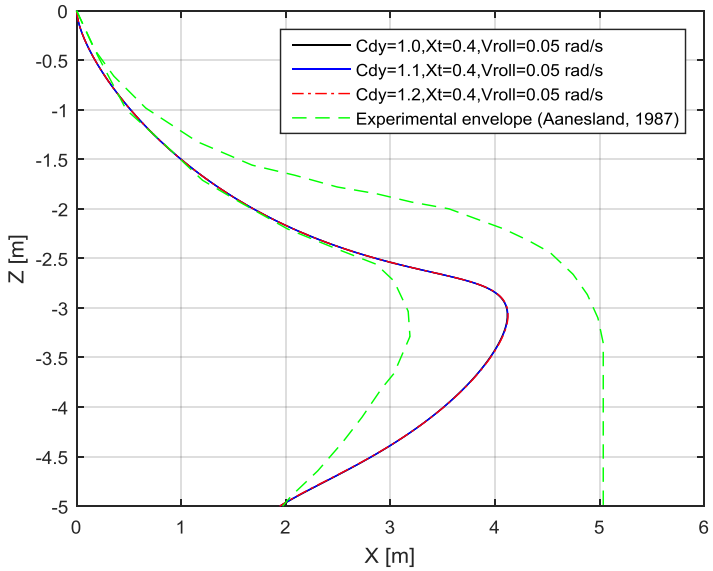

Fig. 4.8. Simulated X-Z plane trajectories with variance of C_{dy} at drop angle 45^o, Xt=0.4, Vroll=0.05rad/s, C_{dz}=1.0

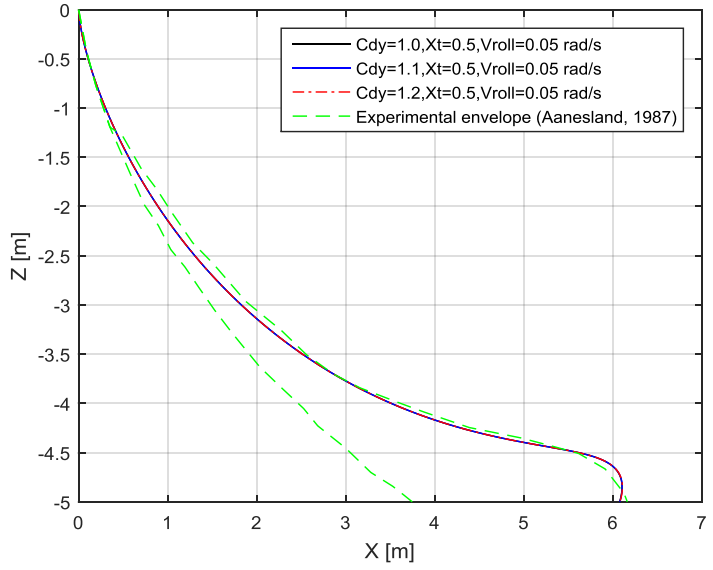

Fig. 4.9. Simulated X-Z plane trajectories with variance of C_{dy} at drop angle 60^o, Xt=0.4,Vroll=0.05rad/s, C_{dz}=1.0

The effect of drag coefficient C_{dy} on the transverse motion in the Y-Z plane is studied and presented in Figs. 4.10-4.12. When C_{dy} increases from 1.0 to 1.2, trajectory and landing point tend to be pulled towards to the origin. With a drop angle of 30^o, the difference of landing point at C_{dy}=1.0 and 1.2 reaches 0.14m which means the landing point is very sensitive to changes in C_{dy}. With increasing drop angle, the difference of landing point at C_{dy}=1.0 and 1.2 decreases to 0.10m and 0.02m respectively. See Fig. 4.11 and Fig. 4.12. So it can be concluded that the sensitivity of dropped cylinders to the change of C_{dy} decreases with increases in drop angle.

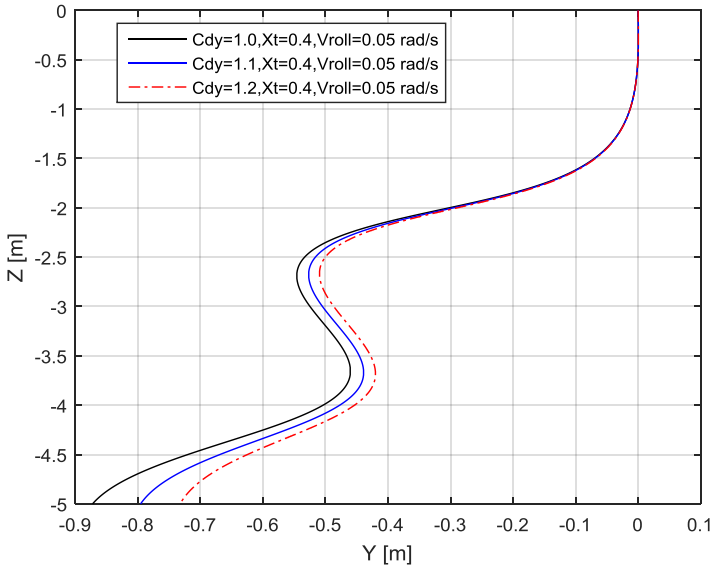

Fig. 4.10. Simulated Y-Z plane trajectories with variance of C_{dy} at drop angle 30^o, Xt=0.4, Vroll=0.05rad/s, C_{dz}=1.0

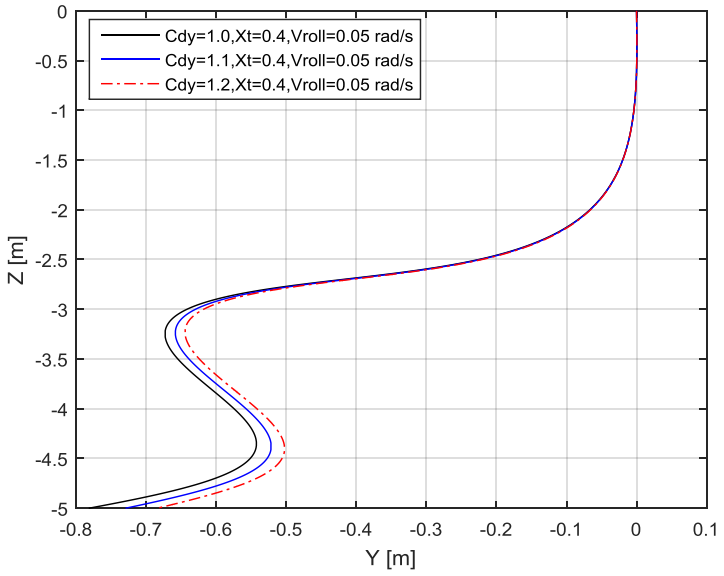

Fig. 4.11. Simulated Y-Z plane trajectories with variance of C_{dy} at drop angle 45^o, Xt=0.4, Vroll=0.05rad/s, C_{dz}=1.0

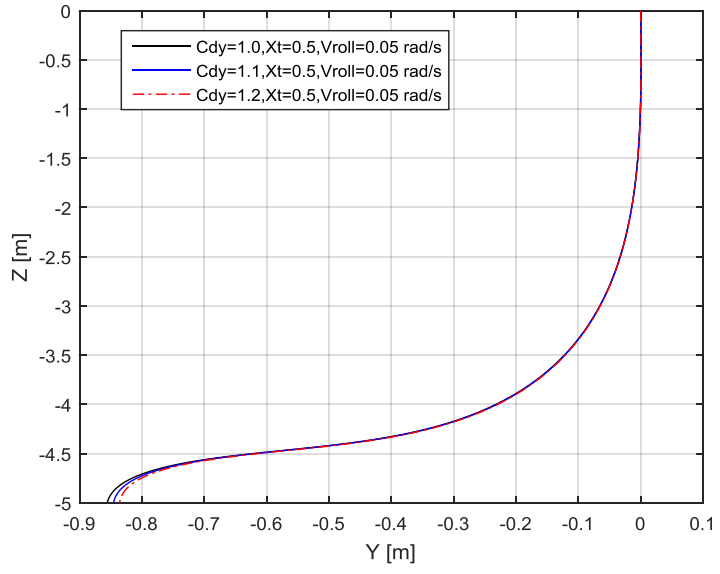

Fig. 4.12. Simulated Y-Z plane trajectories with variance of C_{dy} at drop angle 60^o, Xt=0.5, Vroll=0.05rad/s, C_{dz}=1.0

In order to consider the effect of rolling frequency, the corresponding trajectories are plotted in Figs. 4.13-4.15. All simulated trajectories are in good agreement with the experimental envelope. The trends of the simulated trajectories and landing points for a drop angle at 30^o are different when rolling frequency varies between 0 to 0.1 rad/s. For vanishing rolling frequency, 0 rad/s, the obtained trajectory follows the sketch given in Fig. 2.1(e). At a larger rolling frequency of 0.05 rad/s, the landing point moves to the left. Further increasing the rolling frequency to 0.1 rad/s, the simulated trajectory becomes close to sketch in Fig. 2.1(a). In addition, different rolling frequencies can cause some variation in the trajectory when the drop angle is less than 45^o, as indicated by Figs. 4.13 and 4.14. However, such difference seems less significant for cases with drop angles larger than 45^o, as indicated by Fig. 4.15.

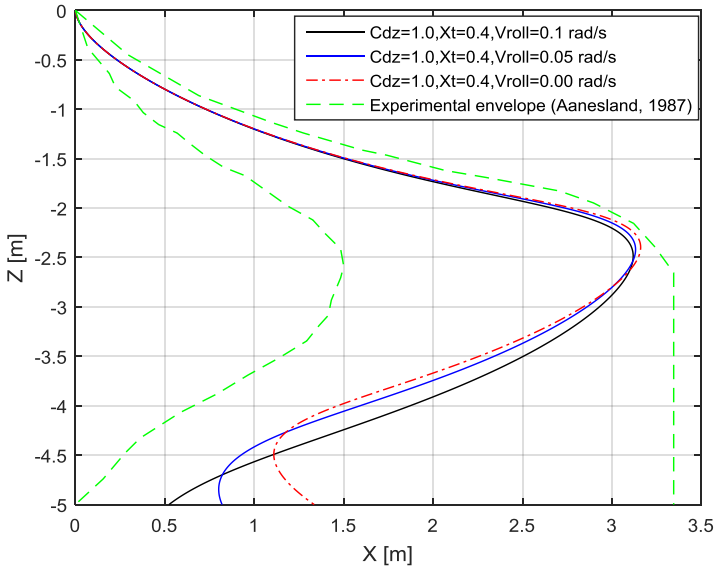

Fig. 4.13. Simulated X-Z plane trajectories with variance of V_{roll} at drop angle 30^o, Xt=0.4,C_{dy}=1.0, C_{dz}=1.0

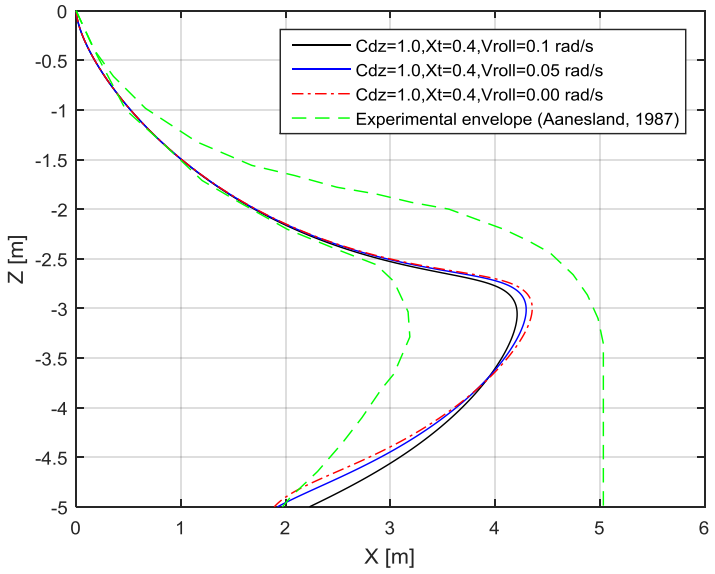

Fig. 4.14. Simulated X-Z plane trajectories with variance of V_{roll} at drop angle 45^o, Xt=0.4,C_{dy}=1.0, C_{dz}=1.0

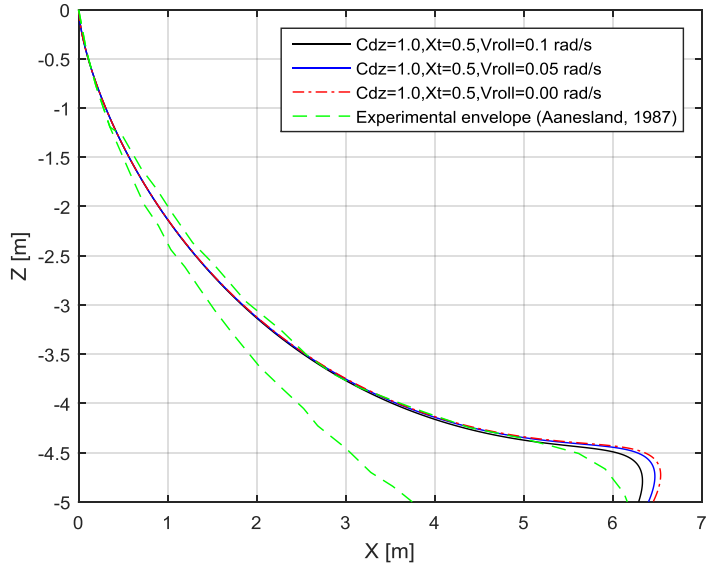

Fig. 4.15. Simulated X-Z plane trajectories with variance of V_{roll} at drop angle 60^o, Xt=0.4,C_{dy}=1.0, C_{dz}=1.0

Fig. 4.16 presents an overview of 3D trajectories with different rolling frequencies: 0 rad/s, 0.01 rad/s, 0.05 rad/s and 0.1 rad/s. A comparison of time domain translational motions in X, Y and Z direction is shown in Fig. 4.17.

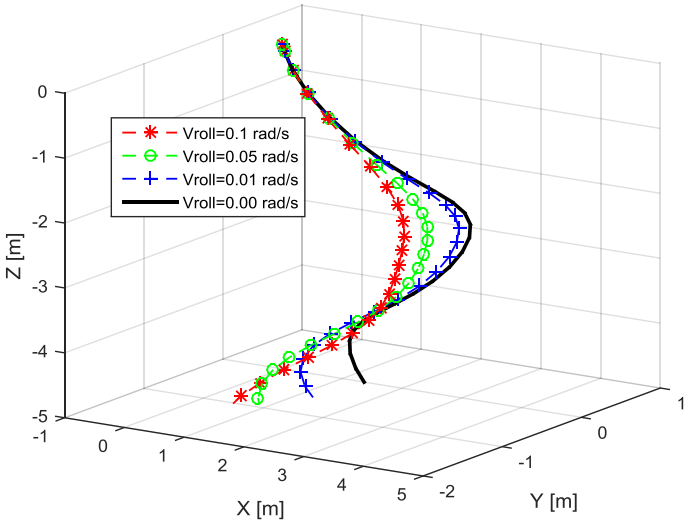

Fig. 4.16. Simulated 3D trajectories with variance of V_{roll} at drop angle 30^o, Xt=0.4, C_{dy}=1.0, C_{dz}=1.0 and V_{roll}=0.1 rad/s

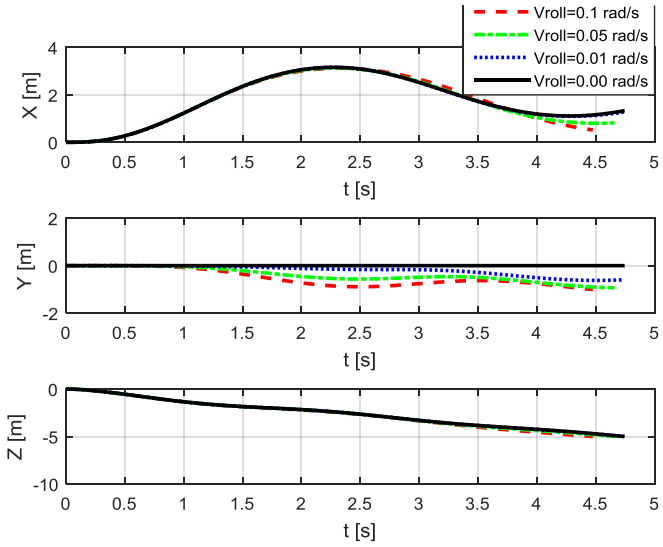

Fig. 4.17. Simulated time domain translational motions (a) in X-direction (b) in Y-direction (c) in Z-direction (from top to bottom)

It should be noted that larger rolling frequencies causes the cylinder to hit the bottom slightly sooner, as indicated by the reduced total duration time t(s) listed in Table 4.2. Further, with increasing rolling frequency but fixed drop angle 30^o, the landing point approaches the Z-axis through the origin. However, it moves further in Y direction (increasing Y). The shorter drop time associated with increased rolling frequency results in a larger terminal velocity at seabed in Z direction as indicated the Z directional component of terminal velocity, V_{tZ} in Table 4.2. More details about the terminal velocity and orientation of the dropped cylinder is recorded in Table 4.2.

Note: 1, V_{tX}, V_{tY}, V_{tZ} are the components of terminal velocity at seabed in X, Y and Z direction. ϕ_t, θ_t, ψ_t are orientation angles at seabed

2, V_{tt} is the total terminal velocity at seabed calculated as: $V_{tt} = \sqrt{V_{tX}^2 + V_{tY}^2 + V_{tZ}^2}$

Multiple simulations have been carried out to investigate the excursion distributions and landing points on the bottom. The initial drop angle is varied from 0^o to 90^o with an uniform increment of 15^o. Some parameters remain unchanged: C_{dy}=1.0, C_{dz}=1.0 and V_{roll}=0.01 rad/s. As shown in Fig. 4.18, X is increasing while the drop angle increases from 0^o to 60^o. However, for

Table 4.2: Excursion distribution for drop angle 30^o

Case number	1	2	3	4
Rolling Frequency(rad/s)	0	0.01	0.05	0.1
X(m)	1.33	1.31	0.99	0.58
Y(m)	0.00	-0. 18	-0.82	-0.99
t(s)	4.746	4.746	4.694	4.544
V_{tX}(m/s)	0.906	0.772	0.263	-0.665
V_{tY}(m/s)	0.000	0.200	-0.113	-0.482
V_{tZ}(m/s)	-1.150	-1.150	-1.091	-0.966
V_{tt}(m/s)	1.464	1.399	1.128	1.268
ϕ_t(rad)	0.000	0.110	0.279	0.448
θ_t(rad)	0.199	0.211	0.238	0.187
ψ_t(rad)	0.000	0.497	0.423	0.430

drop angles from 60^o to 90^o, X tends to decrease again. In Fig. 4.19 with drop angles increase from 0^o to 90^o, the Y directional excursion decreases from 0.5m to 0m. Maximum excursion in Y-direction occurs for a drop angle of 0^o.

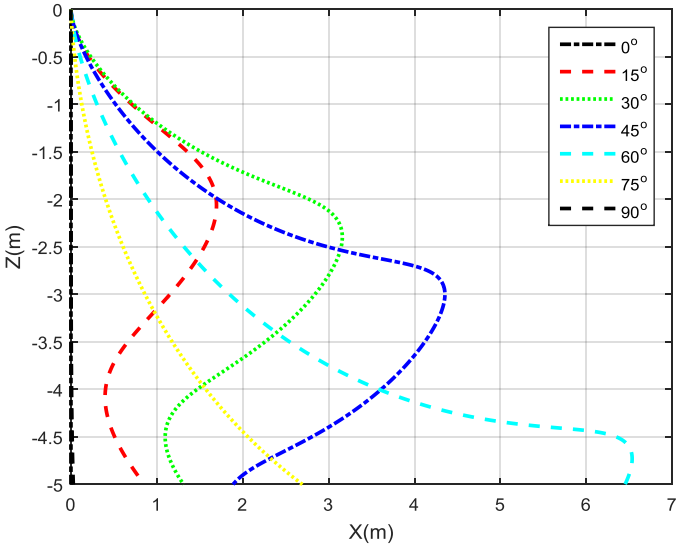

Fig. 4.18. Simulated X-Z plane trajectories with drop angle from 0^o to 90^o, C_{dy}=1.0, C_{dz}=1.0, Vroll=0.01 rad/s

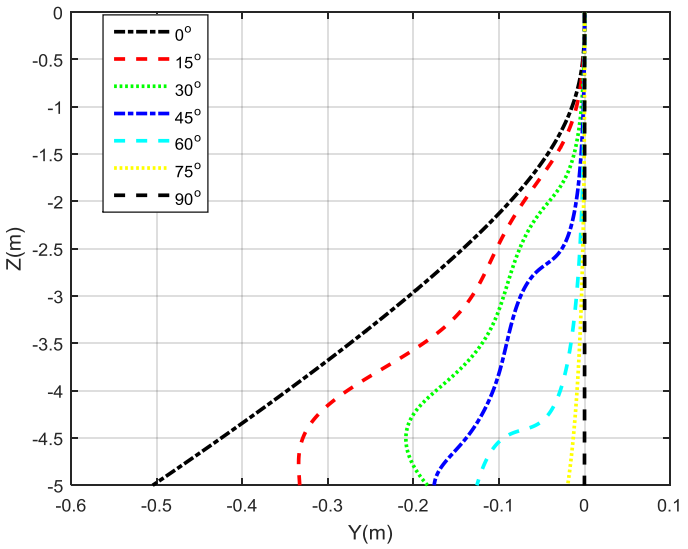

Fig. 4.19. Simulated Y-Z plane trajectories with drop angle from 0^o to 90^o, C_{dy}=1.0, C_{dz}=1.0, Vroll=0.01 rad/s

Table 4.3 provides the simulated data for X and Y directional excursions of the landing points at different drop angles and compares them with corresponding statistical experimental data. Minimum value, mean value, and maximum value are taken from Aanesland (1987). All the simulated data are close to the experimental data range . Both numerical and experimental results found that the data show the maximum X directional excursion of the landing point occurring for a drop angle 60^o.The total excursion distribution at 5 meter water depth is plotted in Fig. 4.20 and 4.21 . The excursion radius R represents the distance from the landing point to the Z-axis and is defined by:

$$R = \sqrt{X^2 + Y^2} \tag{4.74}$$

Table 4.3: Excursion distribution at drop angle 30^o

Drop angle(degree)	0	15	30	45	60	75	90
Simulated $X(m)$	0.00	0.86	1.31	1.89	6.44	2.68	0.03
Simulated $Y(m)$	-0.50	-0.33	-0.18	-0.17	-0.13	-0.02	0.00
Measured Min $X(m)$	0.00	-	0.00	1.80	4.00	-	0.00
Measured Min $Y(m)$	-	-	-	-	-	-	-
Measured Max $X(m)$	0.00	-	3.30	5.00	6.20	-	0.00
Measured Max $Y(m)$	-	-	-	-	-	-	-
Measured Mean $X(m)$	0.00	-	1.50	3.20	4.70	-	0.00
Measured Mean $Y(m)$	-	-	-	-	-	-	-

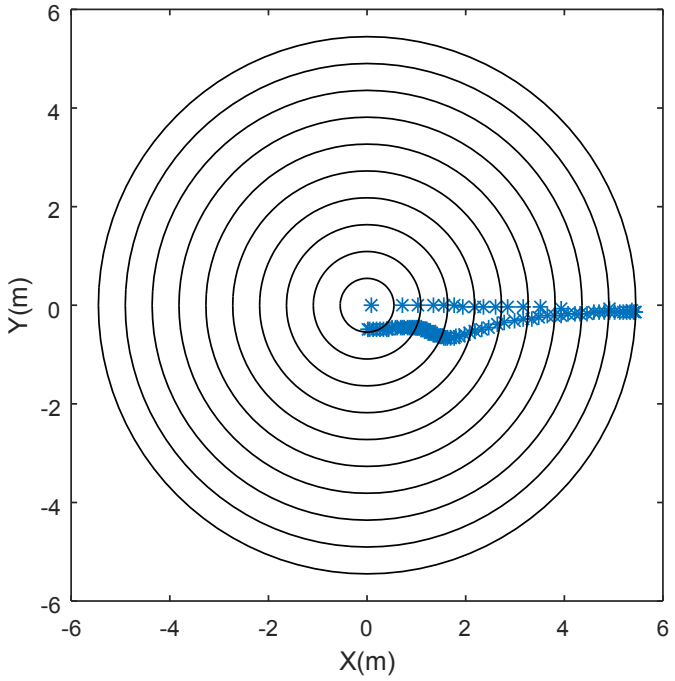

Fig. 4.20. Excursion distribution at 5m water depth with drop angles from 0^o to 90^o, $C_{dy} = 1.0, C_{dz} = 1.0, V_{roll} = 0.01$ rad/s, global view

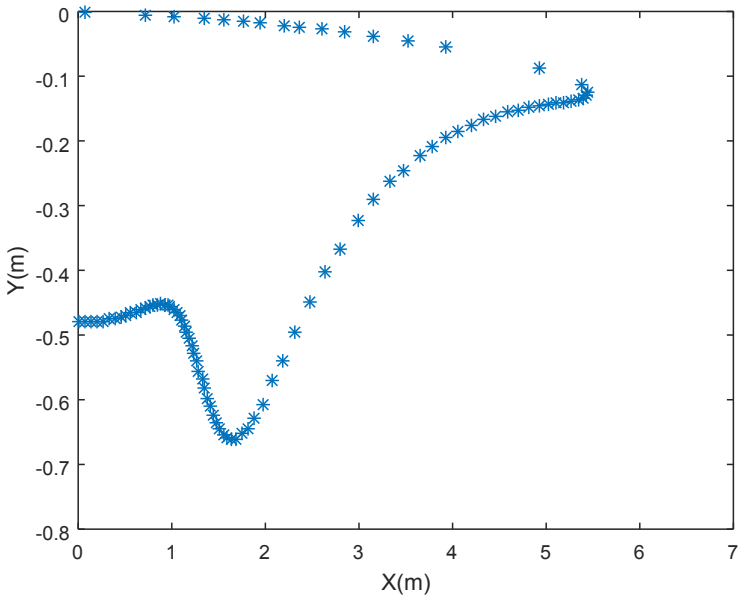

Fig. 4.21. Excursion distribution at 5m water depth with drop angles from 0^o to 90^o, $C_{dy} = 1.0, C_{dz} = 1.0, V_{roll} = 0.01$ rad/s, local view(Y axis scale enlarged)

A closer view of landing point distribution is shown in Fig. 4.21. Excursion in X-direction are more significant than in Y direction.

4.3.1 Study of translational and rotational motions

The 3D trajectory of a dropped cylinder with drop angle 30^o and rolling frequency: 0.1 rad/s and its simultaneous attitudes are simulated in Fig. 4.22. Fig. 4.23-4.25 show the translational velocity time series in X, Y, and Z direction in the time domain. Fig. 4.26-4.28 show the rotational velocity time series in X, Y, and Z direction in the time domain. Fig. 4.29-4.31 show the Euler angle time series in X, Y, and Z direction in the time domain.

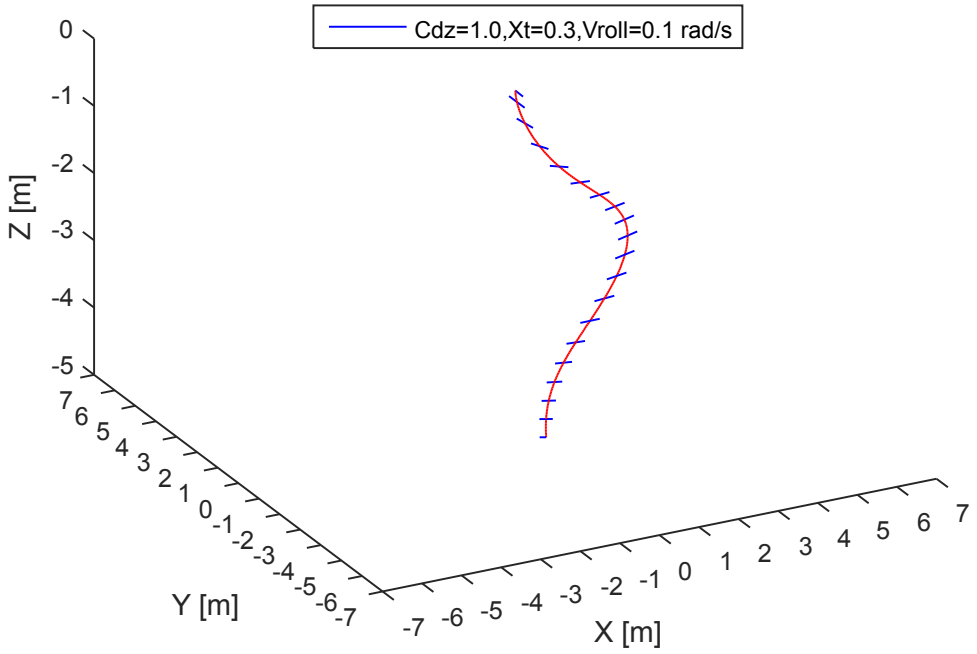

Fig. 4.22. 3D Simulated orientation and trajectory for drop angle 30^o

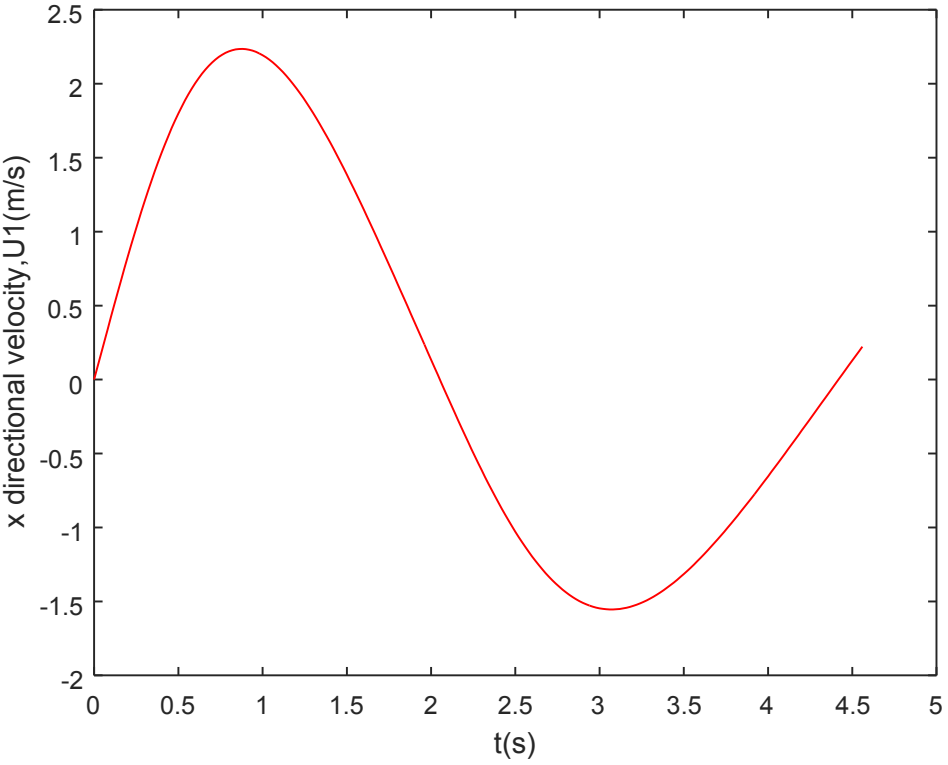

Fig. 4.23. The velocity time series of surge

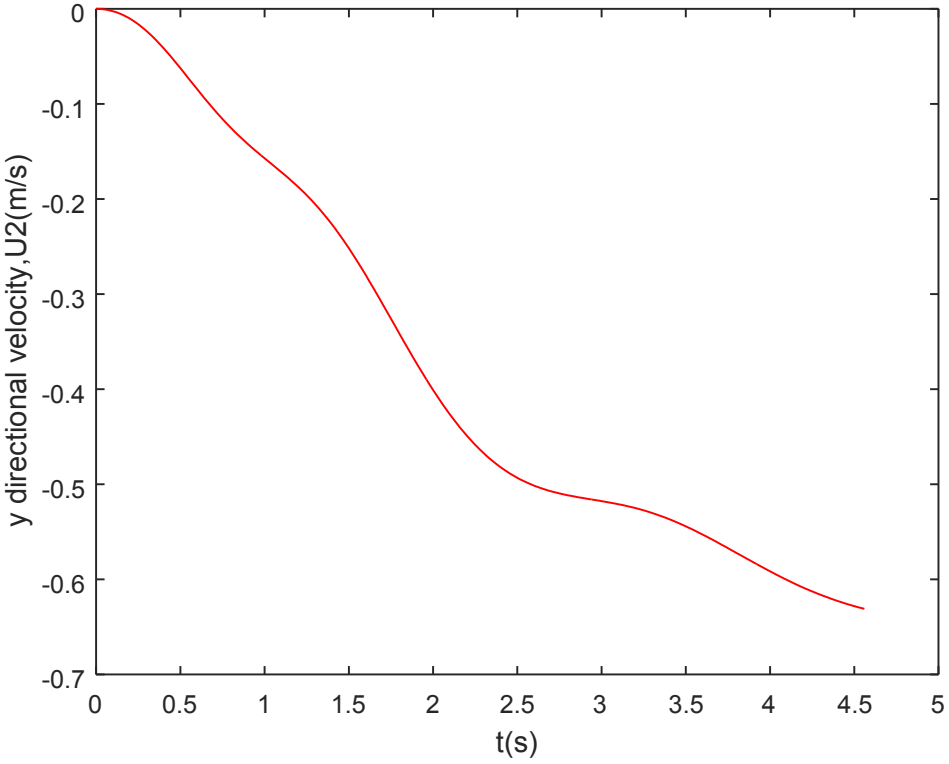

Fig. 4.24. The velocity time series of sway

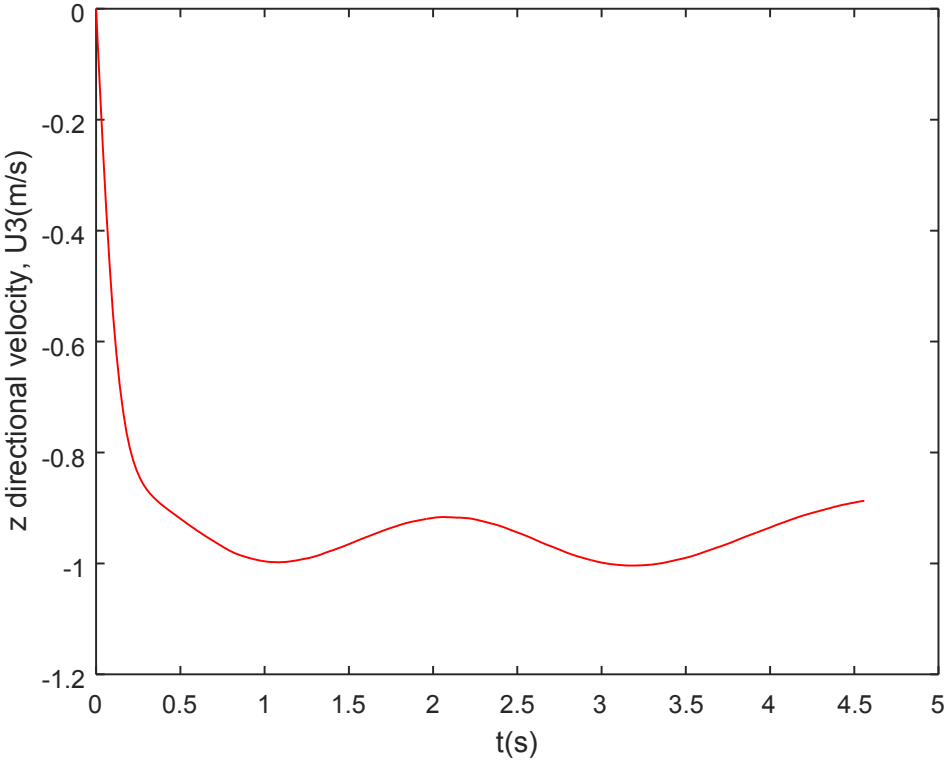

Fig. 4.25. The velocity time series of heave

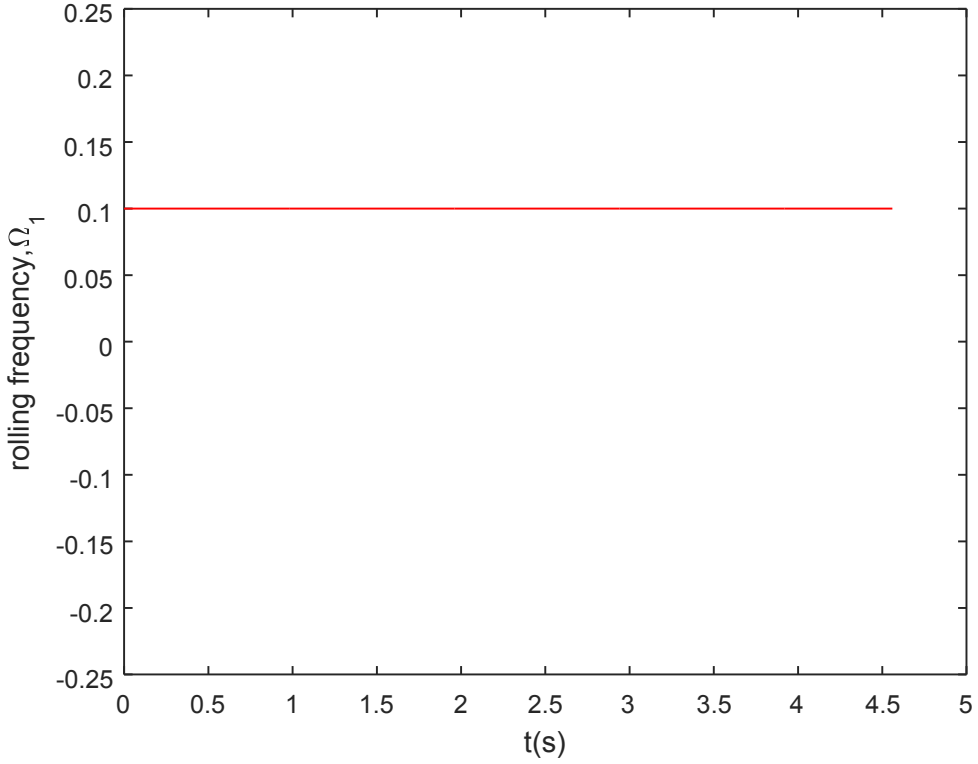

Fig. 4.26. The velocity time series of roll

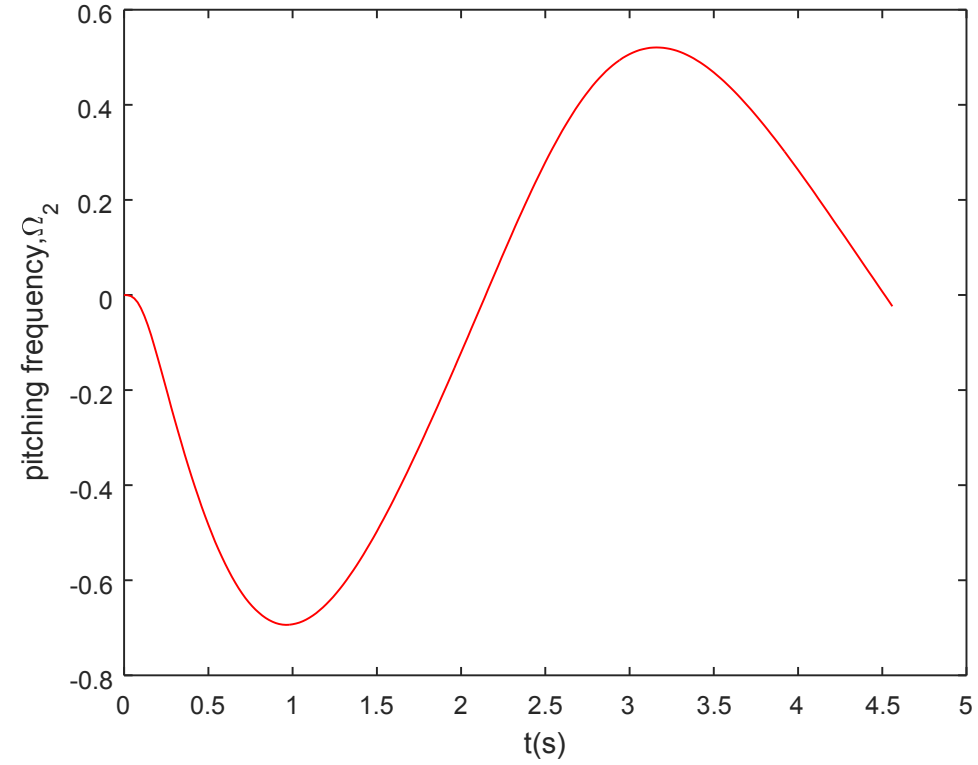

Fig. 4.27. The velocity time series of pitch

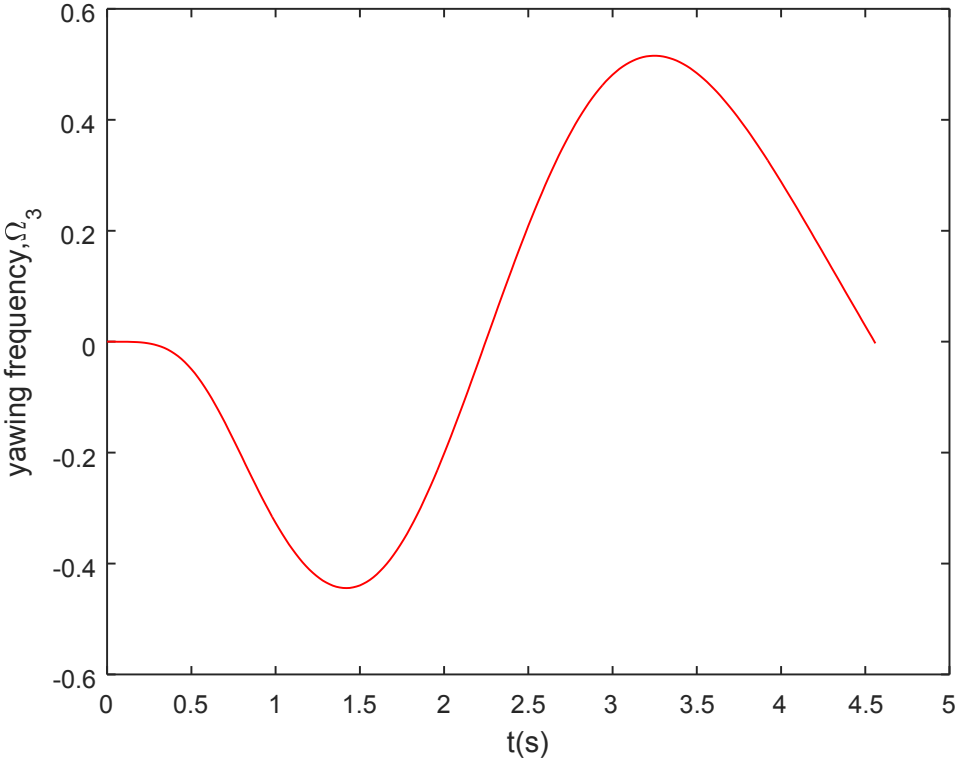

Fig. 4.28. The velocity time series of yaw

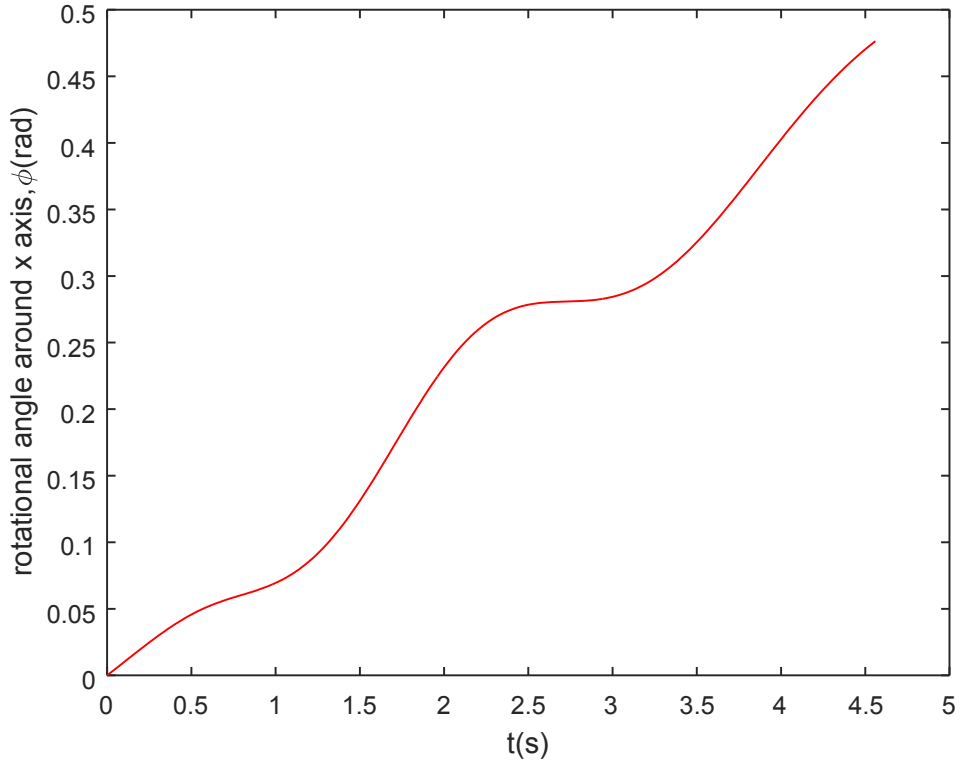

Fig. 4.29. Time series of the Euler angle in roll direction

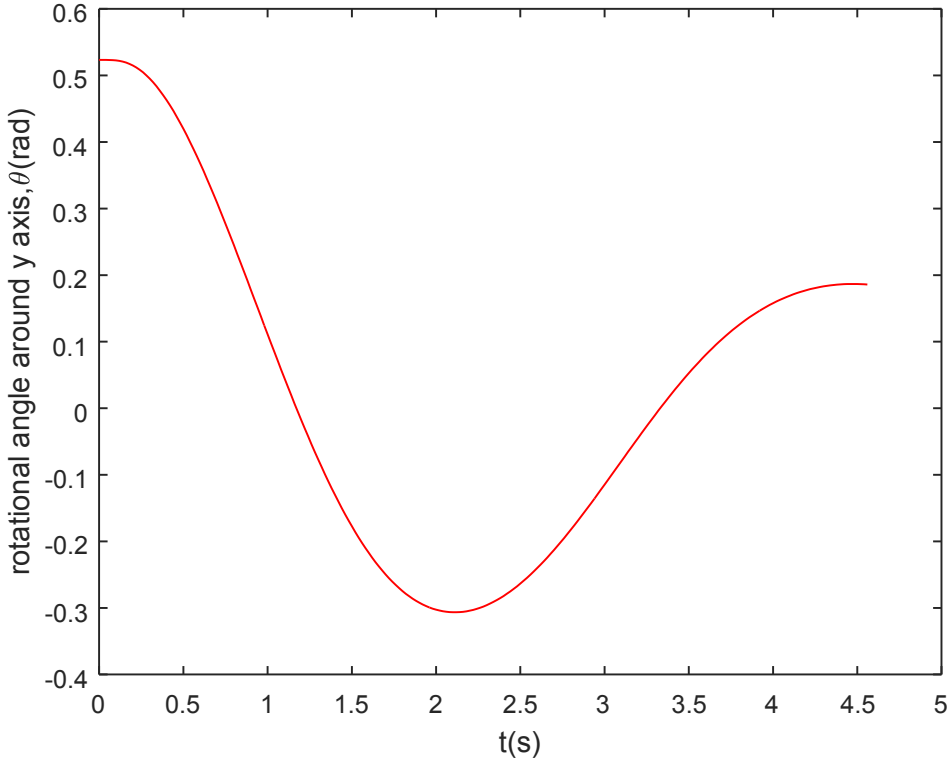

Fig. 4.30. Time series of the Euler angle in pitch direction

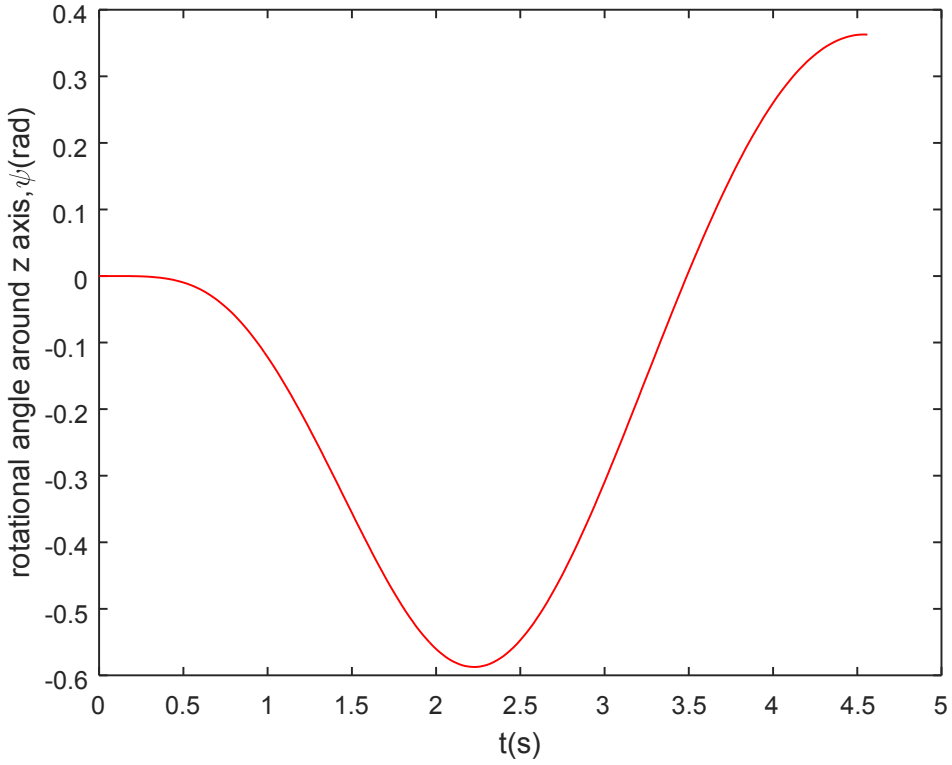

Fig. 4.31. Time series of the Euler angle in yaw direction

4.4 A more genereal three-dimensional (3D) theory for dropped objects with nonzero LCG

4.4.1 Rigid body kinematics

In case where the longitudinal center of gravity (LCG) does not coincide with the origin, the acceleration of the body at the mass center, G, in terms of the body fixed system can be expressed by

$$\vec{V}_G = \vec{V}_o + \vec{\Omega}_o \times \vec{R}_G \tag{4.75}$$

$$\vec{a}_G = \vec{a}_o + \dot{\vec{\Omega}}_o \times \vec{R}_G + \vec{\Omega}_o \times (\vec{\Omega}_o \times \vec{R}_G) \tag{4.76}$$

Substituting Eq. (4.10) into Eq. (4.76) yields,

$$\begin{aligned} \vec{a}_G = {} & (\dot{u} - vr + wq - x_G(q^2 + r^2) + y_G(pq - \dot{r}) + z_G(pr + \dot{q}))\vec{i} \\ & + (\dot{v} + ur - wp + x_G(pq + \dot{r}) - y_G(p^2 + r^2) + z_G(qr - \dot{p}))\vec{j} \\ & + (\dot{w} - uq + vp + x_G(pr - \dot{q}) + y_G(qr + \dot{p}) - z_G(p^2 + q^2))\vec{k} \end{aligned} \tag{4.77}$$

4.4.2 Rigid body dynamics

A rigid body consists of a set of material points with masses m_i located at the vector positions $\vec{R}_i = x_i\vec{i} + y_i\vec{j} + z_i\vec{k}$. The total mass of the body is $m = \Sigma_i m_i$. The position of the center of mass is determined by $\vec{R}_G = \frac{1}{m}\Sigma_i m_i \vec{R}_i$. The time rate of the linear momentum for the rigid body may be expressed as:

$$\begin{aligned} & \frac{\mathrm{d}}{\mathrm{d}t}\Big[\Sigma m_i(\vec{V}_o + \vec{\Omega}_o \times \vec{R}_i)\Big] \\ & = (\Sigma m_i)\frac{\mathrm{d}\vec{V}_o}{\mathrm{d}t} + \frac{\mathrm{d}}{\mathrm{d}t}\Big[\vec{\Omega}_o \times (\Sigma m_i \vec{R}_i)\Big] \\ & = (\Sigma m_i)\frac{\mathrm{d}\vec{V}_o}{\mathrm{d}t} + \dot{\vec{\Omega}}_o \times (\Sigma m_i \vec{R}_i) + \vec{\Omega}_o \times \Big[\vec{\Omega}_o \times (\Sigma m_i \vec{R}_i)\Big] \\ & = m\Big[\vec{a}_o + \dot{\vec{\Omega}}_o \times \vec{R}_G + \vec{\Omega}_o \times (\vec{\Omega}_o \times \vec{R}_G)\Big] \\ & = m\vec{a}_G \end{aligned} \tag{4.78}$$

Based on Newton's Second Law:

$$F_e = \frac{\mathrm{d}}{\mathrm{d}t}\Big[\Sigma m_i(\vec{V}_o + \vec{\Omega}_o \times \vec{R}_i)\Big] = m\vec{a}_G \tag{4.79}$$

F_e is the total external force acting on the mass center, G. It can be split into its components.

$$F_e = F_{ex}\vec{i} + F_{ey}\vec{j} + F_{ez}\vec{k} \tag{4.80}$$

When we substitute Eq. (4.80) into Eq. (4.79), we obtain

$$\begin{aligned} F_{ex}\vec{i} + F_{ey}\vec{j} + F_{ez}\vec{k} =& m\Big[(\dot{u} - vr + wq - x_G(q^2 + r^2) + y_G(pq - \dot{r}) + z_G(pr + \dot{q}))\vec{i} \\ &+ (\dot{v} + ur - wp + x_G(pq + \dot{r}) - y_G(p^2 + r^2) + z_G(qr - \dot{p}))\vec{j} \\ &+ (\dot{w} - uq + vp + x_G(pr - \dot{q}) + y_G(qr + \dot{p}) - z_G(p^2 + q^2))\vec{k}\Big] \end{aligned} \tag{4.81}$$

Based on Newton's Second Law, the rate of change of angular momentum is:

$$\begin{aligned} M_e &= \frac{\mathrm{d}}{\mathrm{d}t}\Big[\Sigma\vec{R}_i \times m_i(\vec{V}_o + \vec{\Omega}_o \times \vec{R}_i)\Big] \\ &= m\vec{R}_G \times \vec{a}_o + \dot{\vec{\Omega}}_o(\Sigma\, m_i\vec{R}_i \cdot \vec{R}_i) - (\Sigma\, m_i\vec{R}_i\vec{R}_i) \cdot \dot{\vec{\Omega}}_o + \dot{\vec{\Omega}}_o \cdot (\Sigma\, m_i\vec{R}_i\vec{R}_i) \times \vec{\Omega}_o \end{aligned} \tag{4.82}$$

M_e is the total moment of external forces with respect to the body fixed system. The total moment can be expressed by its components.

$$M_e = M_{ex}\vec{i} + M_{ey}\vec{j} + M_{ez}\vec{k} \tag{4.83}$$

Substitution of Eq. (4.83) into Eq. (4.82) yields,

$$\begin{aligned} M_{ex}\vec{i} + M_{ey}\vec{j} + M_{ez}\vec{k} =& m\{[y_G(\dot{w} - uq + vp) - z_G(\dot{v} + ur - wp) + I_x\dot{p} - I_{xy}(\dot{q} - pr) \\ &- I_{xz}(\dot{r} + pq) + I_{yz}(r^2 - q^2) + (I_z - I_y)qr]\vec{i} + [z_G(\dot{u} - vr + wq) \\ &- x_G(\dot{w} - uq + vp) + I_y\dot{q} - I_{yx}(\dot{p} + qr) - I_{yz}(\dot{r} - pq) + I_{xz}(p^2 - r^2) \\ &+ (I_x - I_z)pr]\vec{j} + [x_G(\dot{v} + ur - wp) - y_G(\dot{u} - vr + wq) + I_z\dot{r} \\ &- I_{zx}(\dot{p} - qr) - I_{zy}(\dot{q} + pr) + I_{xy}(q^2 - p^2) + (I_y - I_x)pq]\vec{k}\} \end{aligned} \tag{4.84}$$

4.4.3 Equations of motion for dropped objects with nonzero LCG

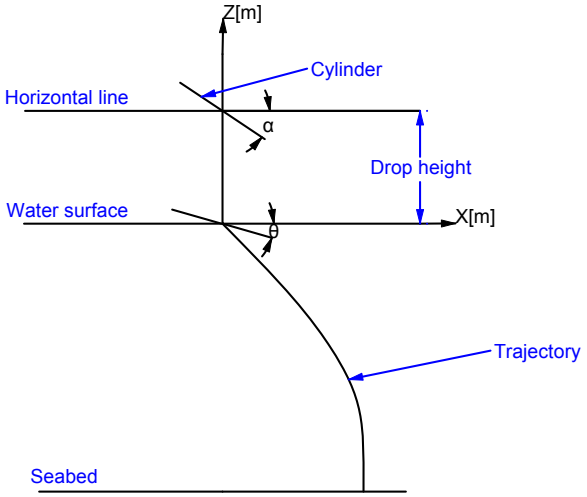

Fig. 4.32. Set up of the cylinders dropped into water

The 3D theory in Xiang et al. (2016) based on the maneuvering theory of slender body (Newman, 1977) and rigid body dynamics (Gertler, 1967; Feldman, 1979; Thorton et al. 2003)), is extended for dropped cylinders with non-zero LCG:

$$(m-\rho\nabla)g\sin(\theta)+F_{dx}=m(\dot{U}_1+U_3\Omega_2-U_2\Omega_3-X_G\Omega_2^2-X_G\Omega_3^2) \tag{4.85}$$

$$\begin{aligned}-(m-\rho\nabla)g\cos(\theta)\sin(\phi)+F_{Ly}+F_{dy}=&\{m_{22}\dot{U}_2+U_1m_{t2}U_2-U_1(x_tm_{t2})\Omega_3\}\\&+m(\dot{U}_2+U_1\Omega_3-U_3\Omega_1+X_G\Omega_1\Omega_2+X_G\dot{\Omega}_3)\end{aligned} \tag{4.86}$$

$$\begin{aligned}-(m-\rho\nabla)g\cos(\theta)\cos(\phi)+F_{Lz}+F_{dz}=&\{m_{33}\dot{U}_3+U_1m_{t3}U_3-U_1(x_tm_{t3})\Omega_2\}\\&+m(\dot{U}_3+U_2\Omega_1-U_1\Omega_2+X_G\Omega_1\Omega_3-X_G\dot{\Omega}_2)\end{aligned} \tag{4.87}$$

$$\dot{\Omega}_1=c \tag{4.88}$$

$$M_{Gy} + M_{Ly} + M_{dy} = \{-U_1(m_{33} + x_t m_{t3})U_3 + U_1 {x_t}^2 m_{t3}\Omega_2 + m_{55}\dot{\Omega}_2\} + M_{55}\dot{\Omega}_2 + (M_{44} - M_{66})\Omega_1\Omega_3 - mX_G(\dot{U}_3 - U_1\Omega_2 + U_2\Omega_1) \tag{4.89}$$

$$M_{Gz} + M_{Lz} + M_{dz} = \{-U_1(m_{22} + x_t m_{t2})U_2 + U_1 {x_t}^2 m_{t2}\Omega_3 + m_{66}\dot{\Omega}_3\} + M_{66}\dot{\Omega}_3 + (M_{55} - M_{44})\Omega_1\Omega_2 + mX_G(\dot{U}_2 + U_1\Omega_3 - U_3\Omega_1) \tag{4.90}$$

M_{Gy} and M_{Gz} are the moments caused by off-center weight in y and z direction:

$$M_{Gy} = X_G mg\cos(\theta)\cos(\phi) \tag{4.91}$$

$$M_{Gz} = -X_G mg\cos(\theta)\sin(\phi) \tag{4.92}$$

C_{dy} and C_{dz} are drag coefficients in y-direction and z-direction calculated based on empirical formula (Rouse, 1938):

$$C_{dy} \text{ or } C_{dz} = \begin{cases} 1.9276 + \frac{8}{Re} & Re \leq 12 \\ 1.261 + \frac{16}{Re} & 12 < Re \leq 180 \\ 0.855 + \frac{89}{Re} & 180 < Re \leq 2000 \\ 0.84 + 0.00003Re & 2000 < Re \leq 12000 \\ 1.2 - \frac{4}{\delta} & 12000 < Re \leq 15000, \delta \leq 10 \\ 0.835 - \frac{0.35}{\delta} & 12000 < Re \leq 15000, 2 \leq \delta < 10 \\ 0.7 - \frac{0.08}{\delta} & 12000 < Re \leq 15000, \delta < 2 \\ 1.875 - 0.0000045Re & 150000 < Re \leq 350000 \\ \frac{1}{\frac{641550}{Re} + 1.5} & Re > 350000 \end{cases}$$

δ=L/D is the cylinder's aspect ratio. Re is the Reynolds number. Re is position dependent and formed with the local transverse relative velocities corresponding to the direction of the drag coefficients: $Re = \frac{U_y(x)D}{\nu}$ for C_{dy}; $Re = \frac{U_z(x)D}{\nu}$ for C_{dz} . $U_y(x)$ and $U_z(x)$ are the local transverse relative velocities in y and z direction respectively.

Three cylinders at model scale are chosen as simulated objects in this study. The properties of these three cylinders: Cylinder #1 (Aanesland, 1987), Cylinder #2 (Chu, 2005), and Cylinder #3 (Chu, 2005) are described in Tables 4.4-4.6. Cylinder #1 starts at the free surface with zero velocity and a defined orientation angle . Cylinders #2 and #3 are start at a defined drop angle

and drop height above the water surface. Once released, the cylinders drop into the water and sink until they hit the seabed. A setup with the cylinders is shown in Fig. 4.32 where α is the drop angle, θ is the instantaneous orientation angle (Euler angle) around the Y-axis. DROBS starts its simulations once a cylinder has fully entered the water. θ_0 is the initial orientation angle around Y-axis.

Table 4.4: Properties of the Cylinder #1

Parameters	Unit	Model Scale (1:20.32)
Length	m	0.450
Mass density	kg/m	0.548
Diameter	m	0.01
LCG	m	0.00

Table 4.5: Properties of the Cylinder #2

Parameters	Unit	Model Scale (1:15)
Length	m	0.152
Mass density	kg/m	2.12
Diameter	m	0.04
LCG	m	0.0074

Table 4.6: Properties of the Cylinder #3

Parameters	Unit	Model Scale (1:15)
Length	m	0.121
Mass density	kg/m	2.10
Diameter	m	0.04
LCG	m	-0.01

Initially, Cylinder #1 has an uniform mass distribution with LCG= 0.00m. The initial conditions for the underwater motions are defined as follows:

$$\begin{aligned} &X_0 = 0, Y_0 = 0, Z_0 = 0, \dot{X}_0 = 0, \dot{Y}_0 = 0, \dot{Z}_0 = 0, \phi_0 = 0 \\ &\theta_0 = 30^o, 45^o, 60^o, \psi_0 = 0, \Omega_{10} = 0, \Omega_{20} = 0, \Omega_{30} = 0 \end{aligned} \tag{4.93}$$

The effective trailing edge position is set to X_t= -0.3L and non-dimensional trailing edge position, Xt= $|X_t|$ =0.3. Th is is commonly employed in maneuvering studies of ships with a blunt aftbody (Aanesland, 1987). It also represents a lower limit value for Xt . Simulations have been performed using the values Xt=0.3, 0.4, and 0.5. Figs. 3 and 4 show the respective trajectories for initial orientation angles of θ_0= 30^o and θ_0= 45^o, respectively. For both initial angles, trailing edge positions of Xt=0.3 and Xt=0.4 predict trajectories which are more in line

with the experimental envelope. Trajectories with Xt=0.5 overshoot the right side bound of the observed experimental envelope.

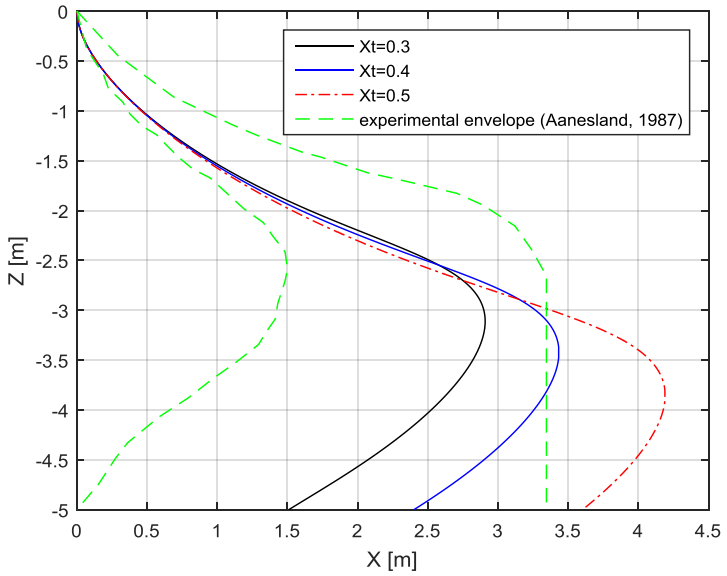

Fig. 4.33. Simulated trajectory with variance of Xt at θ_0= 30^o

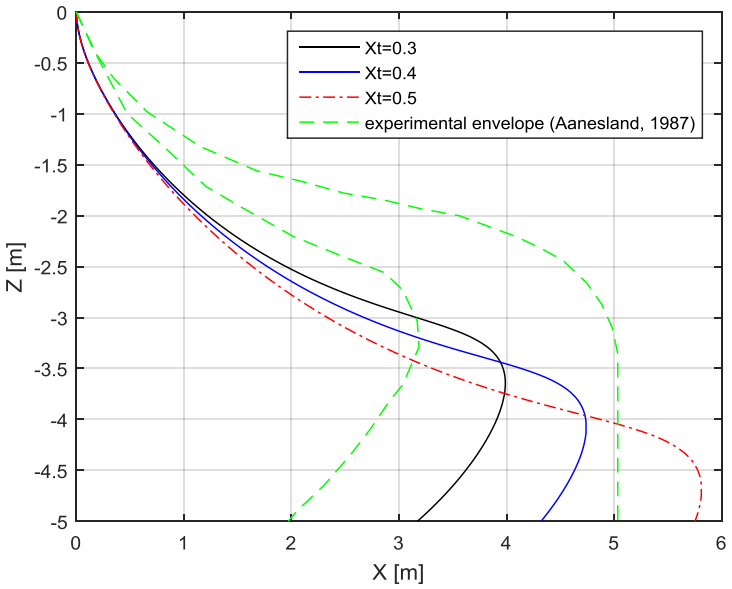

Fig. 4.34. Simulated trajectory with variance of Xt at θ_0= 45^o

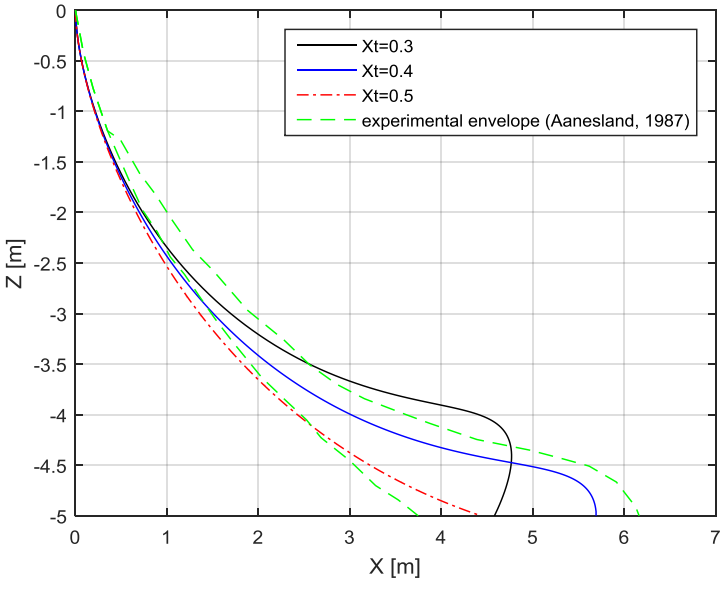

Fig. 4.35. Simulated trajectory with variance of Xt at θ_0= 60^o

The effect of the trailing edge parameter is diminished at higher initial orientation angles θ_0 . Fig. 5 shows trajectories for θ_0 = 60^o. Trajectories predicted for Xt=0.5 and Xt=0.4 match the trends of left and right side bounds of the experimental envelope better than with Xt=0.3. In Figs. 3-5, with θ_0 increasing from 30^o to 60^o, the simulated landing points seem to shift to higher X-values, whereas the spread is slightly decreasing. Table 4.7 summarizes experimental and numerical results. The simulations show that the trailing edge position Xt has significant influence on the simulated trajectory. They also confirm that the initial orientation angle θ_0 is one of the main factors determining the trajectory of dropped cylinders which is consistent with the findings from Aanesland (1987), Luo and Davis (1992), and Colwill and Ahilan, (1992).

Table 4.7: X coordinates of landing points for Cylinder#1

X coordinates of landing points (m)	DROBS	Experiments (Aanesland,1987)
30^o with Xt=0.3 and Xt=0.4	1.5, 2.4	0.0-3.4
45^o with Xt=0.3 and Xt=0.4	3.1, 4.2	1.9-5.0
60^o with Xt=0.4 and Xt=0.5	4.2, 5.8	3.8-6.1

Cylinder #2 has a nose down configuration with positive LCG=0.0074m. For the experiments in Chu et al. (2005), the initial conditions for the underwater motions are recorded as follows:

$$\begin{aligned} &X_0 = 0, Y_0 = 0, Z_0 = 0, \dot{X}_0 = 0, \dot{Y}_0 = -1.55m/s, \dot{Z}_0 = -2.52m/s, \phi_0 = 0 \\ &\theta_0 = 60^o, \psi_0 = -95^o, \Omega_{10} = 0rad/s, \Omega_{20} = 0.49rad/s, \Omega_{30} = 0.29rad/s \end{aligned} \tag{4.94}$$

The simulated underwater trajectory of the center of gravity of a cylinder is compared to experimental and simulated results from Chu et al. (2005) as shown in Fig. 4.36. The trajectory predicted from DROBS in Fig. 4.37 matches the observed trajectories from experimental tests. In contrast to the simulation by Chu et al. (2005), the projection of trajectories onto the sea bed predicted by DROBS can show the motion in X-direction before hitting the sea bed and agrees well with the projection of the trajectory observed in experiments. The landing point predicted by DROBS (X=-0.02, Y=-0.42) matches the experimental landing point (X=-0.1, Y=-0.25 Chu et al. 2005) better than the simulation result reported in Chu (2005) (X=0.05, Y=-0.5). Landing point data for Cylinder #2 is summarized in Table 4.8.

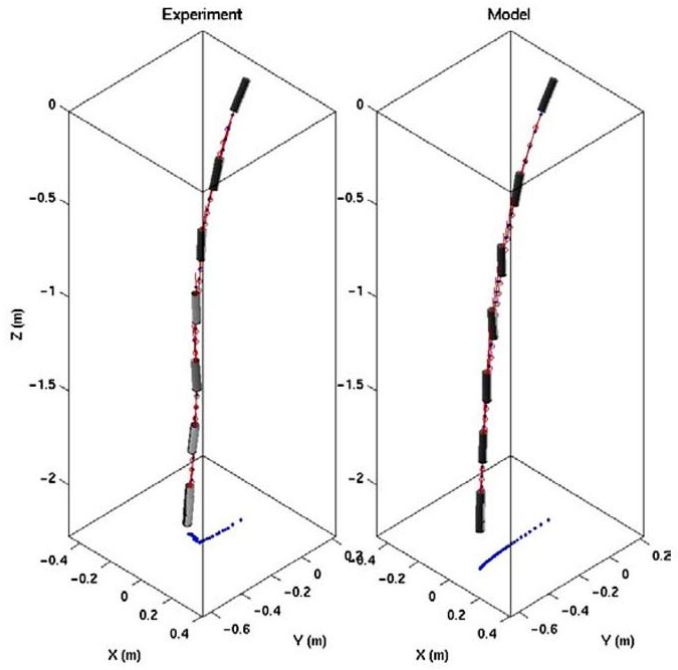

Fig. 4.36. Trajectory of cylinder #2 with drop angle 45^o: (a) Chu et al. (2005)

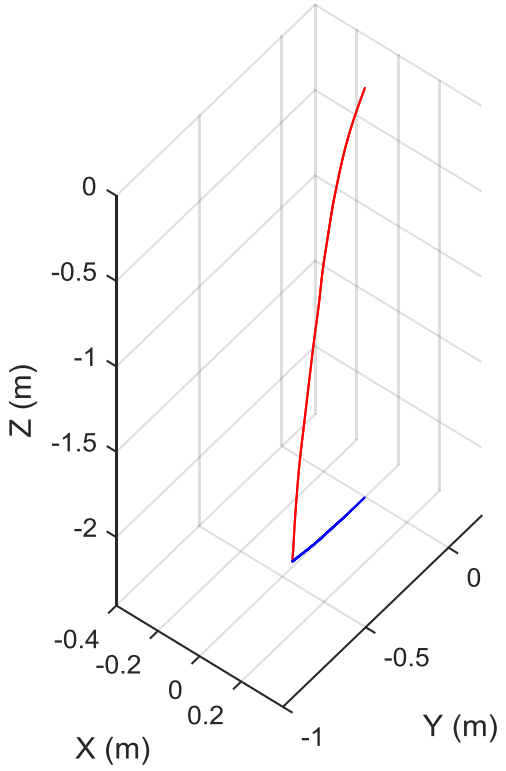

Fig. 4.37. Trajectory of cylinder #2 with drop angle 45^o: (b) DROBS

Table 4.8: Comparison of landing points for Cylinder #2

Landing points	Experimental results - Chu et al. (2005)	Simulated results - Chu et al. (2005)	Simulated results-DROBS
X (m)	-0.10	0.05	-0.02
Y (m)	-0.25	-0.50	-0.42

Cylinder #3 has a nose up configuration with positive LCG= -0.01m. Chu et al. (2005) reports the following initial conditions for the underwater motions measured in experiments:

$$\begin{aligned} &X_0 = 0, Y_0 = 0, Z_0 = 0, \dot{X}_0 = 0, \dot{Y}_0 = -0.75m/s, \dot{Z}_0 = -0.67m/s, \phi_0 = 0 \\ &\theta_0 = 24^o, \psi_0 = -96^o, \Omega_{10} = 0rad/s, \Omega_{20} = 5.08rad/s, \Omega_{30} = 0.15rad/s \end{aligned} \tag{4.95}$$

Fig. 4.38 and Fig. 4.39 show the simulated underwater trajectories of the center of gravity of cylinder #3. Experimental and simulated results from Chu et al. (2005) are depicted in Fig. 4.38. Fig. 4.39 presents the trajectory predicted by DROBS. The landing point estimated by DROBS is closer to the experimental value. Table 4.9 compares landing point data from Chu (2005), Chu et al. (2005), and the current work.

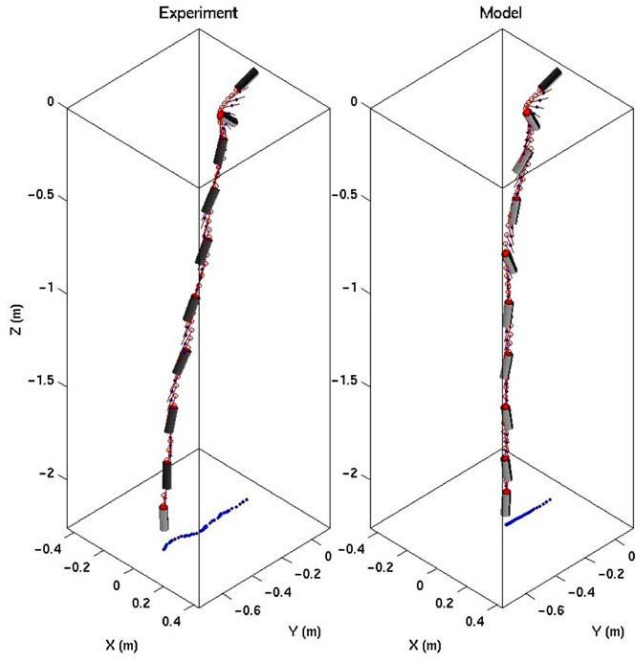

Fig. 4.38. Trajectory of cylinder #3 with drop angle 45^o: (a) Chu et al. (2005)

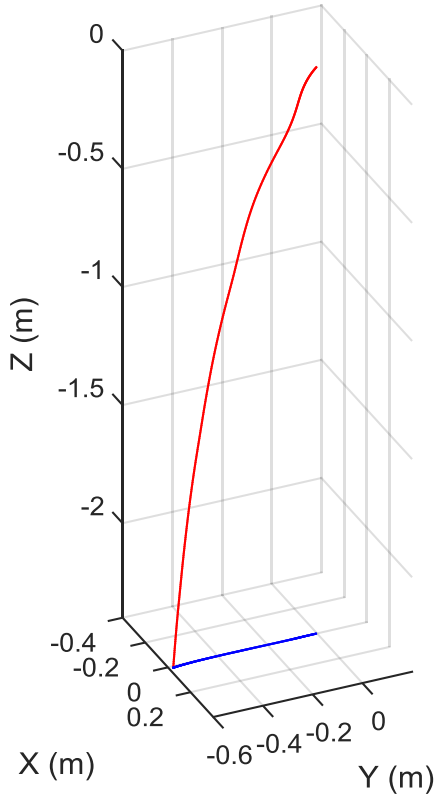

Fig. 4.39. Trajectory of cylinder #3 with drop angle 45^o: (b) DROBS

Table 4.9: Comparison of landing points for Cylinder #3

Landing points	Experimental results - Chu et al. (2005)	Simulated results - Chu et al. (2005)	Simulated results-DROBS
X (m)	0.00	0.00	0.00
Y (m)	-0.56	-0.30	-0.58

At last,the effect of different LCGs on the trajectories are studied. For cylinder #2, the same initial conditions as in Eq. (4.94) are used for numerical simulation in DROBS, except that the LCG is modified. As indicated in Fig. 4.40, the trajectory expands outward when LCG is shifted from aftbody (-0.0074m) over the center (0.0m) to the forebody (+0.0074m). Quantitatively, the total excursion of the landing point decreases from 0.50m over 0.45m to 0.42m. Simulation

data is summarized in Table 4.10. The calculated difference ratios are -10.10% and -7.13%, respectively.

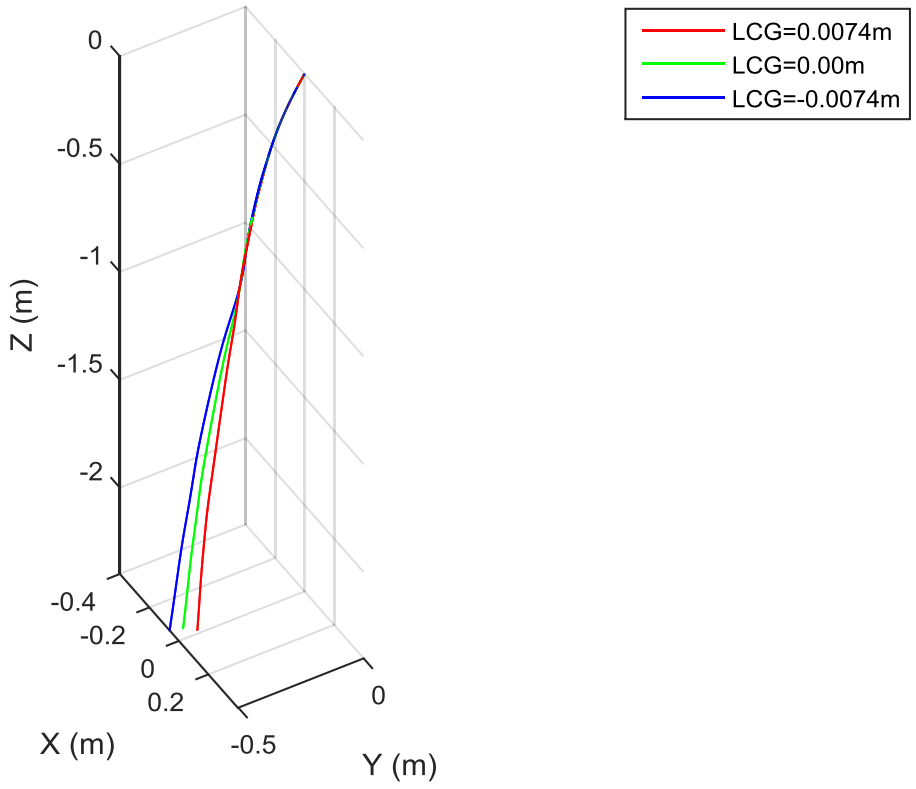

Fig. 4.40. Trajectory of cylinder #2 with varying LCG, drop angle 45^o

Table 4.10: Simulated landing points for cylinder #2

	Case (a)	Case (b)	Case (c)
Landing points	LCG = -0.0074m	LCG = 0.0m	LCG = +0.0074m
X (m)	-0.06	-0.05	-0.02
Y (m)	-0.50	-0.45	-0.42
Excursion (m)	0.50	0.45	0.42
Diff. Raito	N/A	-10.10%	-7.13%

Note: (1) Excursion = $\sqrt{X^2 + Y^2}$ (2) Diff. Ratio = Excursion (b) - Excursion (a) / Excursion (a) or Excursion (c) - Excursion (b) / Excursion (b)

The results show that LCG greatly influence the underwater trajectory of dropped cylinders and corresponding landing points. This emphasizes the importance of adjusting the position LCG of test specimen when preparing in model tests. Small discrepancies may cause significant differences in the observed motion.

4.5 Dropped objects under current

In Fig. 4.41, $OXYZ$ is the global coordinate system, where $X-Y$ represents the still-water surface and Z-axis points vertical upwards. The other coordinate system $oxyz$ is a local coordinate system fixed to the cylinder, where the x-axis is the cylinder axis, in tangent direction, y-axis is in binormal direction, and z-axis is in normal direction. Its origin is located at the geometric center. Both $OXYZ$ and $oxyz$ coordinate systems coincide when the cylinder is situated on the water surface horizontally at the beginning. A 3D theory for dropped cylinders with non-zero LCG is described below (Aanesland, 1987; Xiang et al. 2016b):

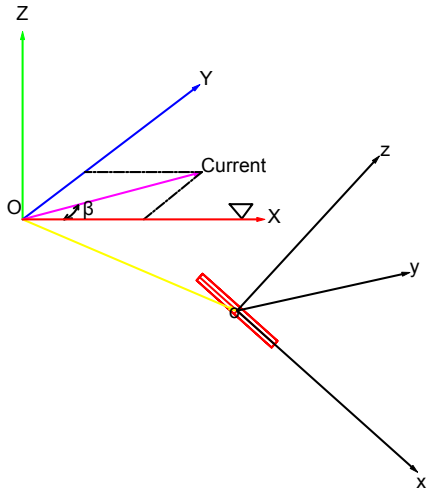

Fig. 4.41. Coordinate system for equation of motions in three dimensions

As shown in Fig. 4.41, a horizontal current is considered with the speed $V_{current}$ and heading angle, β. The velocity components of the current in X, Y and Z direction, V_{cX}, V_{cY}, and V_{cZ} may be expressed as

$$\begin{aligned} V_{cX} &= V_{current}\cos(\beta) \\ V_{cY} &= V_{current}\sin(\beta) \\ V_{cZ} &= 0 \end{aligned} \tag{4.96}$$

After the transformation from the global coordinate system ($OXYZ$) to the local coordinate system ($oxyz$) (John and Francis, 1962), the velocity components of the current in x, y, and z direction, V_{cX}, V_{cY}, and V_{cZ} can be expressed as

$$V_{cx} = V_{cX}\cos(\theta)\cos(\psi) + V_{cY}\cos(\theta)\sin(\psi) \tag{4.97}$$

$$\begin{aligned} V_{cy} =& V_{cX}\{-\cos(\phi)\sin(\psi) + \sin(\phi)\sin(\theta)\cos(\psi)\} \\ &+ V_{cY}\{\cos(\phi)\cos(\psi) + \sin(\phi)\sin(\theta)\sin(\psi)\} \end{aligned} \tag{4.98}$$

$$\begin{aligned} V_{cz} =& V_{cX}\{\sin(\phi)\sin(\psi) + \cos(\phi)\sin(\theta)\cos(\psi)\} \\ &+ V_{cY}\{-\sin(\phi)\cos(\psi) + \cos(\phi)\sin(\theta)\sin(\psi)\} \end{aligned} \tag{4.99}$$

To be determined are the local relative velocities: U_x, $U_y(x)$ and $U_z(x)$ in x, y and z-axis direction between the water and points on the cylinder:

$$\begin{aligned} U_x &= V_{cx} - U_1 \\ U_y(x) &= V_{cy} - (U_2 + \Omega_3 x). - 0.5L < x < 0.5L \\ U_z(x) &= V_{cz} - (U_3 + \Omega_2 x). - 0.5L < x < 0.5L \end{aligned} \tag{4.100}$$

4.5.1 Uniform current

For the purpose of simplicity, we only consider the effects of a uniform current and ignore effects of waves. Also, Luo and Davis (1992) found that the horizontal excursion at the seabed level is heavily influenced by currents but waves have limited effects on overall horizontal excursion. This may be because the wave effects on dropped objects will decay very fast with the increasing submergence. So it is more worthwhile to discuss the effects of currents on the trajectory of dropped cylinders below the water. Cylinder #2 with the same initial conditions

as expressed in Eq. (4.94) is dropped into water with 0.5m/s uniform current along the water depth. The heading angles, β are at 0^o, 90^o, 180^o, and 270^o. Correspondingly, the simulated trajectories of the center of gravity of the cylinder are shown in Fig. 4.42.

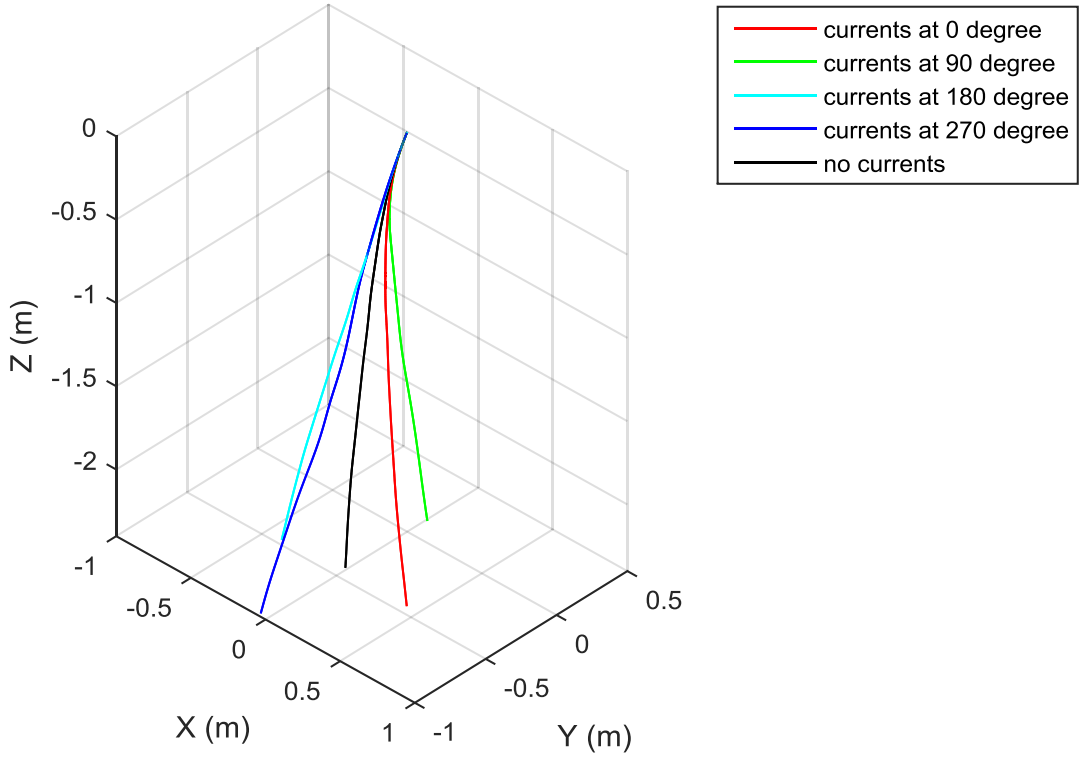

Fig. 4.42. Trajectory of cylinder #2 under current from direction: β at $0^o, 90^o, 180^o, 270^o$

Table 4.11: Comparison of landing points

Case Number	1	2	3	4	5
Landing points	No current	Current at 0^o	Current at 90^o	Current at 180^o	Current at 270^o
X (m)	-0.02	0.40	0.00	-0.39	-0.05
Y (m)	-0.42	-0.43	0.13	-0.46	-0.97
T (s)	1.228	1.228	1.236	1.232	1.354
Difference X(m)	0.00	0.42	0.02	-0.37	-0.03
Difference Y(m)	0.00	-0.01	0.55	-0.04	-0.55
Difference T(s)	0.00	0.00	0.008	0.004	0.126

Note: (1) Difference X = X(Case N)- X(Case 1), N=1, 2, 3, 4, and 5

Difference Y = Y(Case N)- Y(Case 1), N=1, 2, 3, 4, and 5

Difference T = T(Case N)- T(Case 1), N=1, 2, 3, 4, and 5

(2) T is the duration time till dropped cylinder lands at the seabed

As shown in Fig. 4.42, the trajectory of the cylinder and the landing point are significantly influenced by the current. In Table 4.11, with current at β= 0^o, the landing point shifts in positive X direction and negative Y direction by 0.42m and 0.01m respectively. With a current heading of 180^o, the landing point shifts in negative X direction and negative Y direction by 0.37m and 0.04m. With transverse current at β= 90^o, the cylinder moves first in negative Y direction according to initial condition but turn to positive Y direction at some point in time. Also, the landing point shifts in positive X direction and positive Y direction by 0.02m and 0.55m, respectively. With currents at β= 270^o, the landing point shifts in negative X direction and negative Y direction by 0.03m and 0.55 m respectively. For a heading of 270^o, the drop time is longest.

Then, Cylinder #2 with the same initial conditions as expressed in Eq. 4.94 is dropped again into water with uniform current at fixed incoming angle β at 270^o but various current velocities. The resultant simulated trajectories of the cylinder are shown in Fig. 4.43.

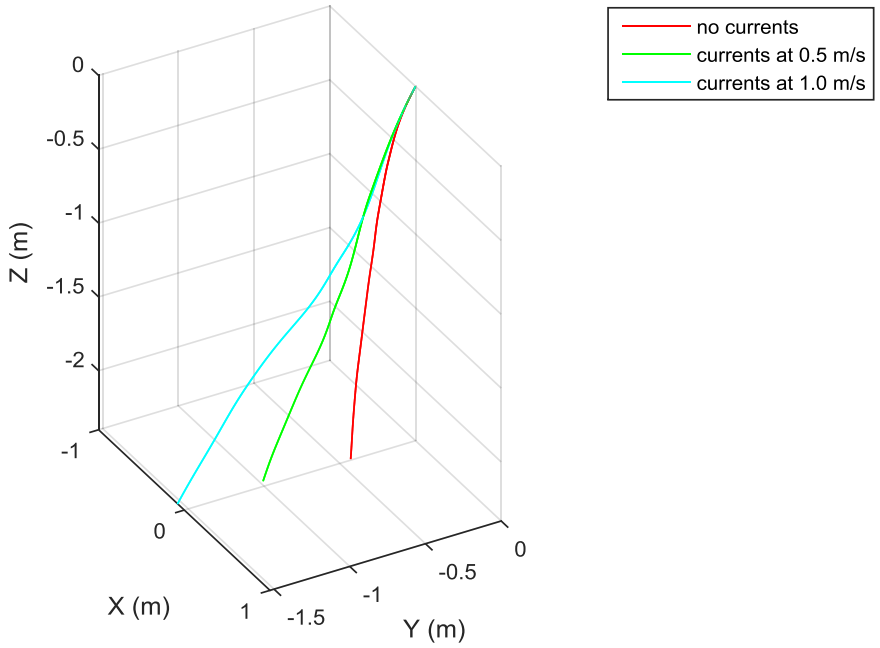

Fig. 4.43. Trajectory of cylinder #2 under current at 0m/s, 0.5m/s, and 1.0m/s

Table 4.12: Comparison of landing points

Case Number	1	2	3
Landing points	No current	Current at 0.5m/s	Current at 1.0m/s
X (m)	-0.02	-0.05	-0.08
Y (m)	-0.38	-0.96	-1.52
T (s)	1.228	1.354	1.264
Difference X(m)	0.00	-0.03	-0.06
Difference Y(m)	0.00	-0.58	-1.14
Difference T(s)	0.00	0.126	0.036

Note: (1) Difference X = X(Case N)- X(Case 1), N=1, 2, 3, 4, and 5

Difference Y = Y(Case N)- Y(Case 1), N=1, 2, 3, 4, and 5

Difference T = T(Case N)- T(Case 1), N=1, 2, 3, 4, and 5

(2) T is the duration time till dropped cylinder lands at the seabed

As shown in Fig. 4.43, increasing current with 0 m/s to 1.0m/s pushes trajectory and landing point of the cylinder in the direction of the current. With current at 0.5m/s, landing point moves in negative X direction and Y direction by 0.03m and 0.58m. With current increasing to 1.0m/s, the landing point shifts in negative X direction and Y direction by 0.06m and 1.14m.

Chapter 5

Statistical study on landing points of dropped cylindrical object falling through air-water columns

5.1 Monte Carlo method

Cylinder #4 (Awotahegn, 2015) is a model of a drilling pipe dropped from 1.2m above the water surface surface into water with depth d= 3.0m, as shown in Fig 5.1. The properties of Cylinder #4, are described in Table 5.1.

Table 5.1: Properties of the Cylinder #4

Parameters	Unit	Model Scale (1:16.67)
Length (L)	m	0.537
Mass density (ρ_c)	kg/m	0.325
Diameter	m	0.013
LCG	m	0.000

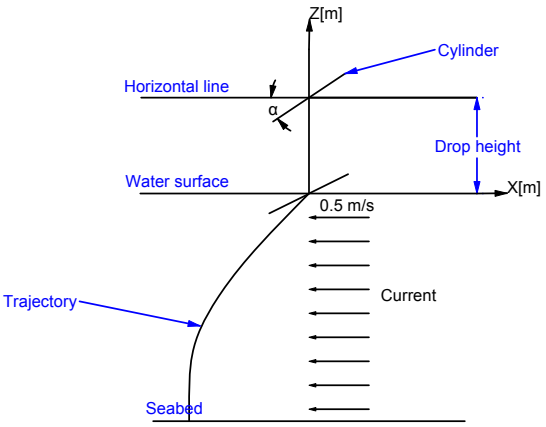

Fig. 5.1. Set up of the drop test under uniform current

The effect of falling through the air can be mostly ignored but a dropped object experiences large impact forces and moments when it hits the water surface. Air may be entrapped in the wake of the object. Most existing studies on water impact are for 2-D bodies and based on a flat (Von Karman, 1929) or near-flat (Wagner, 1931) free surfaces. Recently, a generalized Wagner theory approach (Mei et al., 1999), based on the extension of Wagner's asymptotic theory to arbitrary body geometry and entry angle, has been developed and has shown to be quite effective for arbitrary 2-D bodies. Sun and Faltinsen (2007) developed a two-dimensional boundary element method (BEM) to simulate the water flow during the water impact of a horizontal circular cylinder. The non-viscous flow separation on the curved surface of the cylindrical was simulated by merging a local analytical solution with the numerical method. These analytic and semi-analytic approaches can be readily applied to 3-D bodies. After the impact with the water surface, an air entrainment may be formed behind the object. Based on the experimental study of water entry of a circular disk at low Froude numbers, a simple effective model for the computation of the drag on the disk due to the entrained air has been developed in Gaudet (1998) and Glasheen and McMahon (1996). Lee et al. (1997) developed a more complex numerical model for very high Froude numbers that considers the motion of the projectile and the nonlinear evolution of the free surface. However, in the practical application of predicting the underwater trajectory and landing points of dropped cylinders,

exact values of the cylinder's physical parameters and the cylinder's release conditions will not be known. In addition, the environment is often quite irregular, so that the water entry introduces significant uncertainties into the initial conditions. In this case, it is useful to use stochastic models to describe the water entry process(Xiang et al., 2016).

Monte Carlo simulation is one of the most powerful and commonly used techniques for analyzing complex physical problems and uncertainty propagation, where the goal is to determine how random variation, lack of knowledge, or errors affect the sensitivity, performance, or reliability of the system that is being modeled. Applications can be found in diverse areas from radiation transport to river basin modeling. Important Navy applications include the analysis of antisubmarine warfare exercises and operations, prediction of aircraft or sensor performance, tactical analyses, and matrix game solutions where random processes are considered to be of particular importance. The range of applications has been broadening and the size, complexity, and computational effort have been increasing. However, such developments are expected and desirable since increased realism is concomitant with more complex and extensive problem descriptions(McGrath et al., 1973; Metropolis, 1987).

Monte Carlo simulation is categorized as a sampling method because its input is randomly generated from probability distributions to simulate the process of sampling from an actual population (*Monte Carlo Simulation Basics* 2004; Dubi, 2000). As shown in Fig 5.2, the variables $x1, x2$, and $x3$, etc are assumed to follow a probability distribution that most closely matches data we already have, or best represents our current state of knowledge. The random variables will be detailed described in section 5.2. Since DROBS has been verified to be capable of accurately predicting the landing points of dropped cylinders, DROBS is used as the model function $f(x)$ here (Bolton, 1998). The data (y_1,y_2, etc) generated from the simulation are the excursion of landing points which can be represented as probability distributions (or histograms), reliability predictions, and confidence intervals.

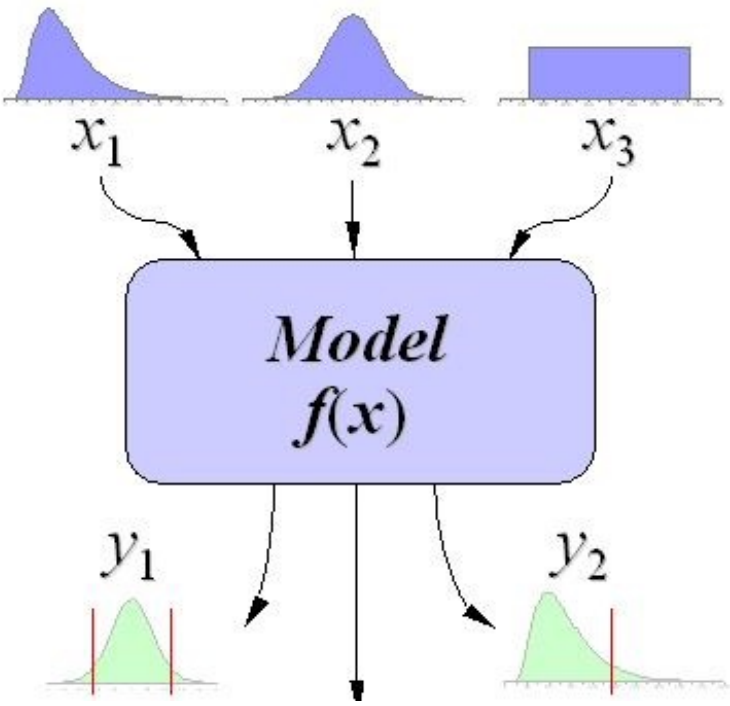

Fig. 5.2. Schematic showing the principal of stochastic uncertainty propagation (*Monte Carlo Simulation Basics* 2004)

5.2 Description of random variables

Variables of motion including initial orientation angles (ϕ_0,θ_0,ψ_0), translational velocity ($\dot{X}_0$,$\dot{Y}_0$,$\dot{Z}_0$), and rotational velocity (Ω_{10},Ω_{20},Ω_{30}) when the cylinder gets fully immersed are the initial conditions of the DROBS simulations. Since the equations of motion are stated in the local coordinate system, translational velocities($\dot{X}_0$,$\dot{Y}_0$,$\dot{Z}_0$) in the global coordinate system need to be transformed into the local coordinate system (U_1,U_2,U_3). The track of the center of gravity of cylinders falling through the air is perpendicular to the water surface. During the water entry process, the perturbation of the velocity of the center of gravity is considered small in X and Y direction. So ϕ_0=0, $\dot{X}_0$=0, $\dot{Y}_0$=0. The remaining 6 variables (θ_0,ψ_0,$\dot{Z}_0$,Ω_{10},Ω_{20},Ω_{30}) are called the random variables which are assumed to be independent and follow its own normal distribution, N(μ,σ^2).

5.2.1 Fundamentals of distribution selection

Selection of an appropriate probability distribution for a given random variable in a simulation requires gathering and evaluating all the available facts, data, and knowledge concerning

each variable. It is also important to know how the particular process which any given variable represents relates to the entire simulation model. When the variable under consideration is just one among many variables which affect the overall problem or system, the simulation might not be sensitive to the choice of the distribution. This can be likened to the phenomenon of summing a series of random variables, none of which dominates the sum. In this case the total tends to have a normal distribution irrespective of the individual distributions. Choosing the form of probability distributions is often a tradeoff between theoretical justification and empirical evidence. Typically, some form of parametric distribution can be justified, such as the normal, uniform, binomial, or Bernoulli distribution. Available data can then be used to estimate its parameters. In the absence of empirical data, one is forced to choose distributions on either theoretical or intuitive grounds, or often to use several distributions and conduct sensitivity or worst-case analyses. In this study, empirical data for the random variables: (θ_0,ψ_0,$\dot{Z}_0$,Ω_{10},Ω_{20},Ω_{30}) are very limited. Therefore, a normal distribution is selected for all random variables. A sensitivity test is performed next.

5.2.2 Sensitivity analysis

The purpose of a sensitivity analysis is to determine the extent to which the outcome of an analysis is dependent upon a particular variable or assumption. It is particularly applicable to simulations where little or no data is available to characterize some random variables. In such a situation, sensitivity analysis can indicate whether or not the behavior of a variable must be more accurately known. If, for instance, the outcome of the simulation is insensitive to the variable, no further effort to characterize it is necessary. However, if it does prove sensitive, an attempt is warranted to develop an accurate distribution model. In addition, sensitivity analysis determines the extent to which the final results of the simulation study are sensitive to a given probability distribution. At this time, it's necessary to attain a determination of sensitivity to the parameters of a given distribution. It might be reasonable to vary the parameters to some extent in both directions. Suppose, for example, that a normal distribution with mean 100 and standard deviation 20 is postulated. Then five runs might be made to test sensitivity of the final simulation results to these parameters as follows [(mean, standard deviation)]: (100, 20), (110, 20), (90, 20), (100, 18). (100, 22). (McGrath et al., 1973)

The out of plane motion (ψ_0,Ω_{10},Ω_{30}) is assumed to be not significantly influenced by the impact, so that the mean value μ is equal to the initial value at the drop point and has a very

small standard deviation σ from mean value μ. This assumption means that variables tend to stay at the starting status with no change or very small change during the water entry process. Variables: Ω_{20} and θ_0, for in plane motion (xz plane) are influenced significantly during the water entry process (Wei and Hu, 2015). Thus larger standard deviation values σ are used with 3 for Ω_{20} , 0.6 for θ_0. The mean value of Ω_{20} and θ_0 are kept the same as their initial value at the drop point. Because of energy losses during the water entry process, $\dot{Z}_0$ decreases starting from V_{max}. V_{max} is the maximum velocity of a dropped cylinder before entering the water and estimated by the law of conservation of energy, Eq. (5.1).

$$V_{max} = \sqrt{2gh} \tag{5.1}$$

It's difficult to estimate how much energy will dissipate during the water entry process. Therefore the mean value for $\dot{Z}_0$ is tested with values of 10% velocity loss, 25% velocity loss, and 50% velocity loss. The standard deviation σ is set to a small value: 0.1. The specifications of random variables are shown in Table 5.2

Table 5.2: Specifications of random variables

Random Variables	Units	Normal Distribution, $N(\mu, \delta^2)$
θ_0	rad	$N(\mu, 0.6^2)$
ψ_0	rad	$N(0, 0.1^2)$
$\dot{Z}_0$	m/s	$N(0.9V_{max}, 0.1^2)$ $N(0.75V_{max}, 0.1^2)$ $N(0.50V_{max}, 0.1^2)$
Ω_{10}	rad/s	$N(0, 0.1^2)$
Ω_{20}	rad/s	$N(0, 3.0^2)$
Ω_{30}	rad/s	$N(0, 0.1^2)$

5.3 Sampling process

The sample size used in the Monte Carlo simulations is 10000 which means randomly picking data 10000 times for random variable group (θ_0,ψ_0,$\dot{Z}_0$,Ω_{10},Ω_{20},Ω_{30}) . Every random variable is picked based on its own normal distribution, $N(\mu,\sigma^2)$. These 10000 samples will form a new sampling distribution, $N_0(\mu,\sigma^2)$. The theoretical normal distribution for θ_0 is $N(1.05,0.6^2)$ for drop angle 60^o plotted in Fig. 5.3. The sampling distribution is shown in Fig. 5.4.

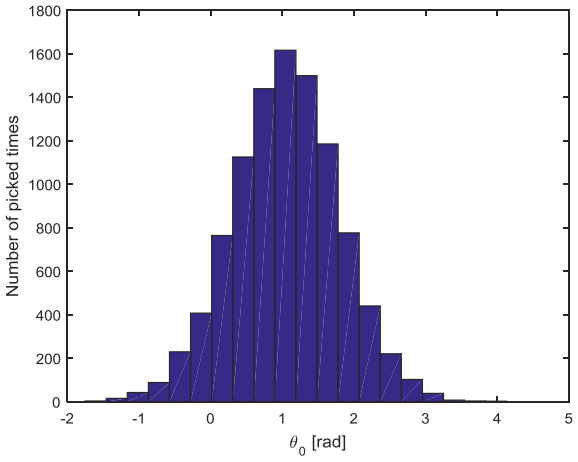

Fig. 5.3. Histogram of sampling distribution of θ_0

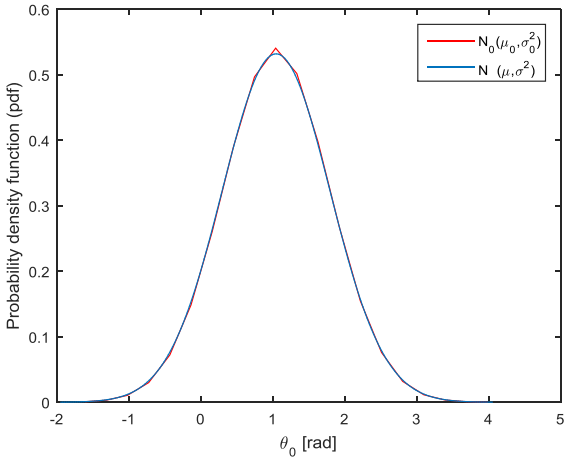

Fig. 5.4. PDF of sampling distribution and true distribution of θ_0

The theoretical normal distribution for Ω_{20} is $N(0,3^2)$ for drop angle 60^o (Fig. 5.5). The sampling distribution is shown in Fig. 5.6.

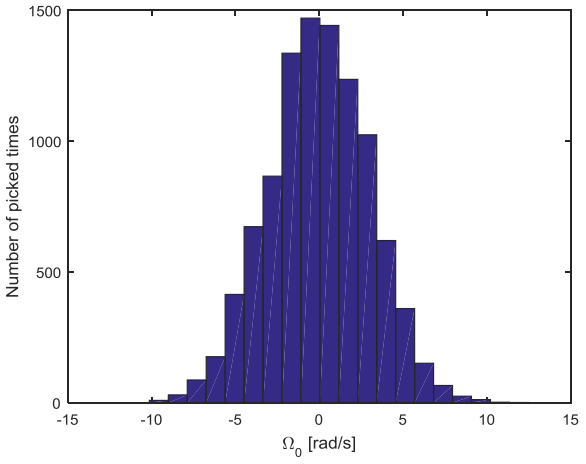

Fig. 5.5. Histogram of sampling distribution of Ω_0

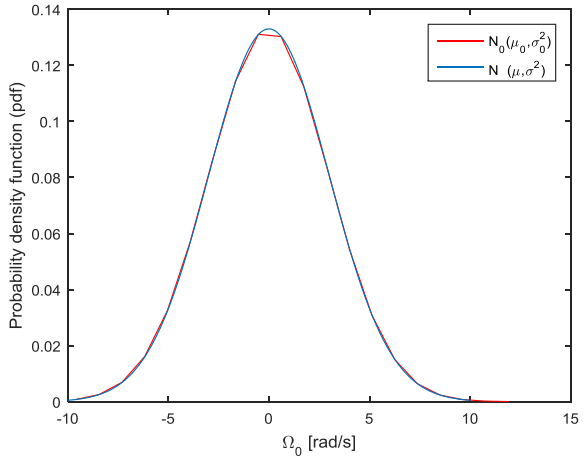

Fig. 5.6. PDF of sampling distribution and true distribution of Ω_0

5.4 Results of estimated landing point distribution under no current

5.4.1 DNV simplified method

In DNV's simplified method (DNV, 2010) the landing point on the seabed is assumed to be normally distributed. For the angular deviations, we have:

$$p(X) = \frac{1}{\sqrt{2\pi}\sigma} e^{-0.5(\frac{X}{\sigma})^2} \tag{5.2}$$

So the distance between landing point and the vertical line through the drop point will follow folded normal distribution:

$$p(R) = p(|X|) = \frac{2}{\sqrt{2\pi}\sigma} e^{-0.5(\frac{R}{\sigma})^2} \tag{5.3}$$

Where, $p(X)$ = Likelihood of a sinking object landing at position X

$p(R)$ = Likelihood of a sinking object landing at a distance R from the vertical line through the drop point

X = Position at the sea bottom (meters)

δ =$d\tan(\alpha_d)$: Lateral deviation (meters), d is the water depth, α_d is the angular deviation (degree)

R = Distance from the vertical line through the drop point at the sea bottom (meters)

The probability that a dropped object will land at the seabed within a distance r from the vertical line through the drop point is then expressed by the cumulative distribution function:

$$\begin{aligned} p(R \leq r) &= \int_0^r p(R)\mathrm{d}R \\ &= \mathrm{erf}(\frac{R}{\sqrt{2\delta^2}}) \end{aligned} \tag{5.4}$$

$$\mu_R = \sqrt{\frac{2}{\pi}}\delta \tag{5.5}$$

erf is the error function; μ_R is the mean value of the folded normal distribution in Eq.(5.3). So the Statistical values of the landing point distributions on the sea bed are presented in Table 5.3.

Table 5.3: Landing point distribution from simplified method in DNV (2010)

DNV simplified method	
Mean (m)	SD (m)
0.64	0.80

5.4.2 Monte Carlo method: sensitivity analysis of mean value for $\dot{Z}_0$

As shown in Figs. 5.7-5.9, landing point distributions for Cylinder #4 with drop angle 60^o without current are obtained by multiple Monte Carlo simulations using DROBS. The mean value for $\dot{Z}_0$ is set according to 10% velocity loss, 25% velocity loss and 50% velocity loss after being fully immersed into water. And other variables follow $\psi_0 \sim N(0, 0.1^2)$, $\theta_0 \sim N(\alpha, 0.6^2)$, $\Omega_{10} \sim N(0, 0.1^2)$, $\Omega_{20} \sim N(0, 3^2)$, $\Omega_{30} \sim N(0, 0.1^2)$.

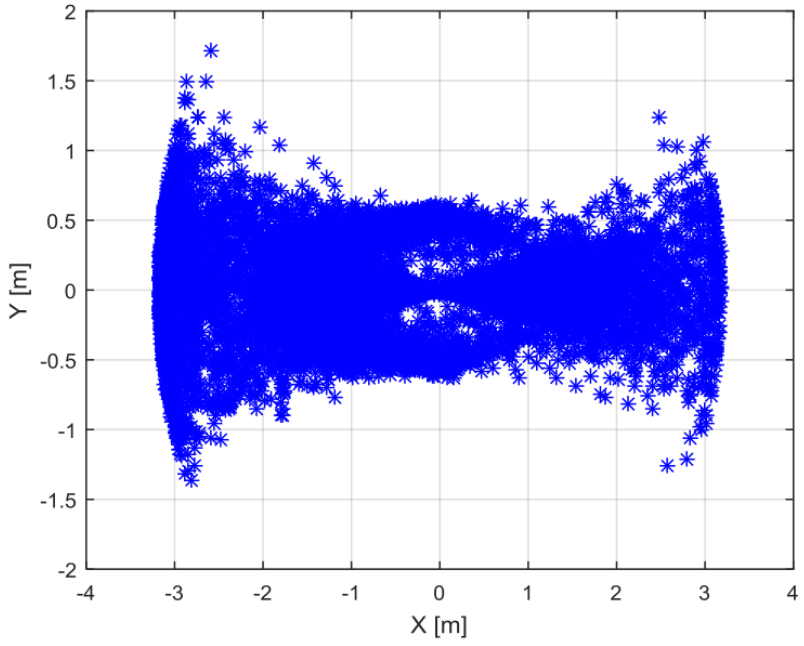

Fig. 5.7. Landing point distribution drop angle 60^o with $\dot{Z}_0 \sim N(0.90V_{max}, 0.1^2)$

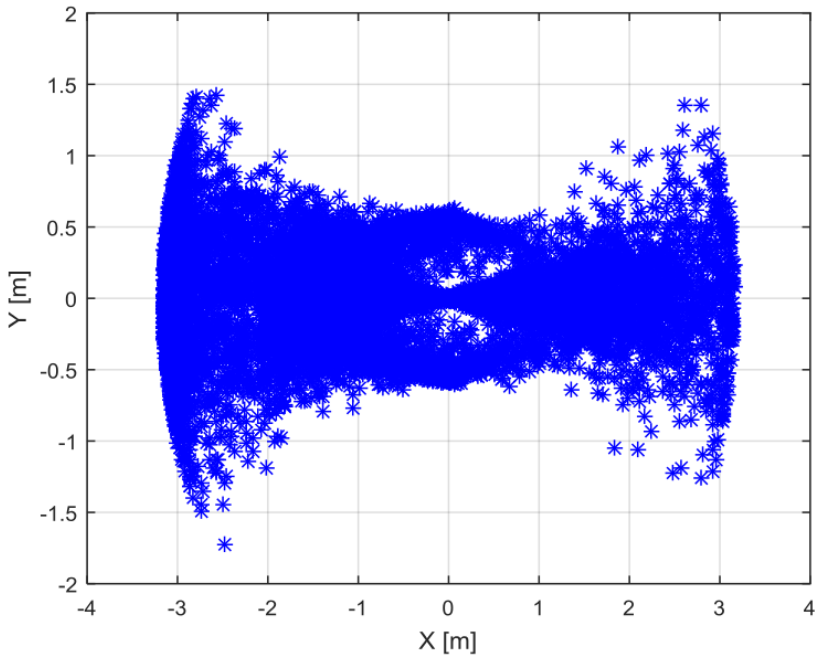

Fig. 5.8. Landing point distribution drop angle 60^o with $\dot{Z}_0 \sim N(0.75V_{max}, 0.1^2)$

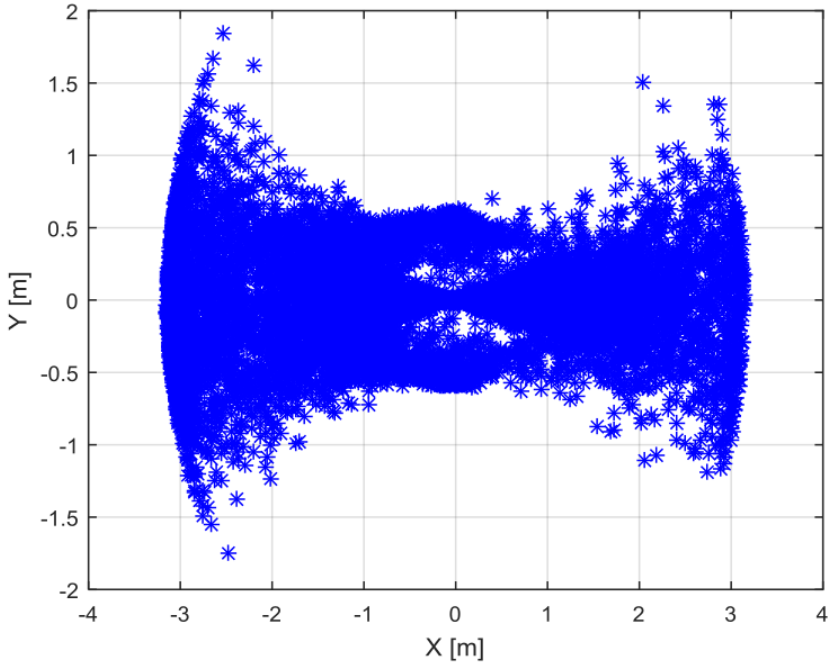

Fig. 5.9. Landing point distribution drop angle 60^o with $\dot{Z}_0 \sim N(0.50V_{max}, 0.1^2)$

Statistical values including mean, median, maximum (Max), minimum (Min), and standard deviation (SD) of excursion of landing points from DROBS based simulated results in Table 5.4 are compared with experimental results (Awotahegn, 2015) as shown in Table 5.5. It's found that:

- when the mean value of $\dot{Z}_0$varies from 0.90Vmax to 0.50Vmax , statistical values of excursion of landing points are not sensitive to the change of mean value of $\dot{Z}_0$;
- the DROBS based Monte Carlo simulation can provide reasonable results though the mean value and standard deviation of simulated results are slightly larger than from experimental results in Awotahegn, (2015).

Firstly, this may be because the sample size in experiments (Awotahegn, 2015) is very small compared with 10000 samples utilized in Monte Carlo simulations which caused the larger statistical values. Also, dropped cylinders with closed ends used in simulation will make a difference from open ends used in real experiments (Awotahegn, 2015) on trajectories. By comparing simulated results and experimental results (Awotahegn, 2015) with results from simplified method in DNV (2010) in Table 5.3, it shows the mean value from this simplified method is so small that results in underestimating the possible excursion of a landing point on the sea bed.

Table 5.4: Comparison of statistical value at different $\dot{Z}_0$ distribution

Simulated Results (DROBS)					
Distribution	Mean (m)	Median (m)	Max(m)	Min(m)	SD(m)
$\dot{Z}_0 \sim N(0.90V_{max}, 0.1^2)$	1.51	1.32	3.23	0.00	0.91
$\dot{Z}_0 \sim N(0.75V_{max}, 0.1^2)$	1.53	1.35	3.17	0.00	0.92
$\dot{Z}_0 \sim N(0.50V_{max}, 0.1^2)$	1.51	1.32	3.16	0.00	0.91

Table 5.5: Comparison of statistical value at different $\dot{Z}_0$ distribution

Experimental Results (Awotahegn, 2015)			
Mean (m)	Max(m)	Min(m)	SD(m)
1.13	2.30	0.40	0.42

5.4.3 Monte Carlo method: sensitivity analysis of value of standard deviation for θ_0 and Ω_2

θ_0 is assumed to follow $N(\mu, 0.6^2)$ and $N(0, 3^2)$ for Ω_2. To study the sensitivity of the standard deviation value used on the simulated results, θ_0 is assumed to follow $N(\mu, (0.6 + 0.01)^2)$ or $N(\mu, (0.6 - 0.01)^2)$ and Ω_2 is assumed to follow $N(0, (3 + 0.1)^2)$ or $N(0, (3 - 0.1)^2)$.

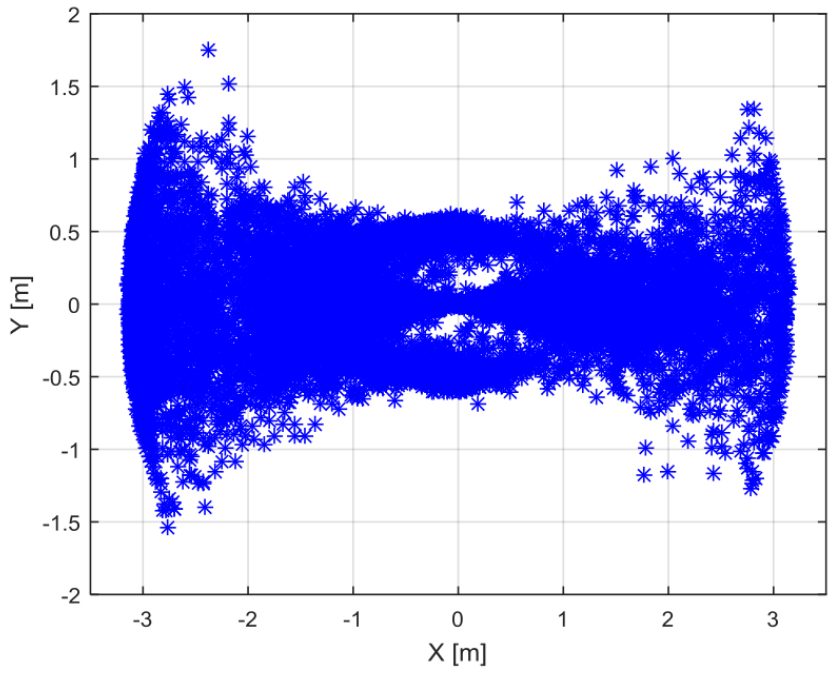

Fig. 5.10. Landing point distribution drop angle 60^o with $\theta_0 \sim N(1.05, (0.6 + 0.01)^2)$

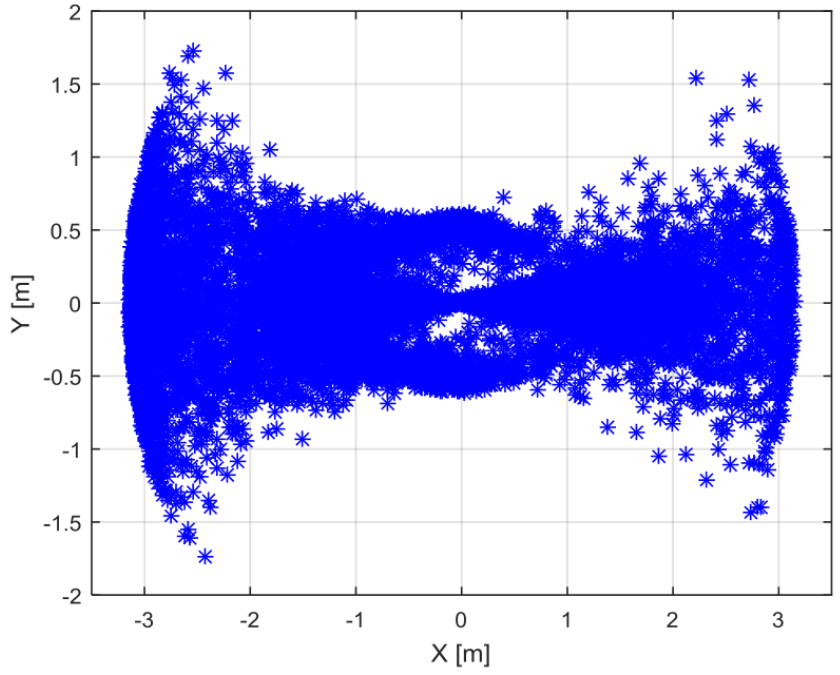

Fig. 5.11. Landing point distribution drop angle 60^o with $\theta_0 \sim N(1.05, (0.6 - 0.01)^2)$

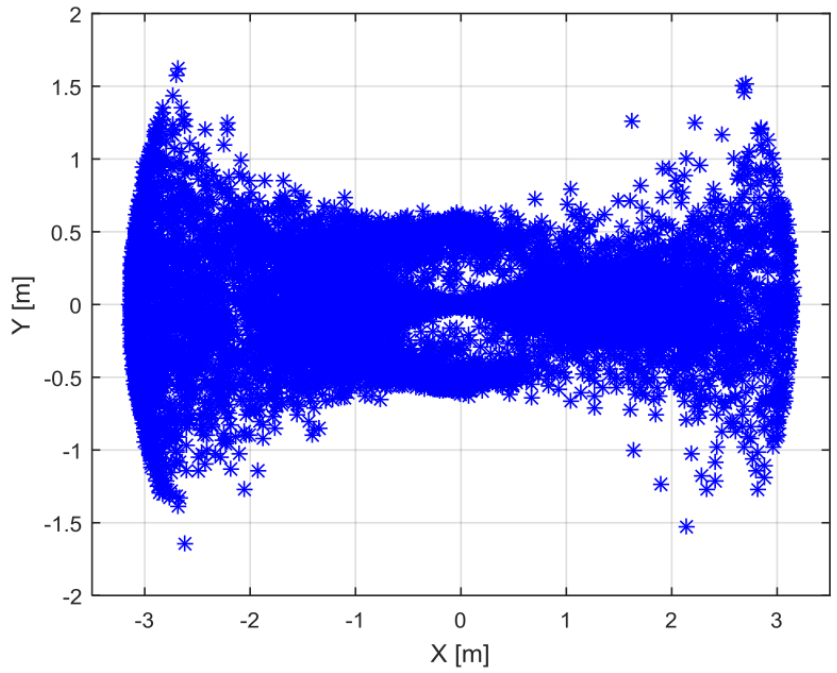

Fig. 5.12. Landing point distribution drop angle 60^o with $\Omega_0 \sim N(0, (3 + 0.1)^2)$

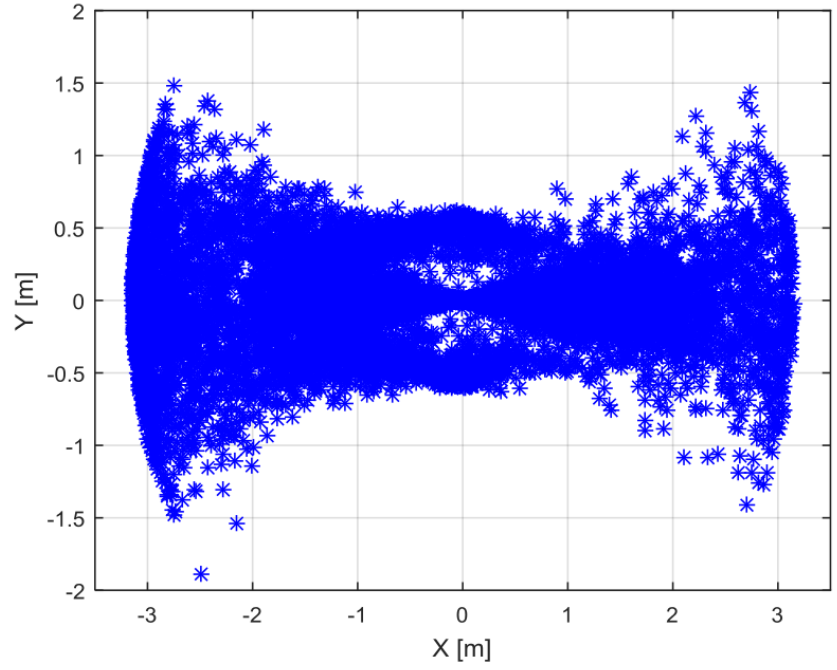

Fig. 5.13. Landing point distribution drop angle 60^o with $\Omega_0 \sim N(0, (3 - 0.1)^2)$

5.4.4 Simulated landing point distributions under uniform current

At drop angles $0^o, 15^o, 30^o, 45^o, 60^o, 75^o$, and 90^o, landing point distributions for Cylinder #4 under uniform current with velocity 0.5m/s and heading angle β = 180^o, are obtained from

Table 5.6: Comparison of statistical value at different $\dot{Z}_0$ distribution

Simulated Results (DROBS)					
Distribution	Mean (m)	Median (m)	Max(m)	Min(m)	SD(m)
$\theta_0 \sim N(1.05, (0.6+0.01)^2)$	1.51	1.29	3.16	0.00	0.91
$\theta_0 \sim N(1.05, (0.6-0.01)^2)$	1.54	1.34	3.18	0.00	0.92
$\Omega_0 \sim N(0, (3+0.1)^2)$	1.51	1.30	3.16	0.00	0.91
$\Omega_0 \sim N(0, (3-0.1)^2)$	1.52	1.33	3.16	0.00	0.91

Monte Carlo simulations and shown in Figs. 5.14-5.27. Corresponding histograms of the landing point distributions are provided at every drop angle to visualize the uncertainty in landing points distribution. It's found that landing points are most likely to be at R= 0.52m with drop angles increasing from 0^o to 60^o. For the drop angle 60^o, landing points are most likely to be located at two excursions: R= 0.52m and R =2.7m. With drop angles larger than 60^o $(60^o - 90^o)$, landing points are most likely to be at R =2.7m.

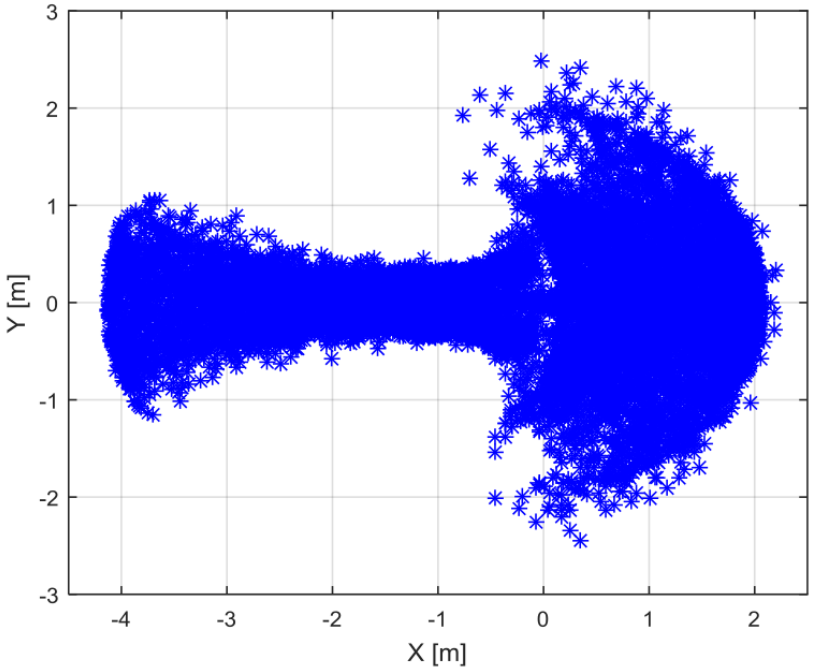

Fig. 5.14. Drop angle 0^o with $\dot{Z}_0 \sim N(0.5V_{max}, 0.1^2), \theta_0 \sim N(0, 0.6^2), \Omega_{20} \sim N(0, 3^2)$: (a) Landing point distribution

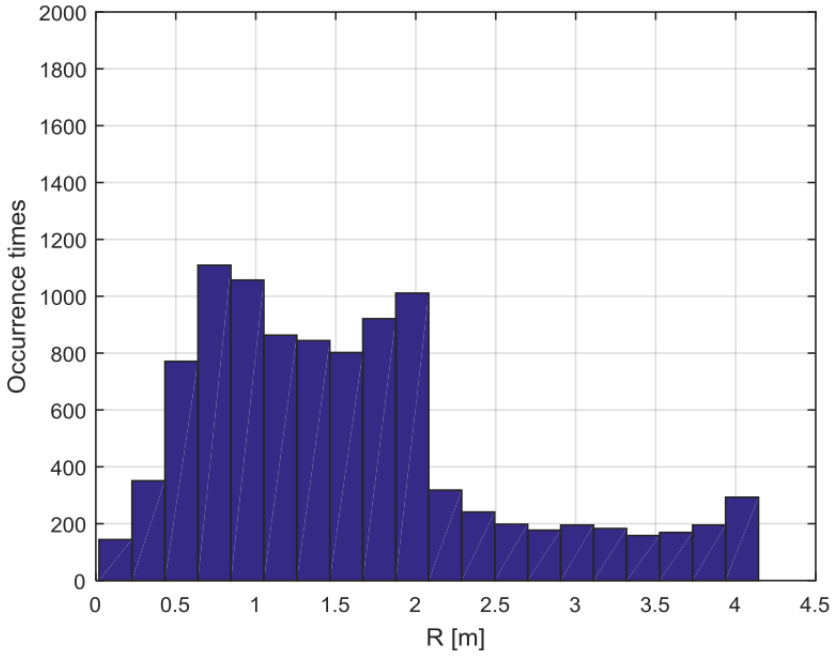

Fig. 5.15. Drop angle 0^o with $\dot{Z}_0 \sim N(0.5V_{max}, 0.1^2), \theta_0 \sim N(0, 0.6^2), \Omega_{20} \sim N(0, 3^2)$: (b) Histogram of excursion

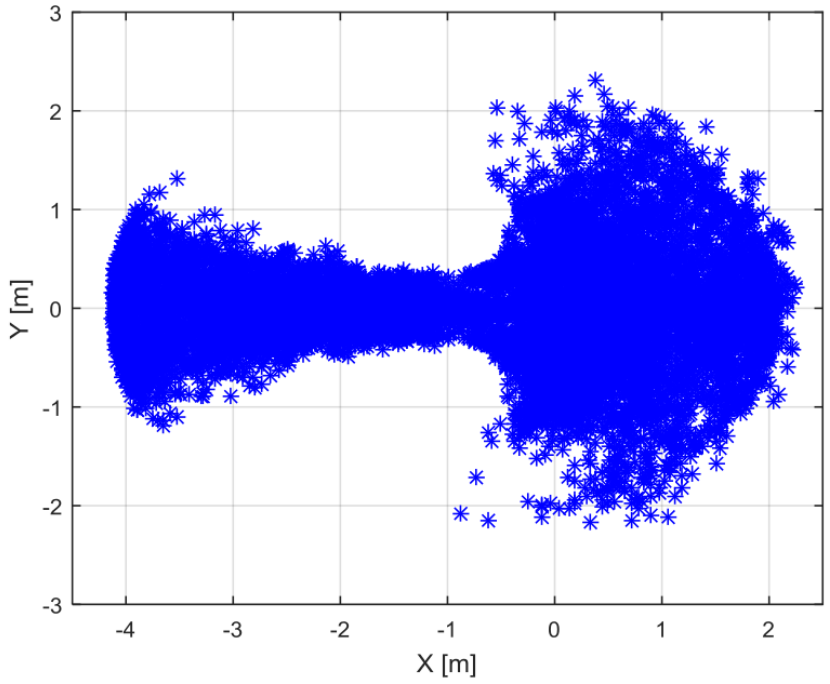

Fig. 5.16. Drop angle 15^o with $\dot{Z}_0 \sim N(0.5V_{max}, 0.1^2), \theta_0 \sim N(0, 0.6^2), \Omega_{20} \sim N(0, 3^2)$: (a) Landing point distribution

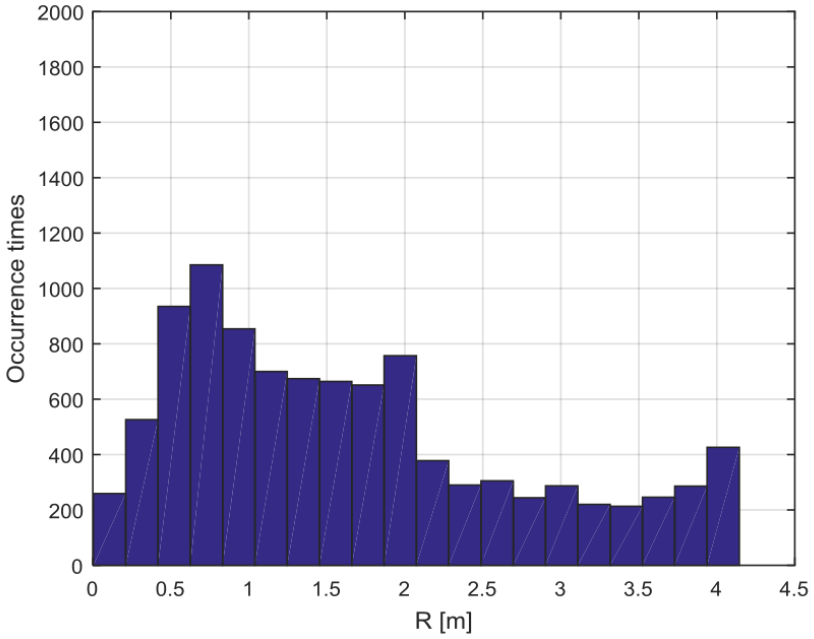

Fig. 5.17. Drop angle 15^o with $\dot{Z}_0 \sim N(0.5V_{max}, 0.1^2), \theta_0 \sim N(0, 0.6^2), \Omega_{20} \sim N(0, 3^2)$: (b) Histogram of excursion

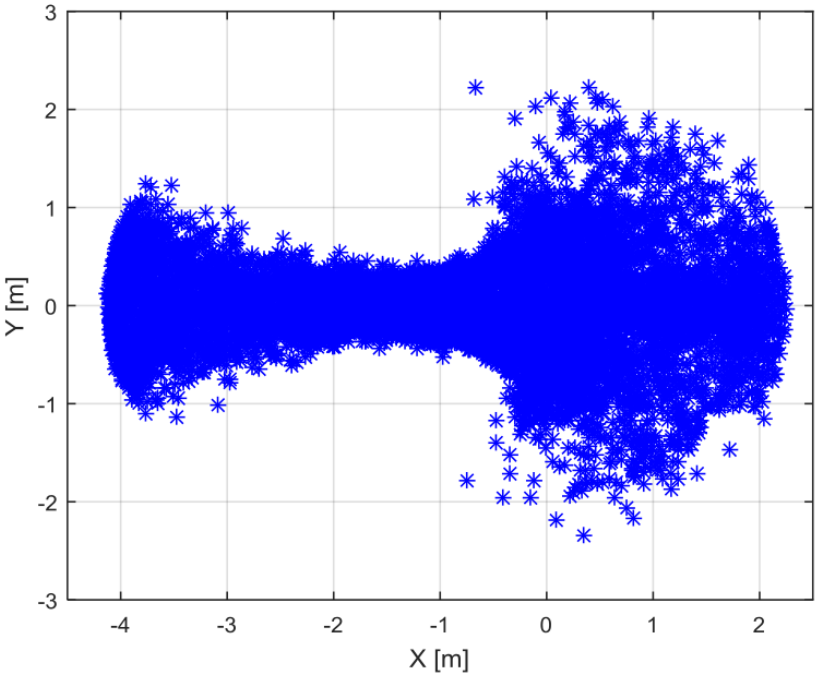

Fig. 5.18. Drop angle 30^o with $\dot{Z}_0 \sim N(0.5V_{max}, 0.1^2), \theta_0 \sim N(0, 0.6^2), \Omega_{20} \sim N(0, 3^2)$: (a) Landing point distribution

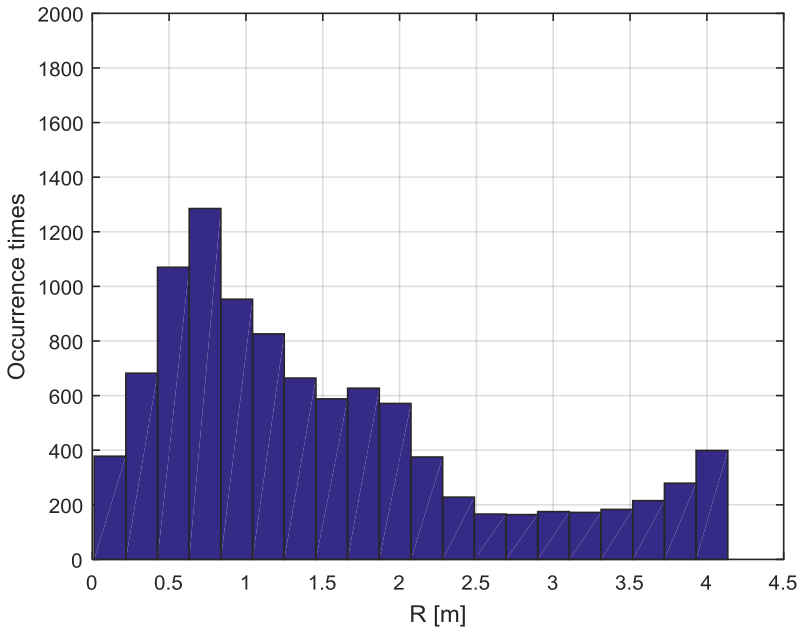

Fig. 5.19. Drop angle 30^o with $\dot{Z}_0 \sim N(0.5V_{max}, 0.1^2), \theta_0 \sim N(0, 0.6^2), \Omega_{20} \sim N(0, 3^2)$: (b) Histogram of excursion

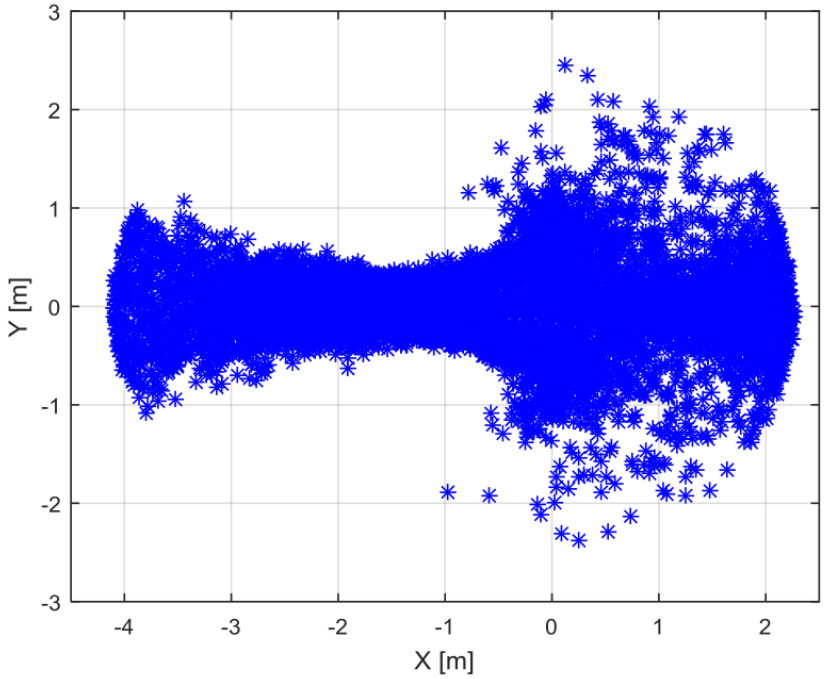

Fig. 5.20. Drop angle 45^o with $\dot{Z}_0 \sim N(0.5V_{max}, 0.1^2), \theta_0 \sim N(0, 0.6^2), \Omega_{20} \sim N(0, 3^2)$: (a) Landing point distribution

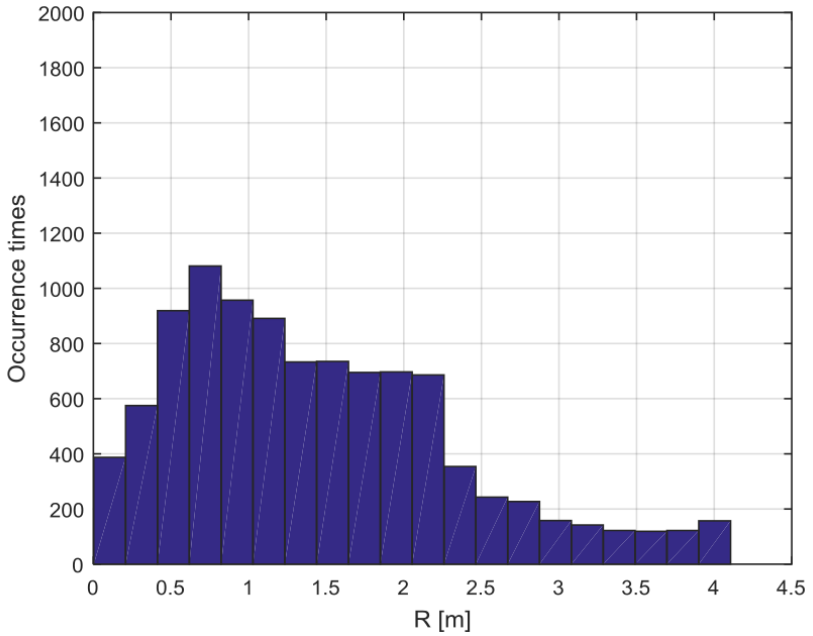

Fig. 5.21. Drop angle 45^o with $\dot{Z}_0 \sim N(0.5V_{max}, 0.1^2), \theta_0 \sim N(0, 0.6^2), \Omega_{20} \sim N(0, 3^2)$: (b) Histogram of excursion

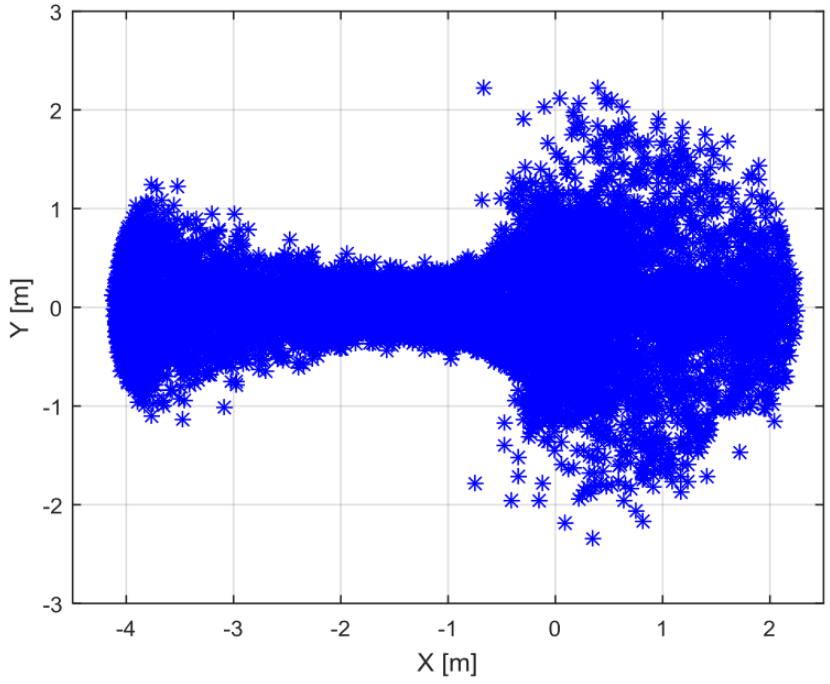

Fig. 5.22. Drop angle 60^o with $\dot{Z}_0 \sim N(0.5V_{max}, 0.1^2), \theta_0 \sim N(0, 0.6^2), \Omega_{20} \sim N(0, 3^2)$: (a) Landing point distribution

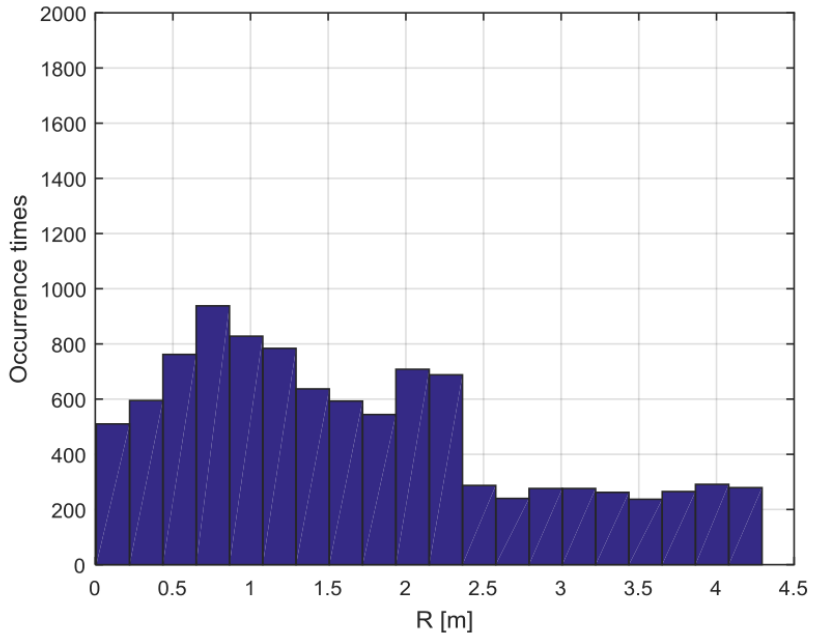

Fig. 5.23. Drop angle 60^o with $\dot{Z}_0 \sim N(0.5V_{max}, 0.1^2), \theta_0 \sim N(0, 0.6^2), \Omega_{20} \sim N(0, 3^2)$: (b) Histogram of excursion

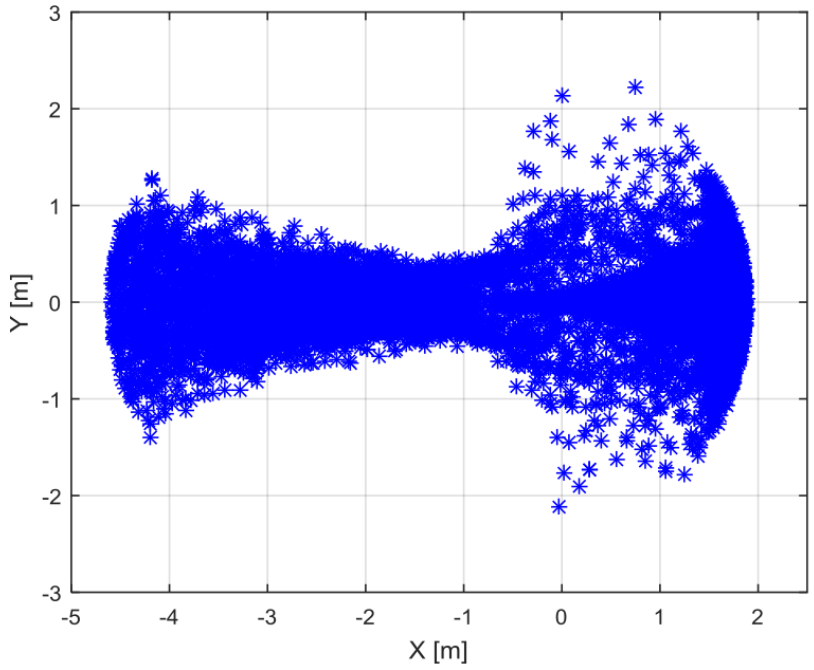

Fig. 5.24. Drop angle 75^o with $\dot{Z}_0 \sim N(0.5V_{max}, 0.1^2), \theta_0 \sim N(0, 0.6^2), \Omega_{20} \sim N(0, 3^2)$: (a) Landing point distribution

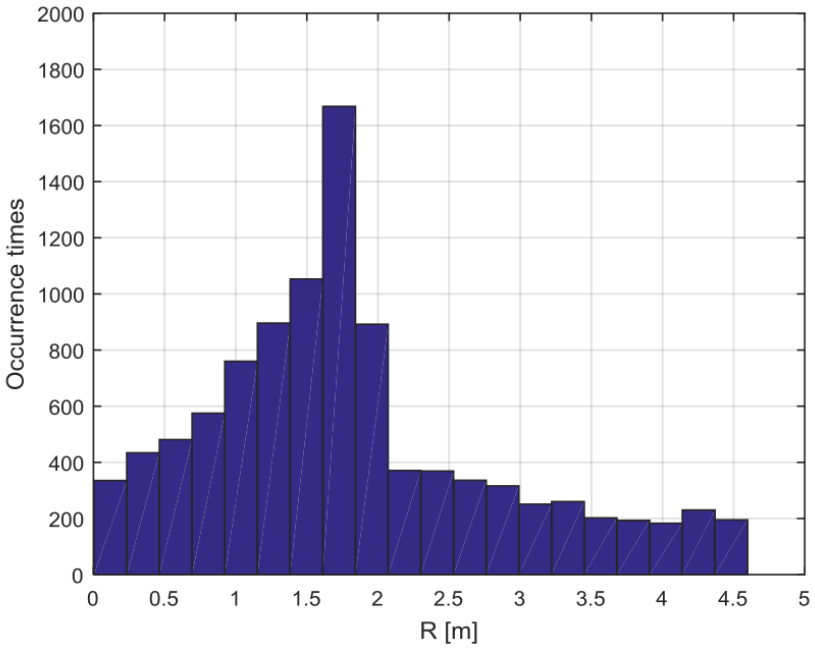

Fig. 5.25. Drop angle 75^o with $\dot{Z}_0 \sim N(0.5V_{max}, 0.1^2), \theta_0 \sim N(0, 0.6^2), \Omega_{20} \sim N(0, 3^2)$: (b) Histogram of excursion

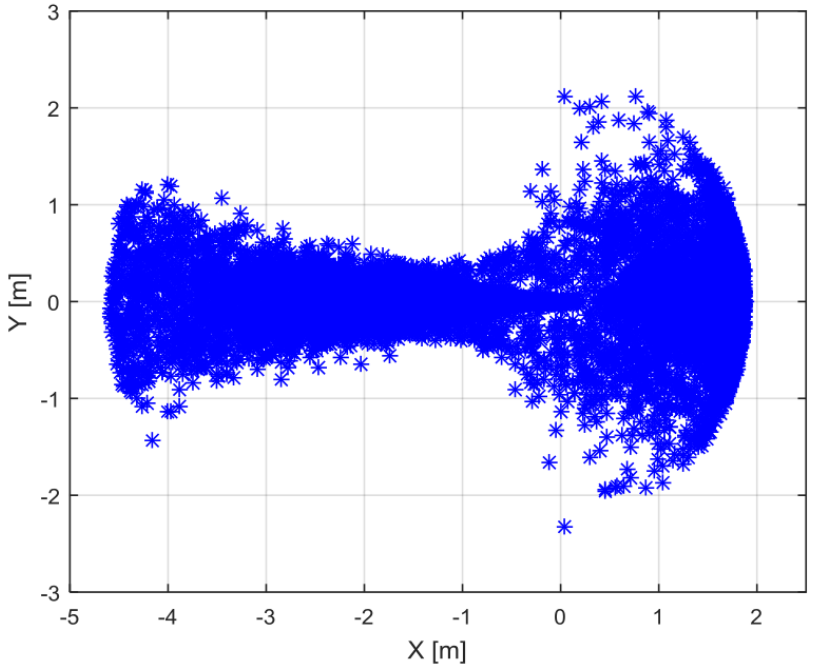

Fig. 5.26. Drop angle 90^o with $\dot{Z}_0 \sim N(0.5V_{max}, 0.1^2), \theta_0 \sim N(0, 0.6^2), \Omega_{20} \sim N(0, 3^2)$: (a) Landing point distribution

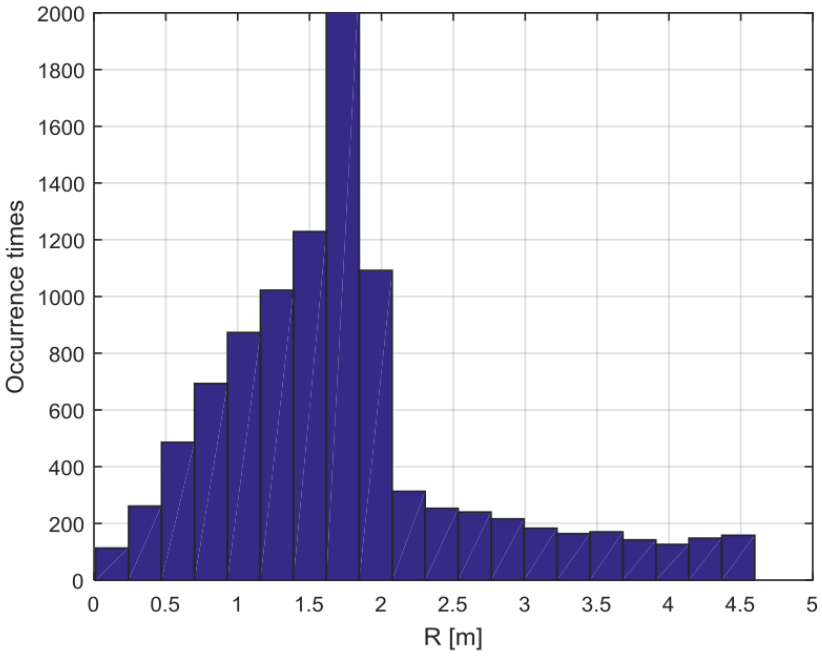

Fig. 5.27. Drop angle 90^o with $\dot{Z}_0 \sim N(0.5V_{max}, 0.1^2), \theta_0 \sim N(0, 0.6^2), \Omega_{20} \sim N(0, 3^2)$: (b) Histogram of excursion

5.5 Statistical analysis of simulated landing point distribution

5.5.1 Mean, Median, Maximum (Max), Minimum (Min), Standard Deviation (SD) and confidence interval of excursion

The statistical values of landing point excursions are shown in Table 5.7.

Table 5.7: Comparison of statistical values at different $\dot{Z}_0$ distributions

	Simulated Results				
Drop angle	Max(m)	Min(m)	Mean(m)	SD(m)	89% confidence interval(m)
0^o	4.14	0.02	1.59	0.94	0-4.41
15^o	4.14	0.00	1.66	1.08	0-4.90
30^o	4.13	0.01	1.51	1.07	0-4.72
45^o	4.10	0.00	1.45	0.91	0-4.18
60^o	4.29	0.00	1.70	1.12	0-5.06
75^o	4.60	0.00	1.83	1.04	0-4.95
90^o	4.60	0.01	1.75	0.90	0-4.45

The maximum mean value of excursion happens at drop angle, 75^o. By considering standard deviation and mean value together, 89% confidence interval can be obtained based on Chebyshev's inequality theory (Mood et al.1974) in Eq. (5.6). The maximum 89% confidence interval is between 0-5.06m at drop angle, 60^o.

$$p(|S-\mu| \geq k\delta) \leq \frac{1}{k^2}, k > 1 \tag{5.6}$$

When k=3, $p(|S-\mu| < 3\delta) \geq \frac{8}{9} \approx 89\%$. S is the random variable. So the 89% confidence interval is between $\mu - 3\delta$ and$\mu + 3\delta$.

5.5.2 Risk free zone

By analyzing all excursion data for drop angles is $0^o, 15^o, 30^o, 45^o, 60^o$, 75^o, and 90^o, an overall likelihood of landing points is represented by Probability Density Function (PDF) in Fig. 5.29 and Cumulative Distribution Function (CDF) in Fig. 5.30. It's found that there are two peaks in the PDF curve as depicted in Fig. 5.29 which means dropped cylinders are most likely to land at two different excursions: R=0.52m and R=2.7m. In contrast, DNV (2010) assumes dropped cylinders are most likely to land at R=0.

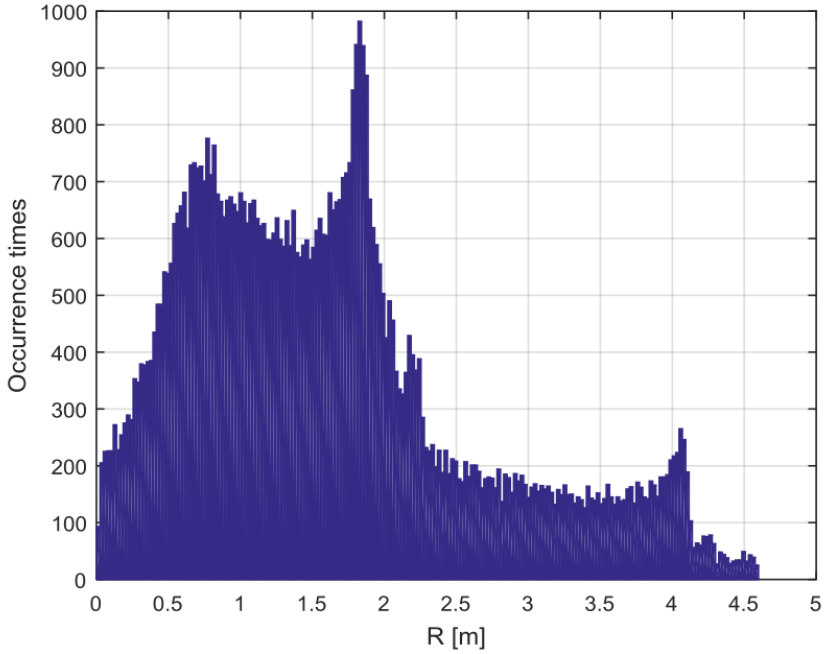

Fig. 5.28. Histogram of excursion of landing points, R with $\dot{Z}_0 \sim N(0.50V_{max}, 0.1^2), \theta_0 \sim N(0, 0.6^2), \Omega_{20} \sim N(0, 3^2)$

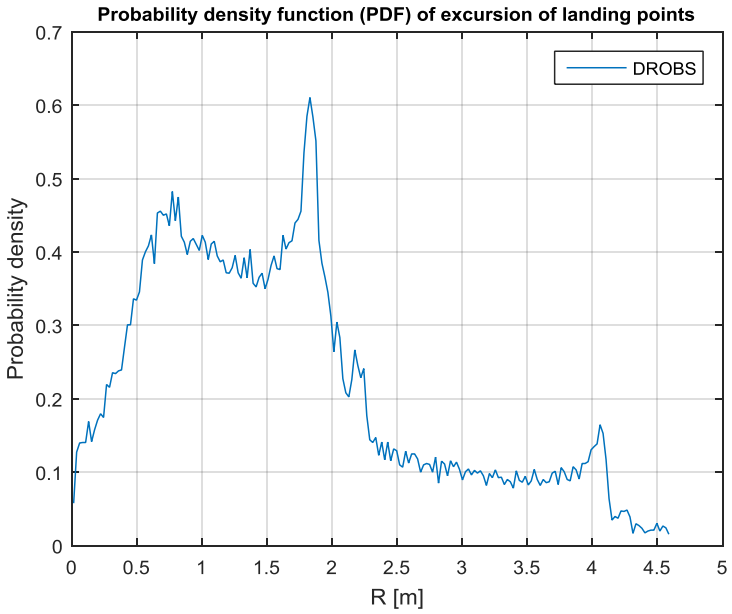

Fig. 5.29. PDF of excursion of landing points, R with $\dot{Z}_0 \sim N(0.50V_{max}, 0.1^2), \theta_0 \sim N(0, 0.6^2), \Omega_{20} \sim N(0, 3^2)$

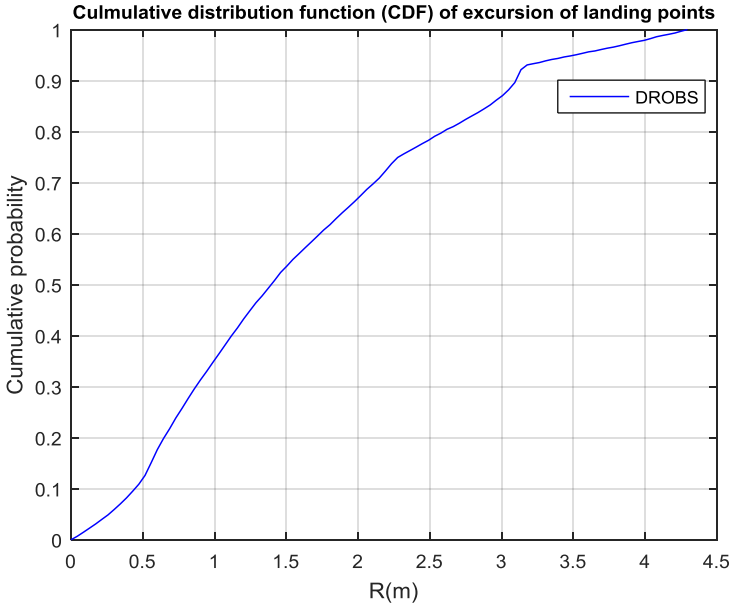

Fig. 5.30. CDF of excursion of landing points, R with $\dot{Z}_0 \sim N(0.50V_{max}, 0.1^2), \theta_0 \sim N(0, 0.6^2), \Omega_{20} \sim N(0, 3^2)$

The probability of landing point within a certain r is presented as $p(R \leq r)$. As shown in Fig. 5.30, the cylinder drops within $R \leq$1m with 30% probability and within $R \leq$3.3m with 90% probability. The probability of a landing point beyond a certain radius r is described by $p(R>r)$=1- $p(R \leq r)$. If $p(R>r)$ is small enough, it might be called risk free. The risk free zone is defined as the area beyond r. Details about risk free zones are shown in Table 5.8 and Fig. 5.31.

Table 5.8: Comparison of statistical value at different $\dot{Z}_0$ distribution

$p(R > r)$	risk free zone
0.10	R>3.3m
0.05	R>3.8m
0.01	R>4.4m

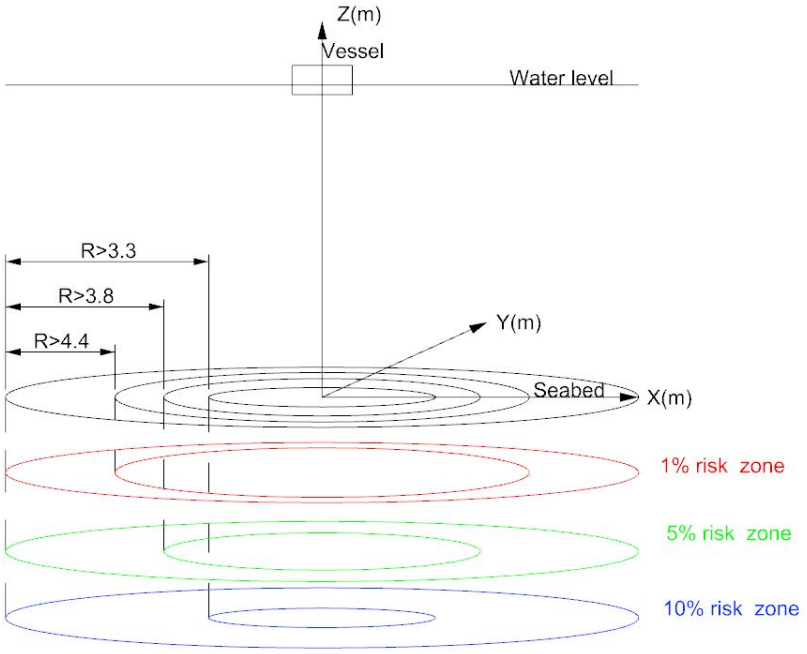

Fig. 5.31. Risk free zone

The impact energy distribution of a dropped object at seabed is another criteria which may be employed in conjunction with Fig. 5.31 to build up a more complete risk assessment. Impact energy is estimated by (DNV, 2010)

$$E_t = \Sigma_{i=1} \frac{1}{2}(m + m_{ii})v_{ti}^2 \tag{5.7}$$

E_t is the total impact energy at the sea bed; m_{ii} is the 3D added mass coefficient in the ith direction. v_{ti} is the terminal velocity at the sea bed in the ith direction. Fig. 5.32 and Fig. 5.33 represent the impact energy distribution of a dropped object at drop angle, 60^o without current and under 0.5m/s current respectively. Comparing Fig. 5.32 and Fig. 5.33 reveals that the high impact energy area marked yellow is greatly influenced by the current and moved in the direction of current and spread out downstream.

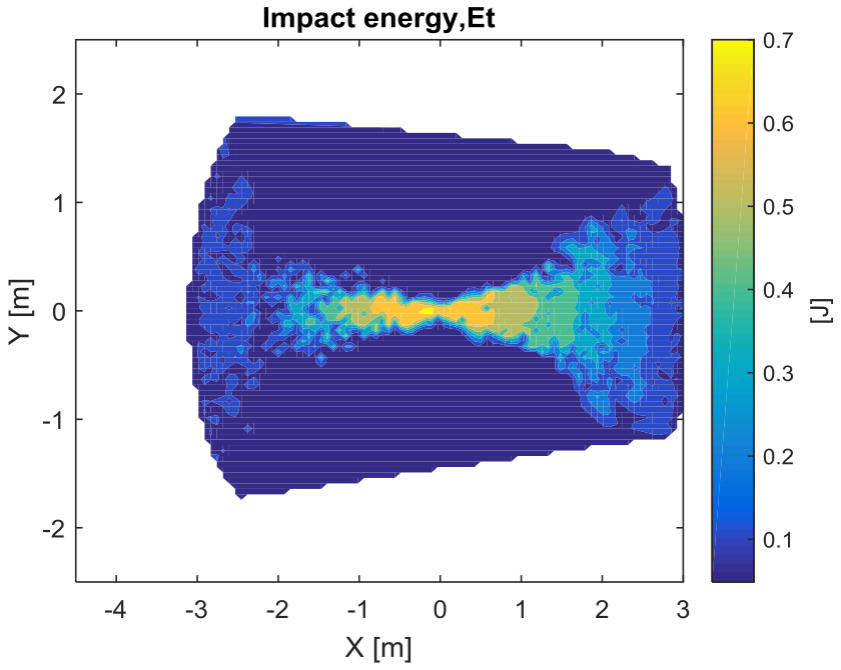

Fig. 5.32. Impact energy distribution for drop angle at 60^o: (a) without current

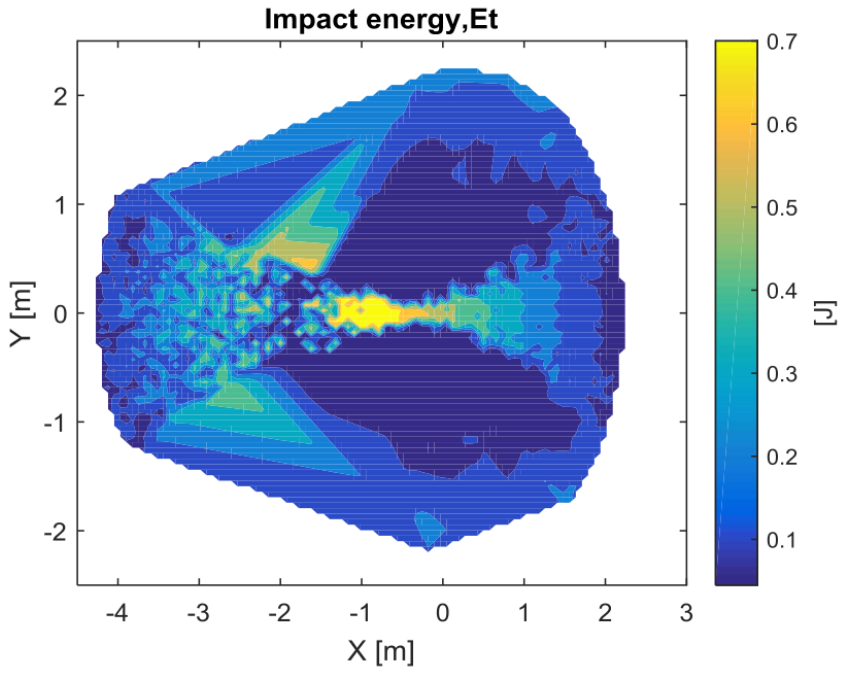

Fig. 5.33. Impact energy distribution for drop angle at 60^o: (b) current with speed 0.5m/s and incoming angle β at 180^o

Chapter 6

Conclusions

6.1 Conclusions

In the first part of this dissertation, the motions of dropped cylindrical objects have been computed based on the 2D theory and validated by experimental results. Since translational motion in y-direction and the rotation around x- and z-directions have been neglected in 2D theory, a new 3D theory for dropped cylindrical objects has been developed which considers all 6DOF motions. The newly developed simulation tool called DROBS, is utilized to predict the 3D trajectory of cylindrical objects dropped into the sea. Results based on the 3D theory for a drilling pipe model with zero rolling frequency are compared with simulated results from the 2D theory by Aanesland (1987). Good agreement is found. In other words, 2D theory is found to be a special case of the new 3D theory. The results also show that drop angle and normal drag coefficient are the most critical factors determining the trajectories, which is consistent with the findings from Aanesland (1987), Luo and Davis (1992), Colwill and Ahilan (1992), and Kim et al. (2002). In addition, rolling frequency mainly influences the trajectory of dropped objects when the drop angle is between 0^o to 45^o based on this study. It is also found that the transverse drag coefficient C_{dy} has little effect on the X-Z plane motion but greatly affects on the Y-Z plane motion with drop angles between 30^o and 45^o. The sensitivity of Y-Z plane motion to the changes of transverse drag coefficient C_{dy} decreases with increasing drop angle. It should be recalled that the assumed initial rolling frequencies are small. This assumption makes the comparison between numerical simulations and measured data more reasonable. By adapting the rolling frequencies, simulated trajectories can be matched to observed experimental trajectories by Aanesland (1987). At last, excursion plots are used to describe the landing point

distribution at the sea bed of dropped cylinders with small rolling frequency. It is concluded that 3D theory can provide a more accurate and reliable prediction of excursion by considering all the degrees of freedom compared to 2D theory.

The second part describes the extension of program DROBS to investigate the influence of varying LCG positions. Initially, three cylinders with different LCG position have been selected for study for which model test results are available. Simulated trajectories match published data from model tests (Aanesland, 1987; Chu et al. 2005). Further, various positions of center of gravity have been assumed for two of the cylinders in order to investigate the influence of LCG position on motion and landing point. LCG position has been found to have a significant impact on trajectories and landing points of dropped cylindrical objects. Therefore, LCG position should be carefully monitored in model tests. It should also be pointed out that the assumed position of the trailing edge Xt is a critical factors which can greatly affect the simulated trajectory. Large Xt may be better for simulations with large initial orientation angle. As already indicated by other researchers, the initial orientation angle θ_0 greatly influence the underwater trajectory of dropped cylinders. With increasing orientation angle excursion increases in positive X-direction. Overall, results from the developed simulation program DROBS compare well with results from model tests and correctly capture the influences of important simulation parameters.

Finally, the 3D theory is expanded to consider the underwater dynamic motion of a dropped cylindrical object under currents from different directions. Correspondingly, DROBS is utilized to investigate how uniform currents from different directions (incoming angle at $0^o, 90^o, 180^o$, and 270^o) and with various amplitude affects the trajectories of dropped cylinders. It is found that the trajectories and landing points of the dropped cylinders are greatly influenced by the current. Further, water entry of the dropped cylinders is modeled as stochastic process. Orientation angle, translational velocity and rotational velocity of the cylinder after being fully immersion are treated as random variables with normal probability density distribution. Firstly, Monte Carlo simulations of landing points of dropped cylinder with drop angles at 60^o through air-water columns without current are accomplished in DROBS. The results show that DROBS based Monte Carlo simulations can provide reasonable landing point distribution. Also, the results indicate that the mean value obtained from simplified method in DNV (2010) may be too low to properly describe the landing point distribution for dropped cylinders. Then, the Monte Carlo simulations are used for predicting the landing point distribution of dropped cylinders under the influence of current. The maximum mean value is obtained for a drop

angle of 75^o. Lastly, the overall landing point distribution plots; probability density function (PDF) and cumulative distribution function (CDF) are provided to help study the uncertainty in landing point estimates and also to set risk free zones. What's more, the impact energy distribution at seabed for dropped cylinder under current and no current are presented to provide another criteria to do risk assessment of possible damage to subsea equipment.

All in all, the art state of my work includes the following:

- Based on the traditional 2D theory, a new 3D theory is extended and established to consider the complete 6DOF motions of dropped cylinders into water. More reasonable hydrodynamic effect are considered: drag coefficients are updated at each time step as per Reynolds number; lift force because of rolling rotation are also considered. More factors like rolling frequencies, drag coefficient in Y direction, etc are firstly found to influence the trajectories of dropped cylinders.
- By comparing the new 3D theory to traditional 3D theory, the trailing edge effect of long cylinders is considered by potential flow theory for a slender body instead of expensive laboratory tests or direct neglect. Also, environmental conditions including current and physical properties of the dropped cylinder like mass distribution are quantitatively studied and found to have a great influence on the trajectories and landing points of the dropped cylinder.
- Other than study on the deterministic model of the 3D theory for the dropped cylinder, a stochastic model is combined with the new 3D theory to study the landing point distribution and impact energy distribution on the sea bed. At the same time, the definition of risk free zone is firstly proposed in Ocean Engineering industry.

6.2 Future work

Though DROBS shows great potential to study the dropped cylindrical objects, it still operates with limitations. To reduce the limitation and expand the capabilities, in future work, further development and more study are required, especially:

- The effect of surface waves should be studied and integrated into DROBS.(Mei et al., 2005)

- Unsteady effects of viscous drag of cylindrical bodies should be considered more accurately .(Shiels and Leonard, 2001; Ramberg, 1983)
- More general and complicated shaped objects which may accidentally fall into water during offshore operations including: Christmas tree, plum, manifold, BOP stacks, etc should be simulated. (Singh and Vadali, 1993)
- Flexibility (bending and twisting) should be considered by nonlinear dynamics simulations of the motion of dropped slender body to make simulations more realistic and predictions more accurate.(Garrett, 1982; Nordgren, 1974)

Bibliography

Aanesland, V. (1987). "Numerical and experimental investigation of accidentally falling drilling pipes". In: *19th Annual OTC*.

ABS (2010). *Guidance notes on accidental load analysis and design for offshore structures*. Guidance notes. ABS.

Awotahegn, M.B. (2015). "Experimental investigation of accidental drops of drill pipes and containers". Master Thesis. University of Stavanger.

Awotahegn, M.B., Oosterkamp, L.D., and Nystrøm, P.R. (2016). "3D study of dropped object motion in sea water based on scale test". In: *ISOPE Conference Paper*.

Beeker, G.L., Bennett, R.L., and Payne, J.M. (1993). *Performance flight testing*. USAF. Chap. 13.

Bolton, W. (1998). *Control Engineering*. Essex, U.K.: Longman.

Brown, I.C. and Perry, S.H. (1989). *The assessment of impact damage caused by dropped objects on concrete offshore structures*. Offshore Technology Report, pp. 87–240.

Carstensen, S., Mandviwalla, X., Vita, L., and Paulsen, U.S. (2014). "Lift of a rotating circular cylinder in unsteady flows". In: *J. Ocean and Wind Energy* 1.1, pp. 41–49.

Chu, P.C. (2009). "Mine impact burial prediction from one to three dimensions". In: *ASME Journal of Applied Mechanics Review* 62.

Chu, P.C. and Fan, C.W. (2006). "Prediction of falling cylinder through air-water-sediment columns". In: *ASME Journal of Applied Mechanics Review* 73, 300–314.

Chu, P.C., Smith, T.B., and Haeger, S.D. (2002). "Mine impact burial prediction experiment". In: *J. Counter-Ordnance Technology*.

Chu, P.C., Gilles, A., and Fan, C.W. (2005). "Experiment of falling cylinder through the water column". In: *Experimental Thermal and Fluid Science* 29, pp. 555–568.

Colwill, R.D. and Ahilan, R.V. (1992). "Reliability analysis of the behavior of dropped objects". In: *24th Annual OTC*. Houston, Texas.

Cox, R.G. (1970). "The motion of long slender bodies in a viscous fluid". In: *J.Fluid Mech* 44, pp. 791–810.

DNV (1996). *Worldwide Offshore Accident Data bank(WOAD)*. DNV.

– (2010). *Risk assessment of pipeline protection*. RP-F107. DNV.

DORIS (2016). URL: http://www.doris.dropsonline.org/.

Dubi, A. (2000). *Monte Carlo Applications in Systems Engineering*. West Sussex, U.K.: Wiley.

Feldman, J. (1979). *Revised Standard Submarine Equations of Motion*. Project n.009-0101. David W Taylor Naval Ship Research and Development Center (DTNSRDC).

Garrett, D.L. (1982). "Dynamic analysis of slender rods". In: *J. Energ. Resour – ASME* 104, pp. 302–307.

Gaudet, S. (1998). "Numerical simulation of circular disks entering the free surface of a fluid". In: *J. Physics Fluids* 10.10, pp. 2489–2499.

Gertler, M and Hagen, G.R. (1967). *Standard Equations of Motion for Submarine Simulation*. SPD-0393-09. David W Taylor Naval Ship Research and Development Center.

Glasheen, J.W. and McMahon, T.A. (1996). "Vertical water entry of disks at low Froude numbers". In: *J. Physics Fluids* 8, pp. 2078–2083.

Gudmestad, O.T. and Moe, G. (1996). "Standard Equations of Motion for Submarine Simulation". In: . *Hydrodynamic Coefficients for Calculation of Hydrodynamic Loads on Offshore Truss Structures* 9, pp. 745–758.

Hoerner, S.F. (1958). *Fluid dynamics drag*. Bricktown, NJ.

John, M.S. and Francis, E. P. (1962). *Six-degree-of-freedom equations of motion for a maneuvering re-entry vehicle*. Technical Report. NAVTRADEVCEN 801A.

Kim, Yonghwan, Liu, Y.M., and Yue, D.K.P. (2002). "Motion dynamics of three-dimensional bodies falling through water". In: *17th IWWWFB*, pp. 21–081.

Kutta-Joukowski lift theorem (1941). URL: https://www.grc.nasa.gov/www/k-12/airplane/cyl.html.

Lee, M., Longoria, R.G., and Wilson, D. E. (1997). "Cavity dynamics in high speed water entry". In: *J. Physics Fluids* 9, pp. 540–550.

Luo, Y. and Davis, J. (1992). "Motion simulation and hazard assessment of dropped objects". In: *Proceedings of the Second International Offshore and Polar Engineering Conference* 4.

Majed, A. and Cooper, P. (2013). "High Fidelity Sink Trajectory Nonlinear Simulations for Dropped Subsea Objects". In: *Proceedings of the Twenty-third International Offshore and Polar Engineering Anchorage, Alaska, USA*.

Mann, J., Liu, Y.M., Kim, Y.W., and Yue, D.K.P. (2007). "Deterministic and stochastic predictions of motion dynamics of cylindrical Mines Falling Through Water". In: *IEEE J. Oceanic Engineering* 32.1, pp. 722–738.

Mazzola, A. (2000). "A probabilistic methodology for the assessment of safety from dropped loads in offshore engineering". In: *Risk Analysis* 20.3, pp. 327–338.

McGrath, E.J., Basin, S.L., Burton, R.W., Irving, D.C., Jaquette, S.C., Ketler, W.R., and Smith, C.A. (1973). *Techniques for Efficient Monte Carlo Simulation:Selecting Probability Distributions*. Final Report. Office of Naval Research.

Mei, C.C., Stiassnie, M., and Yue, D.K.P. (2005). *Theory and Applications of Ocean Surface Waves*. Singapore: World Scientific.

Mei, X., Liu, Y., and Yue, D.K.P. (1999). "On the water impact of general two-dimensional sections". In: *J. Applied Ocean Research* 21, pp. 1–15.

Metropolis, N. (1987). "The beginning of the Monte Carlo method". In: *J. Los Alamos Science* 15, pp. 125–130.

Monte Carlo Simulation Basics (2004). URL: http://vertex42.com/ExcelArticles/mc/MonteCarloSimulation.html.

Nagle, R.K., Saff, E.B., and Snider, A.D. (2008). *Fundamentals of differential equations and boundary value problems*.

Newman, J. N. (1977). *Marine hydrodynamic*. , Cambridge, Massachusetts: The MIT Press.

Nordgren, R.P. (1974). "On Computation of the motion of elastic rods". In: *Journal of applied mechanics*.

Ramberg, S.E. (1983). "The effects of yaw and finite length upon the vortex wakes of stationary and vibrating circular cylinders". In: *J. Fluid Mechanics* 128, pp. 81–107.

Rouse, H. (1938). *Fluid Mechanics for Hydraulic Engineers, 1st ed.*, New York: McGraw-Hill Book Company.

Schlichting, H. (1979). *Boundary layer theory*. New York: McGraw-Hill Book Company.

Shiels, D. and Leonard, A. (2001). "Investigation of a drag reduction on a circular cylinder in rotary oscillation". In: *J. Fluid Mechanics* 431, pp. 297–322.

Singh, T. and Vadali, S.R. (1993). "Input-shaped control of three-dimensional maneuvers of flexible spacecraft". In: *J. Guidance, Control and Dynamics* 16.6.

Sun, H. and Faltinsen, O.M. (2007). "Water impact of horizontal circular cylinders and cylindrical shells". In: *J. Applied Ocean Research* 28, pp. 299–311.

Thorton, S. T. and Marion, J. B. (2003). *Classical dynamics of particles and systems,5th Edition*. New York: McGraw-Hill Book Company.

Von Karman, T. (1929). *The impact of seaplane floats during landing*. TN. NACA, pp. 1–8.

Wagner, H. (1931). *Landing of seaplanes*. TN. NACA, pp. 193–215.

Wei, Z.Y. and Hu, C.H. (2015). "Experimental study on water entry of circular cylinders with inclined angles". In: *J Mar Sci Tech* 20, pp. 722–738.

Xiang, G., Birk, L., Li, L.X., Yu, X.C., and Luo, Y. (2016). "Risk free zone study for cylindrical objects dropped into water". In: *J.Ocean System Engineering* 6.4, pp. 377–400.

Xiang, G., Birk, L., Yu, X.C., and Lu, H.N. (2017). "Numerical Study on the Trajectory of Dropped Cylindrical Objects". In: *J.Ocean Engineering* 130, pp. 1–9.

Yasseri, S. (2014). "Experiment of free-falling cylinders in water". In: *Underwater Technology* 32, pp. 177–191.

Vita

The author was born in Yichang, China. He obtained his Bachelor's degree in Naval Architecture and Marine Engineering from Huazhong University of Science and Technology in 2011. He graduated from Stevens Institute of Technology in 2013 with a Master's of Science in Ocean Engineering and from the University of New Orleans in May 2017 with a Doctorate of Philosophy in Naval Architecture and Marine Engineering.